

SESSION I

X-ray Absorption Spectroscopy of Radionuclides

Chairs: G. Kaindl, G. Bernhard, D.L. Clark

ACTINIDES IN SILICATE GLASSES AND MELTS AND ON MINERAL SURFACES: INFORMATION ON LOCAL CO-ORDINATION ENVIRONMENTS FROM XAFS SPECTROSCOPY AND BOND VALENCE THEORY

Gordon E. Brown, Jr.,^{1,2} François Farges,^{1,2,3} John R. Bargar² and Hillary Thompson Berbeco⁴

¹Surface & Aqueous Geochemistry Group

Department of Geological & Environmental Sciences
Stanford University, Stanford, CA 94305-2115, USA

²Stanford Synchrotron Radiation Laboratory

P.O. Box 4349, Stanford, CA 94309-0210, USA

³Laboratoire des Géomatériaux, Université de Marne-la-Vallée

5, blvd Descartes, Champs s/Marne, 77454 Marne-la-Vallée Cedex 2, France

⁴F.W. Olin College of Engineering

1735 Great Plain Avenue, Needham, MA 02492-1245

Abstract

The impact of actinides on the environment is mitigated by their interaction with particle surfaces and by incorporation into suitable waste forms. In both cases, a fundamental knowledge of the local co-ordination environment of actinide ions is essential for understanding their stability in various near-surface environments under a range of conditions. When actinide ions are sorbed on mineral surfaces, the extent to which the ions are immobilised depends on the type of surface complex or solid precipitate that forms. When incorporated into a glass or crystalline waste form, the stability of the actinide will depend in part on its redox state and local co-ordination environment. In both cases, XAFS spectroscopy can provide unique information on the number and types of first and, in certain cases, more distant neighbours, and their geometric arrangement (including inter-atomic distances and a measure of their disorder). When this structural information from XAFS spectroscopy is combined with Pauling bond valence theory and modern bond valences corrected for bond length variations, it is also possible to develop plausible models for their medium-range co-ordination environments (out to ≈ 4 Å radial distance around the actinide) for both sorbed actinide ions and those present in a silicate glass or melt. We discuss results from several XAFS studies of the naturally occurring actinides uranium and thorium in sorption samples, silicate glasses and silicate melts at high temperature.

Introduction

When XAFS spectroscopy was first introduced as an element-specific method capable of providing quantitative information on the local co-ordination environment around selected atoms in crystalline and amorphous materials [1], few appreciated its potential applications in science and technology. In spite of a variety of early problems, including (1) non-optimised synchrotron sources operating in parasitic mode, (2) the inaccuracy of some XAFS-derived inter-atomic distances and co-ordination numbers due to inadequate model compounds and theoretical methods for deriving accurate phase shifts and backscattering amplitudes, (3) lack of proper experimental procedures and (4) anharmonic effects, this potential has been largely realised in modern XAFS studies. Because of dramatic improvements in XAFS theory, particularly the availability of user-friendly computer codes capable of accurate modelling of XAFS spectra (both XANES and EXAFS) of elements in different co-ordination environments (see e.g. Feff [2,3]), it is now possible to obtain accuracies of $\pm 0.01 \text{ \AA}$ for first co-ordination shell inter-atomic distances around most absorber atoms and of $\pm 0.04 \text{ \AA}$ for second-shell distances, even in structurally complex materials [4]. Corresponding improvements in synchrotron light sources [5] and X-ray detectors [6,7] have also had dramatic impacts on XAFS spectroscopy and its many applications. It is now possible to determine first-shell co-ordination environments of elements with atomic number >15 (P) at concentrations of 100 ppm in most types of materials (crystalline and amorphous solids under ambient conditions and aqueous solutions). With improvements in focusing optics at third-generation hard X-ray synchrotrons, X-ray beam diameters of 1-5 μm are now available for micro-XAFS studies of the spatial distribution and speciation of elements in highly heterogeneous samples such as soils and sediments [8,9]. These beams are also useful for the collection of spectra with very low signal-to-noise ratios (i.e. $< 10^{-4}$) required for improved pre-edge, XANES deconvolution, and next-nearest neighbour analyses, especially in natural materials, such as glasses or gels, where a continuum of sites for one specific element may be present. Applications of XAFS spectroscopy in mineralogy and geochemistry [10], environmental geochemistry/chemistry [11,12], interfacial chemistry [13,14], glass science [15,16], materials science and chemistry [11,17], and soil science [18], among other fields of science and engineering, are quite varied and, in many cases, provide unique information not easily obtainable by other means. In the case of actinides, XAFS spectroscopy has been used to obtain unique information about their co-ordination environments when present at mineral-water interfaces, in metamict minerals, or in silicate glasses and melts.

The purpose of this paper is to review several examples of these studies and to demonstrate how XAFS spectroscopy can be combined with Pauling bond valence theory to place constraints on the medium-range co-ordination environments of actinide ions in amorphous materials and at mineral-aqueous solution interfaces. In addition, because positional (or static) and thermal disorder involving actinide ions in solids or liquids at high temperatures can result in significant inaccuracies in inter-atomic distances and co-ordination numbers when using the normal harmonic approximation in EXAFS data analysis, we review the effects of anharmonicity on EXAFS spectra and some of the methods that can be used to account for these effects. Selected applications of XAFS spectroscopy to U and Th ions in metamict minerals, glasses and melts are discussed in a companion paper in this volume [19].

XAFS spectroscopy and anharmonic effects

EXAFS spectra can be modelled accurately, in the absence of multiple-scattering of the photoelectron among different atoms in the vicinity of the absorber, by using the single-scattering formalism [20], where the modulations of the normalised absorption coefficient $\chi(k)$ are given by:

$$\chi(k) = S_0^2 rf \sum_j \frac{N_j |F_{cw}|(k, R)}{k} \int_0^\infty \frac{g(R_j)}{R_j^2} e^{-2R_j/\lambda} \sin(2kR_j + \sum \phi(k, R)) dR \quad (1)$$

Here S_0^2 is the amplitude reduction factor, and rf is the reduction factor for the total central atom loss. Also, for every shell of neighbouring atoms j , N_j is the number of backscattering atoms; $|F_{cw}(k, R)|$ is the effective, curved-wave backscattering amplitude; R_j is the average distance between the central and backscattering atoms; $g(R_j)$ is the (partial) radial distribution function of the neighbouring distances around the absorbing element; λ is the photoelectron mean free path; and $\sum \phi(k, R)$ is the sum of the phase shift functions (central and backscattering phase shifts). This formalism is valid for any experimental XAFS data. Eq. (1) can be simplified by using a Gaussian pair distribution function to represent $g(R_j)$ when atomic vibrations are harmonic or when the distribution of inter-atomic distances is relatively symmetrical around the absorbing atom.

The local environment of actinides in many crystalline and amorphous materials at ambient to low temperatures (to 10 K) can be modelled accurately from EXAFS spectra using the harmonic approximation. This was demonstrated in several studies of U co-ordination environments in complex crystalline solids [21,22], metamict minerals [23] and silicate glasses [21]. This has also been demonstrated for Th in crystalline and amorphous materials [24,25]. However, in several of these studies, a quasi-anharmonic approach (two Gaussian shells fit and averaged) was needed for analysing the EXAFS spectra properly.

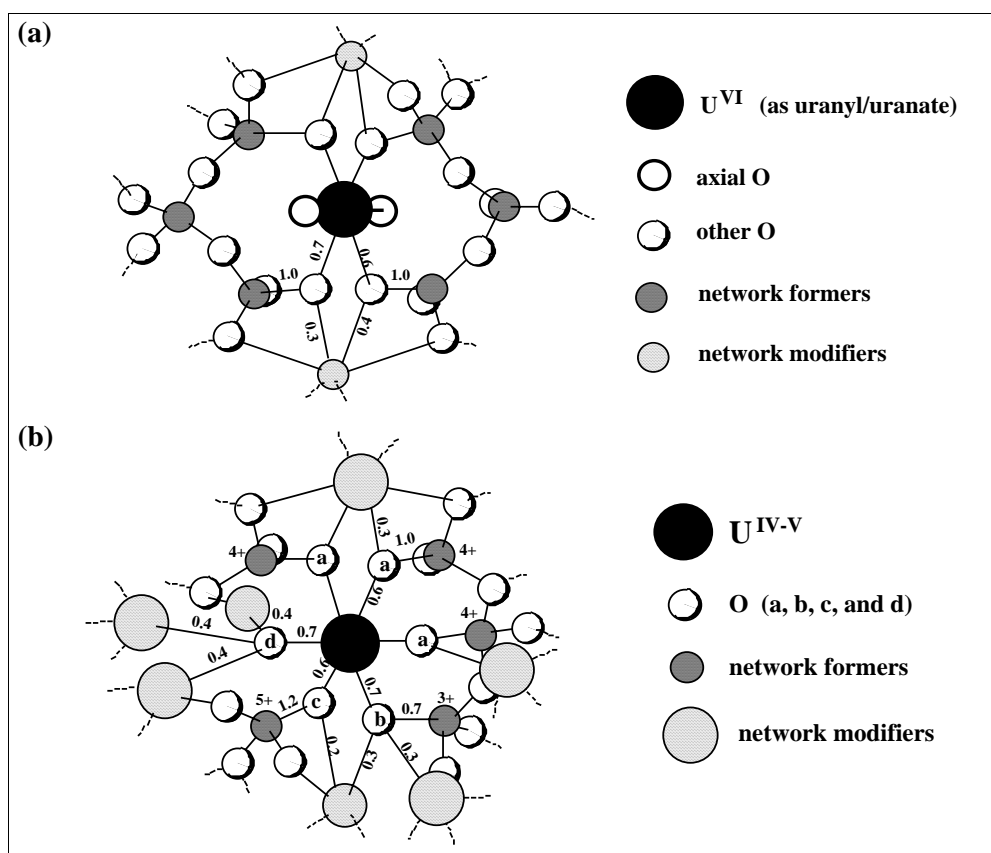
When positional disorder around an atom in a solid or liquid is large, however, such as for a low-valent, weakly bonded cation in silicate glasses, or when inter-atomic vibrations are anharmonic, such as for a non-framework cation in a silicate melt at high temperature, the harmonic approximation may fail to model the EXAFS data accurately, and EXAFS-derived inter-atomic distances and co-ordination numbers are often too small. In this case, it is necessary to use a $g(R_j)$ function that properly models anharmonicity. There are a number of ways of doing this (see [15] for a review of methods), including the cumulant expansion method [20], empirical anharmonic potential energy functions for a given bond type [26,27], empirical models that utilise known linear thermal expansion coefficients of specific bonds or Pauling bond valence for specific atom pairs [28] and analytical expressions for the anharmonic pair correlation function [29]. When anharmonic effects are large, the cumulant expansion method may be inadequate [30,31]. An example of this is the recent work of Wu and Farges [31], who carried out a high-temperature EXAFS study of crystalline ThO₂ over the temperature range 20 to 1474°C (see Figure 1 in [19]). They used the analytical expression for anharmonic effects in Winterer's [29] XAFS data analysis code to derive average Th-O distances as a function of temperature that are consistent with known Th-O bond thermal expansion. The resulting average Th-O distances at 1474°C are 2.44(1) and 2.33(1) Å, respectively, from anharmonic and harmonic fits of Th L_{III}-EXAFS data for ThO₂, in excellent agreement with *in situ* X-ray diffraction experiments.

U and Th co-ordination environments in silicate glasses and melts

Silicate glasses and melts have a special role in the long-term disposal of actinides because of the proposal to incorporate high-level nuclear waste in borosilicate glass [32]. The initial step in the vitrification process involves incorporation of actinides and other radioactive elements in a borosilicate melt, so a knowledge of the medium-range structural environment of the actinides in the melt and the quenched melt as a function of melt composition is important for tailoring the local environment of actinide ions for maximum stability.

Although the structures of silicate glasses and melts lack long-range order, the local co-ordination environments around cations can be relatively undistorted. For example, all available evidence from X-ray scattering and NMR measurements in silicate glasses and melts as well as borosilicate glasses and melts indicates that the silicate tetrahedron (SiO_4^{4-}) and borate tetrahedron (BO_4^{5-}) and triangle (BO_3^{3-}) are stable and relatively undistorted [15,33]. These small, high-valent ions act as network formers, whereas large, low-valent cations like Na^+ , K^+ or Ca^{2+} , which have co-ordination numbers of 6 to 8 in silicate glasses [34-38], act as network modifiers or, alternatively, as charge-compensating cations, when cations like Al^{3+} occur in tetrahedral co-ordination in aluminosilicate glasses and melts. Uranium(IV,V) and thorium(IV) are relatively large ions that are typically six-co-ordinated by oxygens in silicate glasses and melts [21,24]. However, when the partial pressure of oxygen is sufficiently high to favour U(VI), uranium typically occurs in a different type of co-ordination environment in silicate glasses and melts, referred to as trans-dioxo, with two axial oxygens forming relatively short double bonds [$d(\text{U} = \text{O}_{\text{axial}}) = 1.77(2)$ to $1.85(2)$ Å]. The U(VI) co-ordination environment is completed by 4 to 5 equatorial oxygens that form longer bonds [$d(\text{U} - \text{O}_{\text{equatorial}}) \approx 2.23(3)$ Å]. Figure 1 shows models of these co-ordination environments in a sodium silicate glass derived from EXAFS spectroscopy and Pauling bond valence theory (see section entitled *Constraints on the medium-range co-ordination environments of cations in silicate glasses and melts and on mineral surfaces from XAFS spectroscopy and Pauling bond valence theory*). A similar co-ordination environment for U(VI) has also been found in naturally occurring Si-Al-Fe gels found in a uranium deposit associated with granitic rocks [39].

Figure 1. Models of medium-range co-ordination environments of (a) U(VI) and (b) U(V) and U(IV) in silicate glasses showing bond valence values for selected bonds (after [21])



XAFS spectroscopy has also been used to determine the average first-shell co-ordination environments of actinides in silicate melts at high temperature (see [15] and [40] for a discussion of high-temperature EXAFS methods). For example, the local co-ordination environments of 0.2 to 7 wt.% U(VI) in Na₂Si₂O₅ and Na₂Si₃O₇ composition glasses and melts were studied at temperatures to 1 550 K [41]. U(VI) was found to be present as the uranyl moiety in these glass/melts for all temperatures and compositions examined. The local co-ordination environment of Th(IV) was also determined using high-temperature XAFS methods in the same glass/melt compositions [41]. Th(IV) was found to occur as a mixture of six and eight-co-ordinated Th at the 1-3 wt.% Th level, but as eight-co-ordinated Th when at trace levels (90-1 000 ppm). For these particular glass/melt compositions, neither U nor Th was found to undergo significant co-ordination changes during the glass-to-melt transformation. However, special care in data analysis was needed to account for the effects of anharmonicity (both positional and thermal effects) which tend to artificially increase the (apparent) amount of six-co-ordinated Th.

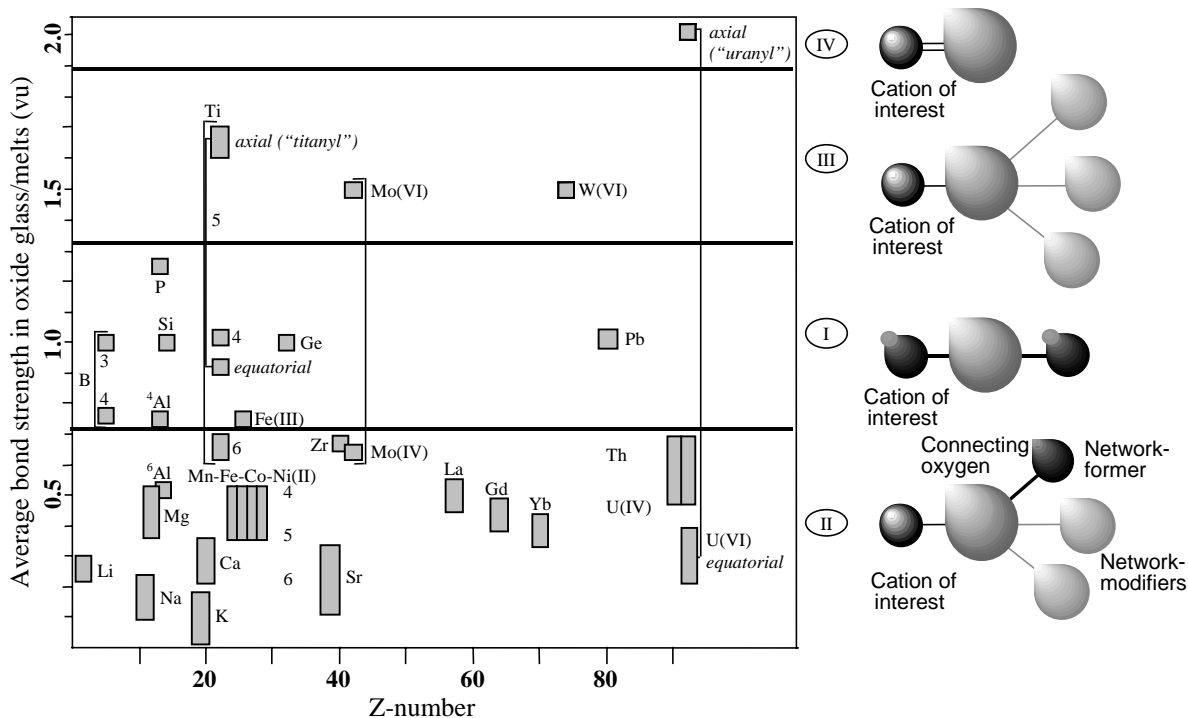
The co-ordination environments of a number of other selected cations commonly found in silicate, aluminosilicate and borosilicate glasses and melts are discussed in [15]. Many of these ions, including Zr(IV) and Th(IV), are “spectroscopically silent” and cannot be studied by most element-specific spectroscopic methods, including EPR, NMR and UV-vis-NIR spectroscopy. In addition, when at low concentrations, the co-ordination environments of these cations cannot be determined by X-ray or neutron scattering methods. The scattering power of an atom and its positional and thermal disorder are also important limitations. For example, the co-ordination environment of Na⁺ in sodium silicate glasses and melts cannot be determined with much accuracy using X-ray scattering methods, even when present at relatively high concentrations, because the Na-O pair correlation function contributes little to the overall radial distribution function due to these effects [15]. This is also true for other important network modifiers like K⁺ and Ca²⁺. For these ions, as well as for the actinides, XAFS spectroscopy provides structural and compositional information about co-ordination environments that often can not be obtained using other structural methods.

Structural classification of cations in silicate glasses and melts

A convenient way of classifying cations among network forming and network modifying types is to examine their average bond strengths (s) in valence units (vu), which are defined in the classical Pauling sense [42] as ion charge/ion co-ordination number. Figure 2 plots bond strength values for many cations found in natural and technologically important silicate, aluminosilicate and borosilicate glasses and melts versus their atomic numbers. Cations in Category I ($s = 0.75$ - 1.3 vu) typically act as network formers, whereas those in Category II ($s < 0.75$ vu) act as network modifiers or charge-compensating cations. Generalised pictures of the linkages for each category of cation (I, II, III or IV) in glass and melts are shown on the right side of Figure 2. The figure to the right of Field I corresponds to two typical network formers (small dark grey atom) bonded to a common “bridging” oxygen (large light grey atom). It depicts more covalent bonds using thicker lines, with bond valences corresponding to 1 ± 0.25 vu for each bond. The figure to the right of Field II shows a network modifying ion (small dark grey atom) bonded to a non-bridging oxygen that is also bonded to a network-former, such as Si, and two other network modifier ions (light grey). The network modifier-oxygen bonds are typically more ionic than network former-oxygen bonds and have individual bond valences of < 0.75 vu). The figure to the right of Field III corresponds to a “complex-forming” ion that can only bond to non-framework oxygens (i.e. neither bridging nor non-bridging) because of the very high bond valence of these bonds ($1.25 < s < 2$ vu). The oxygens to which these “complex formers” bond are also bonded to an appropriate number of network modifiers required to satisfy Pauling’s second rule. Finally, the figure to the right of Field IV shows the unusual case of a non-framework oxygen such as the axial oxygen of a uranyl moiety, with bond valence of 2 vu.

Figure 2. Average bond strength [43] versus atomic number (Z) for a variety of cations occurring in natural and technologically important silicate, aluminosilicate and borosilicate glasses and melts

The two five-co-ordinated values for Ti connected by the bracket between Fields I and III represent the apical Ti = O bond (“titanyl”, $s = 1.7$ vu) and the four Ti-O bonds ($s \approx 0.7$ - 0.8 vu). Similarly, the bond strengths for U(VI)-O_{axial} and U(VI)-O_{equatorial} are located in Fields IV and II, respectively (after [44]).



Six-co-ordinated U(IV) and Th(IV) have relatively high individual M-O bond valences (≈ 0.7 vu), which restricts the types of oxygens to which they can bond in silicate glasses and melts. This is also true of U(VI) in the uranyl moiety, in which the $U = O_{axial}$ bond has $s \approx 2$ vu, whereas $U-O_{equatorial}$ bonds have $s \approx 0.62$ vu. Some of the implications of the very high bond valence of $U = O_{axial}$ bonds for local and medium-range structure in silicate glasses and melts are discussed further in the following section.

Table 1 lists a number of parameters for selected cations (M), including (1) nominal valences; (2) most common co-ordination numbers in oxide compounds; (3) ionic radius values for different co-ordination numbers [45]; (4) mean linear thermal expansion coefficient of the M-O bond [46]; (5) mean M-O interatomic distance at 298 K (from the sum of Shannon and Prewitt ionic radius values [45]); (6) mean M-O interatomic distance at 1 773 K (calculated using $\bar{\alpha}$ values in Table 1); (7) field strength of the cation at 298 K; (8) the R_0 value used to calculate the Brese and O’Keeffe values of M-O bond valence [43]; (9) M-O bond valence at 298 K; and (10) M-O bond valence at 1 773 K. These parameters are useful for predicting the average co-ordination environments of cations in silicate glasses and melts and in building plausible medium-range structural models for these materials using the approach discussed below.

Table 1. Valence (Z), co-ordination number (CN), ionic radius, mean linear M-O expansion coefficient ($\bar{\alpha}$) ($\times 10^6 \text{ K}^{-1}$) at 1 773 K, mean d(M-O) at 298 K, mean d(M-O) at 1 773 K, field strength, and bond valences at 298 K and 1 773 K for selected cations occurring in silicate glasses and melts (after [15])

Cation (M)	Nominal valence (Z) ⁽¹⁾	CN (M-O) ⁽²⁾	Ionic radius (\AA) ⁽³⁾	Mean linear $\bar{\alpha}$ ⁽⁴⁾	$R_{298\text{K}} = \text{D(M-O)}$ (\AA) ⁽⁵⁾	$R_{1773\text{K}} = \text{D(M-O)}$ (\AA) ⁽⁶⁾	Field strength $\{Z/R^2\}$ ⁽⁷⁾	R_0 value ⁽⁸⁾	M-O bond valence 298 K (vu) ⁽⁹⁾	M-O bond valence 1 773 K (vu) ⁽¹⁰⁾
Network modifiers										
Cs	1	8	1.74	32.0	3.10	3.25	0.10	2.42	0.16	0.11
K	1	8	1.51	32.0	2.87	3.01	0.12	2.13	0.14	0.09
Na	1	6	1.02	24.0	2.38	2.47	0.18	1.80	0.21	0.17
Sr	2	8	1.26	16.0	2.62	2.68	0.29	2.118	0.26	0.22
Ca	2	6	1.00	12.0	2.36	2.40	0.36	1.967	0.35	0.31
Mg	2	6	0.72	12.0	2.08	2.12	0.46	1.693	0.35	0.32
		5	0.66	10.0	2.02	2.05	0.49		0.41	0.38
		4	0.57	8.0	1.93	1.95	0.53		0.53	0.50
Fe	2	6	0.78	12.0	2.14	2.18	0.44	1.734	0.33	0.30
		5	0.70	10.0	2.06	2.09	0.47		0.41	0.38
		4	0.63	8.0	1.99	2.01	0.51		0.50	0.47
Pb	2	8	1.29	16.0	2.65	2.71	0.28	2.112	0.23	0.20
Al	3	6	0.535	8.0	1.90	1.92	0.83	1.651	0.51	0.48
		5	0.48	6.7	1.84	1.86	0.89		0.60	0.57
	3	6	0.645	8.0	2.00	2.02	0.75	1.759	0.52	0.49
		5	0.58	6.7	1.94	1.96	0.80		0.61	0.58
Ti	4	6	0.605	6.0	1.965	1.98	1.04	1.815	0.67	0.64
		5	0.34	5.0	1.70	1.71	1.38		1.4	1.32
Zr	4	8	0.84	8.0	2.20	2.23	0.83	1.937	0.49	0.46
		6	0.72	6.0	2.08	2.10	0.92		0.68	0.65
Th	4	8	1.05	8.0	2.41	2.44	0.69	2.167	0.52	0.48
		6	0.94	6.0	2.30	2.32	0.76		0.70	0.66
U	6	2	0.45	1.3	1.82	1.82	1.89	2.075	1.99	1.97
		4	0.89	2.7	2.25	2.26	1.19		0.62	0.61
		6	0.89	6.0	2.25	2.27	0.79		2.112	0.69
Network formers										
B	3	4	0.11	5.3	1.47	1.48	1.39	1.371	0.77	0.74
		3	0.01	4.0	1.37	1.38	1.60		1.00	0.98
Al	3	4	0.39	5.3	1.75	1.76	0.98	1.651	0.77	0.74
Fe	3	4	0.49	5.3	1.85	1.86	0.88	1.759	0.78	0.75
Si	4	4	0.26	4.0	1.62	1.63	1.52	1.624	1.01	0.98
Ti	4	5	0.51	5.0	1.95	1.96	1.05	1.815	0.70	0.67
		4	0.42	4.0	1.78	1.79	1.26		1.10	1.07

Constraints on the medium-range co-ordination environments of cations in silicate glasses and melts and on mineral surfaces from XAFS spectroscopy and Pauling bond valence theory

Medium-range ($\leq 4 \text{ \AA}$) co-ordination environments of cations in amorphous oxides or of cations sorbed at mineral-aqueous solution interfaces are difficult to determine by most experimental structural methods. This is true even for cases where a given cation is present at high concentrations, and it is especially true when cation concentration is in the parts per million range. Knowledge of medium-range ordering is essential for a fundamental understanding of the physical properties of aluminosilicate glasses and melts, such as their dissolution kinetics. A molecular-level knowledge of speciation is also

essential for understanding why some cations sorbed at mineral-water interfaces are easily desorbed (e.g. when present as weakly-bonded outer-sphere sorption complexes) and why some are more difficult to desorb (e.g. when present as inner-sphere sorption complexes or as three-dimensional precipitates).

Important constraints concerning the structure and composition of medium-range co-ordination environments of cations in such materials can be developed by combining structural and compositional information from XAFS spectroscopy and X-ray or neutron scattering with the concept of Pauling bond valence and Pauling's second rule for complex ionic crystals. Pauling's second rule [42] states that the sum of bond valences to an ion in a stable co-ordination environment should equal the absolute value of the nominal valence of the ion (± 0.05 vu). This rule works well for crystalline oxides, including structurally complex silicates and aluminosilicates, and it has also been found to work well for cation environments in amorphous silicates [47] and aqueous solutions [48] and on mineral surfaces [49]. For instance, the bond valence rule can be used to test EXAFS-derived parameters for the short-range environments around cations in silicate glasses and melts. The co-ordination number N_j and first-neighbour distances R_j of a selected cation are obtained from fitting the experimental EXAFS spectra. One can then use the R_j values to determine average s_j values (the average bond valence of the bond studied by EXAFS) and determine if the calculated bond valence sum matches the nominal valence of the central ion probed [50]. Discrepancies between calculated valence sums and nominal valences for the central ion can be explained in most cases by the need for an appropriate anharmonic theory or the use of an improper anharmonic theory in fitting the EXAFS data.

We have used the approach described above to place constraints on the short- and medium-range co-ordination environments of cations in silicate glasses and melts [15,47,50] as well as on mineral surfaces [49,51]. We make use of the fact that the range of variations of M-O bond lengths in oxide materials differs with bond type and bond valence. For example, in a sodium aluminosilicate glass/melt, the classical Pauling bond valences for the $^{\text{IV}}\text{Si-O}$, $^{\text{IV}}\text{Al-O}$ and $^{\text{VI}}\text{Na-O}$ bonds are 1.0, 0.75 and 0.167 vu, respectively. These values can be adjusted for variations in Si-O, Al-O, and Na-O bond lengths using the empirical bond strength-bond length model of Brown and Shannon [52] (see also [43,53]). An M-O bond with high bond valence should show less length variation than a bond with low bond valence in oxide materials. This is borne out in crystalline sodium aluminosilicates where the lengths of individual Si-O bonds vary between ≈ 1.54 and ≈ 1.70 Å, with bond valences ranging between 1.28 and 0.82 vu, and those of individual Al-O bonds vary between about 1.63 and 1.82 Å, with bond valences between 1.04 and 0.63 vu [54]. Because of their much smaller bond valences, which range between 0.29 and 0.02 vu, Na-O bonds show much larger variations in length in these materials (≈ 2.2 to ≈ 3.4 Å). All evidence to date indicates that similar bond length ranges occur in sodium aluminosilicate glasses, although the first-shell co-ordination environments of network modifying cations such as Na^+ and Ca^{2+} can be more regular in silicate glasses than in crystalline silicates [15,34,35,38,55].

In developing molecular models for the average medium-range co-ordination environment around a cation (M) in a silicate glass or melt or at a sodium aluminosilicate-aqueous solution interface, we fix the average M-O distance for the M cation to that derived from EXAFS spectroscopy and adjust the Si-O, Al-O, and Na-O bond lengths within the bond length ranges indicated above such that the total bond valence to each type of oxygen is near 2.0 vu. A similar approach works for other bond types as well. In the case of cations at mineral-aqueous solution interfaces, hydrogen bonds play an important role and can contribute significant bond valence (0.7-0.9 vu) when hydroxyl groups are present or much less bond valence (0.1-0.2 vu) when longer hydrogen bonds are present [51,56].

Recent molecular dynamics calculations for a variety of silicate glass and melt structures suggest that Pauling's bond valence rule employing Brese and O'Keeffe bond valences [43] is generally satisfied around most of the ions considered (e.g. O, Si, Na, K, Ti and Fe [50]). The few observed

discrepancies (especially around Ca) were found to be related to inaccurate pair potential parameters (Born-Mayer-Huggins type potentials were used), which were modified to yield excellent bond valence sums and more realistic structures.

Examples of the application of this approach to Zr(IV), Th(IV) and U(VI) can be found in [47], [24] and [21], respectively. As shown in Figure 1, the uranyl moiety is bonded to oxygens in the glass through equatorial bonds with bond valences of ≈ 0.6 vu. In addition, these oxygens are bonded to one four-co-ordinated Si rather than two $^{\text{IV}}\text{Si}$. The latter case would result in a bond valence sum of 2.6 vu and “overbonding” of ≈ 0.6 vu, which violates Pauling’s second rule; the former results in a bond valence sum of ≈ 1.7 vu, with an “underbonding” of ≈ 0.3 vu. This “underbonding” is satisfied by bonding a six-co-ordinated Na to the oxygen with a relatively short Na-O bond. Thus, U(VI) is predicted to bond only to non-bridging oxygens in an aluminosilicate glass or melt, and the axial oxygens of the uranyl moiety are not bonded to other cations since the bond valence of the $\text{U} = \text{O}_{\text{axial}}$ bond is ≈ 2 vu, which satisfies the bond valence requirements of the axial oxygens. This is tantamount to stating that the non-bonded electron density on the axial oxygens is sufficiently small such that lone pair repulsions between axial oxygens and other nearby oxygen ions do not destabilise the local structure [57]. In the case of U(IV), the first-neighbour oxygens around uranium can be bonded to $^{\text{IV}}\text{Al}^{3+}$ and two $^{\text{VI}}\text{Na}^+$, or to one $^{\text{IV}}\text{Si}^{4+}$ and one $^{\text{VI}}\text{Na}^+$, or to three $^{\text{VI}}\text{Na}^+$. Each of these second-neighbour arrangements would result in a bond valence sum near 2 vu.

In the case of uranyl sorption on mineral surfaces, as discussed earlier, the same procedure can be applied to develop plausible models for the extended bonding environment of U(VI). As for the uranyl moiety in silicate glasses, the axial oxygens do not bond to mineral surfaces. Instead, the uranyl ion forms inner-sphere complexes on oxide mineral surfaces by bonding through equatorial oxygens [58].

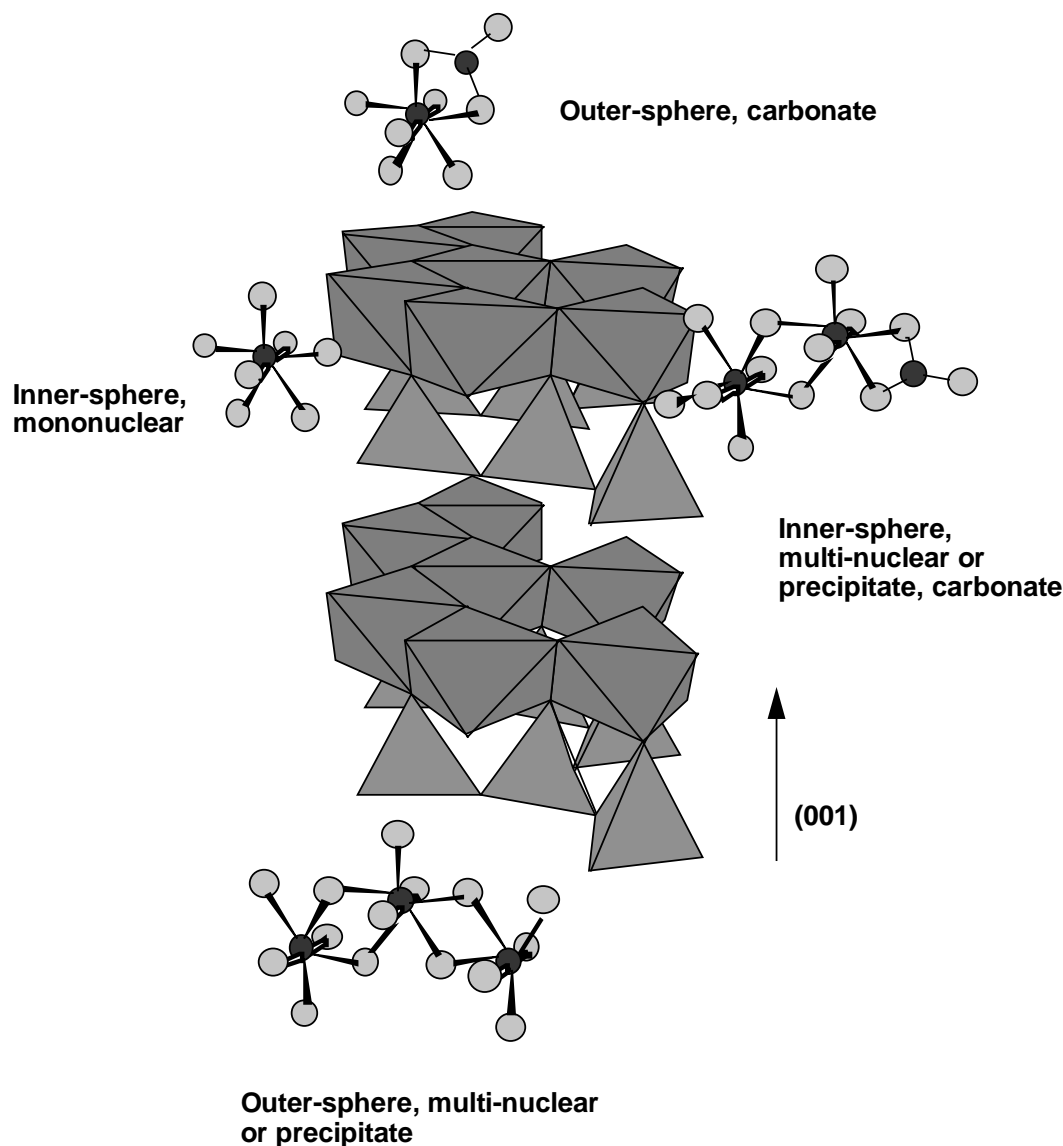
XAFS studies of the sorption of actinides on mineral surfaces

Sorption of actinides on mineral surfaces provides a natural or “engineered” means of sequestering these ions in groundwater aquifers and vadose zones, thus mitigating their dispersal. There have been a limited number of XAFS studies of aqueous actinide ion sorption on “model” mineral surfaces in controlled laboratory conditions as a function of pH, including U(VI) sorption on montmorillonite [59-62], kaolinite [58], vermiculite and hydrobiotite [63], alumina [61,62], silica [59,61,62], silica gel [64], hematite [65], hydrous iron and manganese oxides [66], ferrihydrite [64,67] and hydrothermally altered concrete [68]; Th(IV) sorption on amorphous silica [69]; and Np(V) sorption on goethite [70]. In each of these studies, evidence was found from EXAFS spectroscopy that the actinide is dominantly bound in an inner-sphere fashion on the mineral surface. In the case of actinide sorption on iron and manganese oxide surfaces, EXAFS spectroscopy revealed that the binding is bidentate, indicating a relatively strong adsorbate-adsorbent bond.

The EXAFS study of Thompson, *et al.* [58] examined the reaction products resulting from the uptake of $\text{U(VI)}_{\text{aqueous}}$ onto kaolinite (KGa-2) particles over the pH range 6.0 to 7.9 and in the presence and absence of CO_2 in air. Under all conditions examined, the sorbed uranyl moiety is characterised by two short axial bonds ($d(\text{U} = \text{O}_{\text{axial}}) = 1.80(2) \text{ \AA}$) and five equatorial bonds, consisting of two short ($\approx 2.28(2) \text{ \AA}$) and three long ($\approx 2.48(2) \text{ \AA}$) $\text{U}-\text{O}_{\text{equatorial}}$ bonds. The EXAFS data for U(VI) sorbed on kaolinite under all conditions examined also showed the presence of second-neighbour Si (and/or Al) at $\approx 3.3(3) \text{ \AA}$ from U, suggesting that U(VI) forms inner-sphere complexes on the kaolinite surface (Figure 3). Samples in contact with air at $6.0 \leq \text{pH} \leq 7.0$ had predominantly monomeric uranyl species, whereas at $7.0 \leq \text{pH} \leq 7.9$, the dominant U(VI) species is multi-nuclear, suggesting that increasing pH

Figure 3. Molecular models of U(VI) sorption on kaolinite based on the EXAFS spectroscopy results of Thompson, *et al.* [58]

Possible adsorbed species include mononuclear, monodentate U(VI) complexes bonded through equatorial oxygens to the aluminol layer as well as multi-nuclear U(VI) species bonded in a bidentate fashion to the aluminol layer. Also shown are an outer-sphere U(VI)-carbonato species and an outer-sphere multi-nuclear U(VI) species, neither of which is thought to be a dominant species based on EXAFS analysis.



favours the formation of multinuclear U complexes. In the absence of CO₂, the results of Thompson, *et al.* [58] suggest that the kaolinite surface enhances U(VI) polymerisation, at least in the short term. These multi-nuclear surface species could be precursors to U(VI)-containing precipitates, which may form over longer time periods, or, alternatively, a surface precipitate or a U-Si/Al hydroxide co-precipitate. This finding suggests that kaolinite may be an effective sorbent for the removal of U(VI) from groundwater or ponded waste water because the formation of multi-nuclear sorption species increases kaolinite's capacity for sorbing U(VI) over that if only mononuclear U(VI) species formed. Similar experiments on hematite, followed by EXAFS and ATR-FTIR characterisation studies, indicate the presence of U(VI)-carbonato ternary surface complexes on hematite [65,71].

An interesting application of EXAFS spectroscopy to actinide transport in groundwater is the recent study by Fuller, *et al.* [72] of the interaction of $U(VI)_{\text{aqueous}}$ with an in-ground engineered barrier consisting of bone charcoal in Fry Canyon, Utah. Their hypothesis was that an insoluble uranyl phosphate would form when the $U(VI)$ -containing groundwater interacted with apatite in the bone charcoal. Instead, the $U_{L_{III}}$ -EXAFS spectra of the reacted bone charcoal samples were interpreted as indicating that a significant fraction of the $U(VI)$ was adsorbed on the surface of apatite particles. No evidence for a crystalline U -containing precipitate was found by X-ray diffraction. This example illustrates the utility of EXAFS spectroscopy in detecting adsorbed $U(VI)$ in a complex sample.

Another recent application of micro-XAFS spectroscopy to actinides important in high level radioactive waste involves a study of the interaction of $Pu(V)_{\text{aqueous}}$ with altered tuff from the proposed Yucca Mountain, Nevada high level waste repository [9]. Among other minerals, this tuff contains clinoptilolite $[(Na,K,Ca)_2Al_3(Al,Si)_2Si_{13}O_{36}\cdot 12H_2O]$ and smectite $[(Na,Ca)Al_4(Si,Al)_8O_{20}(OH)_4\cdot 2(H_2O)]$ coated with iron and manganese oxides. Micro-XAFS mapping of the reacted tuff showed that $Pu(V)$ is associated only with the manganese oxide coatings on smectite grains, and not with iron oxide coatings or other minerals. Unfortunately, it is not possible to infer if the $Pu(V)$ forms a true adsorption complex on the manganese oxide from the XAFS data reported. However, this example illustrates the need to know what phase(s) a particular solution species preferentially sorbs onto in a complex mixture of phases so that laboratory studies of sorption processes of actinides and other ions make use of the appropriate model sorbents. The information from this study has very practical applications as well to understanding how $Pu(V)_{\text{aqueous}}$ might be retarded should it be released into a groundwater aquifer.

Conclusions

XAFS studies of actinides in silicate glasses and melts or sorbed on mineral surfaces have provided unique insights about their co-ordination environments not obtainable from other structural methods. When EXAFS-derived inter-atomic distances and co-ordination numbers are combined with the constraints on bonding from Pauling bond valence theory, it is possible to develop plausible molecular models of medium-range co-ordination environments around actinides (out to a radial distance of 4 Å around the absorbing atom) in these materials. The examples included in this review are illustrative of the progress made in XAFS spectroscopy on oxide materials since it was first introduced as a structural method almost 30 years ago. Over the next 30 years, it is likely that further developments in XAFS spectroscopy methods, synchrotron X-ray sources, and X-ray detectors will result in extensions of these types of studies to actinides in even more complex materials at smaller spatial scales and lower concentrations than currently possible.

Acknowledgements

We thank the organising committee for the invitation to present this paper at the Actinide-XAS-2000 Workshop in Grenoble, France. We also wish to thank Dr. David K. Shuh (Chemical Sciences Division, Lawrence Berkeley National Laboratory) for a careful review of the manuscript. Our work discussed in this review was generously supported by the US Department of Energy (DOE) and the US National Science Foundation. Our synchrotron radiation studies were carried out at the Stanford Synchrotron Radiation Laboratory (SSRL) and the Laboratoire pour l'Utilisation du Rayonnement Electromagnetique (LURE). SSRL is supported by the US DOE and the National Institutes of Health. The technical staffs of both laboratories are thanked for their help during our XAFS studies.

REFERENCES

- [1] D.E. Sayers, E.A. Stern and F.W. Lytle, "New Technique for Investigating Non-crystalline Structures: Fourier Analysis of the Extended X-ray Absorption Fine Structure", *Phys. Rev. Lett.*, 27, 1204-1207 (1971).
- [2] J.J. Rehr, S.I. Zabinsky and R.C. Albers, "High-order Multiple Scattering Calculations of X-ray Absorption Fine Structure", *Phys. Rev. Lett.*, 69, 3397-4000 (1992).
- [3] A.L. Ankudinov, B. Ravel, J.J. Rehr and S.D. Conradson, "Real-space Multiple-scattering Calculation and Interpretation of X-ray Absorption Near-edge Structure", *Phys. Rev.*, B 58, 7565-7576 (1998).
- [4] P.A. O'Day, J.J. Rehr, S.I. Zabinsky and G.E. Brown, Jr., "Extended X-ray Absorption Fine Structure (EXAFS) Analysis of Disorder and Multiple Scattering in Complex Crystalline Solids", *J. Am. Chem. Soc.*, 116, 2938-2949 (1994).
- [5] J. Corbett and T. Rabedeau, "Intermediate Energy Storage Rings (2.5-4.0 GeV)", *Synchrotron Rad. News*, 12, 25-33 (1999).
- [6] G.A. Waychunas and G.E. Brown, Jr., "Fluorescence Yield XANES and EXAFS Experiments: Application to Highly Dilute and Surface Samples", *Advances in X-ray Analysis*, 37, 607-617 (1994).
- [7] C. Gauthier, V.A. Solé, R. Signorato, J. Goulon and E. Moguiline, "The ESRF Beamline ID26: X-ray Absorption on Ultra Dilute Sample", *J. Synchrotron Rad.*, 6, 164-166 (1999).
- [8] P.M. Bertsch, D.B. Hunter, S.R. Sutton, S. Bajt and M.L. Rivers, "In Situ Chemical Speciation of Uranium in Soils and Sediments by Micro X-ray Absorption Spectroscopy", *Environ. Sci. Technol.*, 28, 980-984 (1994).
- [9] M.C. Duff, M. Newville, D.B. Hunter, P.M. Bertsch, S.R. Sutton, I.R. Triay, D.T. Vaniman, P. Eng and M.L. Rivers, "Micro-XAS Studies with Sorbed Plutonium on Tuff", *J. Synchrotron Rad.*, 6 (3), 350-352 (1999).
- [10] G.E. Brown, Jr., G. Calas, G.A. Waychunas and J. Petiau, "X-ray Absorption Spectroscopy and its Applications in Mineralogy and Geochemistry", in *Spectroscopic Methods in Mineralogy and Geology*, F. Hawthorne, ed., *Reviews in Mineralogy*, Vol. 18, pp. 431-512, Mineralogical Society of America, Washington, DC (1988).
- [11] S.D. Conradson, "Application of X-ray Absorption Fine Structure Spectroscopy to Materials and Environmental Science", *Appl. Spectrosc.*, 52, 252-279 (1998).

- [12] G.E. Brown, Jr., A.L. Foster and J.D. Ostergren, "Mineral Surfaces and Bioavailability of Heavy Metals: A Molecular-scale Perspective", *Proc. Nat. Acad. Sci. USA* 96, 3388-3395 (1999).
- [13] G.E. Brown, Jr., "Spectroscopic Studies of Chemisorption Reaction Mechanisms at Oxide/Water Interfaces", in *Mineral-water Interface Geochemistry*, M.F. Hochella, Jr. and A.F. White, eds., *Reviews in Mineralogy*, Vol. 23, pp. 309-363, Mineralogical Society of America, Washington, DC (1990).
- [14] G.E. Brown, Jr., V.E. Henrich, W.H. Casey, D.L. Clark, C. Eggleston, A. Felmy, D.W. Goodman, M. Grätzel, G. Maciel, M.I. McCarthy, K. Nealson, D.A. Sverjensky, M.F. Toney and J.M. Zachara, "Metal Oxide Surfaces and Their Interactions with Aqueous Solutions and Microbial Organisms", *Chem. Rev.*, 99, 77-174 (1999).
- [15] G.E. Brown, Jr., F. Farges and G. Calas, "X-ray Scattering and X-ray Spectroscopy Studies of Silicate Melts", in *Structure, Dynamics, and Properties of Silicate Melts*, J.F. Stebbins, P.F. McMillan and D.B. Dingwell, eds., *Reviews in Mineralogy*, Vol. 32, pp. 317-419, Mineralogical Society of America, Washington, DC (1995).
- [16] G. Calas, G.E. Brown, Jr., F. Farges, L. Galois, J.P. Itie and A. Polian, "Cations in Glasses Under Ambient and Non-ambient Conditions", *Nucl. Instru. Meth. Phys. Res.*, B 97, 155-161 (1995).
- [17] "Synchrotron Radiation Techniques in Industrial, Chemical and Materials Science" K.L. D'Amico, L.J. Terminello and D.K. Shuh, eds., Plenum Press, New York (1996).
- [18] S.E. Fendorf, "Fundamental Aspects and Applications of X-ray Absorption Spectroscopy in Clay and Soil Science", in *Synchrotron X-ray Methods in Clay Science*, Clay Minerals Society Workshop Lecture, 9, 19-67 (1999).
- [19] F. Farges, M. Harfouche, P-E. Petit and G.E. Brown, Jr., "Actinides in Earth Materials: The Importance of Natural Analogues", these proceedings (2001).
- [20] E.D. Crozier, J.J. Rehr and R. Ingalls, "Amorphous and Liquid Systems", in *X-ray Absorption. Principles, Applications, Techniques of EXAFS, SEXAFS and XANES*, D.C. Koningsberger and R. Prins, eds., *Chemical Analysis*, Vol. 92, pp. 373-442, John Wiley & Sons, New York (1988).
- [21] F. Farges, C.W. Ponader, G. Calas and G.E. Brown, Jr., "Local Environment Around Incompatible Elements in Silicate Glass/Melt Systems. II: U(VI), U(V) and U(IV)", *Geochim. Cosmochim. Acta*, 56, 4205-4220 (1992).
- [22] H.A. Thompson, G.E. Brown, Jr. and G.A. Parks, "XAFS Spectroscopic Study of Uranyl Co-ordination in Solids and Aqueous Solution", *Am. Mineral.*, 82, 483-496 (1997).
- [23] F. Farges, R.C. Ewing and G.E. Brown, Jr., "The Structure of Aperiodic, Metamict, (Ca, Th)ZrTi₂O₇: An EXAFS Study of the Zr, Th and U sites", *J. Materials Res.*, 8, 1983-1995 (1993).
- [24] F. Farges, "Structural Environment Around Th⁴⁺ in Silicate Glasses: Implications for the Geochemistry of Incompatible Me⁴⁺ Elements", *Geochim. Cosmochim. Acta*, 55, 3303-3319 (1991).

- [25] F. Farges and G. Calas, "Structural Analysis of Radiation Damage in Zircon and Thorite: An X-ray Absorption Study", *Amer. Mineral.*, 76, 60-73 (1991).
- [26] W.E. Jackson, G.A. Waychunas, G.E. Brown, Jr., J. Mustre de Leon, S.D. Conradson, J-M. Combes, "In Situ High-temperature X-ray Absorption Study of Ferrous Iron in Orthosilicate Crystals and Liquids", in *X-ray Absorption Fine Structure*, S.S. Hasnain, ed., pp. 298-301, Ellis Horwood Ltd., Chichester, UK (1991).
- [27] W.E. Jackson, G.E. Brown, Jr., G.A. Waychunas, J. Mustre de Leon, S.D. Conradson and J-M. Combes, "High-temperature XAS Study of Fe₂SiO₄: Evidence for Reduced Co-ordination of Ferrous Iron in the Liquid", *Science*, 262, 229-233 (1993).
- [28] F. Farges and G.E. Brown, Jr., "An Empirical Model for the Anharmonic Analysis of High-temperature XAFS Spectra of Oxide Compounds with Applications to the Co-ordination Environment of Ni in NiO, γ -Ni₂SiO₄ and Ni-bearing Na-disilicate Glass and Melt", *Chem. Geol.*, 128, 93-106 (1996).
- [29] M. Winterer, Proceedings of the 9th International Conference on X-ray Absorption Fine Structure (XAFS IX, Grenoble), *J. Phys IV France*, 7, 243 (1997).
- [30] J. Mustre de Leon, S.D. Conradson, A.R. Bishop, I.D. Raistric, I. Batistic, W.E. Jackson, G.E. Brown, Jr. and G.A. Waychunas, "XAFS Analysis in the Anharmonic Limit: Applications to Hi-T_c Superconductors and Ferrosilicates", in *XAFS VI, Sixth International Conference on X-ray Absorption Fine Structure*, S.S. Hasnain, ed., pp. 54-57, Ellis Horwood Ltd. Publishers, Chichester, UK (1991).
- [31] Z. Wu and F. Farges, "Anharmonicity Around Th in Crystalline Oxide-type Compounds. An In Situ, High-temperature XAFS Spectroscopy Study", *Physica*, B 266, 282-289 (1999).
- [32] N.E. Bibler, J.P. Bibler, M.K. Andrews and C.M. Jantzen, "Initial Demonstration of the Vitrification of High-level Nuclear Waste Sludge Containing an Organic Cs-loaded Ion-exchange Resin", *Mat. Res. Soc. Symp. Proc.*, Vol. 294, 81-86 (1993).
- [33] J.F. Stebbins, "Dynamics and Structure of Silicate and Oxide Melts: Nuclear Magnetic Resonance Studies", in *Structure, Dynamics, and Properties of Silicate Melts*, J.F. Stebbins, P.F. McMillan and D.B. Dingwell, eds., *Reviews in Mineralogy*, Vol. 32, pp. 191-246, Mineralogical Society of America, Washington, DC (1995).
- [34] N. Binstead, G.N. Greaves and C.M.B. Henderson, "An EXAFS Study of Glassy and Crystalline Phases of Compositions CaAl₂Si₂O₈ (Anorthite) and CaMgSi₂O₆ (Diopside)", *Contrib. Min. Petrol.*, 89, 103-109 (1985).
- [35] D.A. McKeown, G.A. Waychunas and G.E. Brown, Jr., "EXAFS and XANES Study of the Local Co-ordination Environment of Sodium in a Series of Silica-rich Glasses and Selected Minerals within the Sodium Aluminosilicate System", *J. Non-Crystal. Solids*, 74, 325-348 (1985).
- [36] W.E. Jackson, G.E. Brown, Jr. and C.W. Ponader, "X-ray Absorption Study of the Potassium Co-ordination Environment in Glasses from the NaAlSi₃O₈-KAlSi₃O₈ Binary: Structural Implications for the Mixed-alkali Effect", *J. Non-Crystal. Solids*, 93, 311-322 (1987).

- [37] M.C. Eckersley, P.H. Gaskell, A.C. Barnes and P. Chieux, "Structural Ordering in a Calcium Silicate Glass", *Nature* 335, 525-527 (1988).
- [38] J-M. Combes, G.E. Brown, Jr. and G.A. Waychunas, "X-ray Absorption Study of the Local Ca Environment in Silicate Glasses", in *XAFS VI, Sixth Internat. Conf. on X-ray Absorption Fine Structure*, S.S. Hasnain, ed., Ellis Horwood Ltd, Publishers, pp. 312-314 (1991).
- [39] T. Allard, P. Ildefonse, K. Beaucaire and G. Calas, "Structural Chemistry of Uranium Associated with Si, Al, Fe Gels in a Granitic Uranium Mine", *Chem. Geol.*, 158, 81-103 (1999).
- [40] F. Farges, G. Fiquet, J-P. Itie and D. Andrault, "A New Device for XAFS Data Collection up to 2 000 K (or 3 700 K Under Vacuum)", *Nucl. Instr. Meth. Phys.*, 101, 493-498 (1995).
- [41] F. Farges and G.E. Brown, Jr., "Co-ordination of Actinides in Silicate Melts", *J. de Physique IV, Colloque C2*, 1009-1010 (1997).
- [42] L. Pauling, "The Principles Determining the Structure of Complex Ionic Crystals", *J. Amer. Chem. Soc.*, 51, 1010-1026 (1929).
- [43] N.E. Brese and M. O'Keeffe, "Bond-valence Parameters in Solids", *Acta Crystallogr.*, B47, 192-197 (1991).
- [44] F. Farges, "Ordre local autour d'éléments fortement chargés dans des silicates amorphes: métamictes, vitreux et fondus" (*Structural Environments Around Highly-charged Cations in Aperiodic Oxide Structures: Radiation-damaged Minerals, Glasses and Melts*), Habilitation a diriger les recherches, Université Marne-la-Vallée (*in French w/abstracts in English*) (1994).
- [45] R.D. Shannon and C.T. Prewitt, "Effective Ionic Radii in Oxides and Fluorides", *Acta Crystallogr.*, B25, 925-945 (1969).
- [46] R.M. Hazen and L.W. Finger, "Comparative Crystal Chemistry", Wiley-Interscience, New York (1982).
- [47] F. Farges, C.W. Ponader and G.E. Brown, Jr., "Structural Environments of Incompatible Elements in Silicate Glass/Melt Systems: I. Zr at Trace Levels", *Geochim. Cosmochim. Acta*, 55, 1563-1574 (1991).
- [48] I.D. Brown, "Recent Developments in the Bond Valence Model of Inorganic Bonding", *Phys. Chem. Minerals*, 15, 30 (1987).
- [49] J.R. Bargar, S.N. Towle, G.E. Brown, Jr. and G.A. Parks, "Structure, Composition and Reactivity of Pb(II) and Co(II) Sorption Products and Surface Functional Groups on Single-crystal α -Al₂O₃", *J. Colloid Interface Sci.*, 85, 473-493 (1997).
- [50] S. Rossano, F. Farges, A. Ramos, J-M. Delaye and G.E. Brown, Jr., "Bond Valence Models in Silicate Glasses and Melts", Proc. First International Symposium on Non-crystalline Solids (*in press*) (2001).
- [51] J.R. Bargar, G.E. Brown, Jr. and G.A. Parks, "Surface Complexation of Pb(II) at Oxide-water Interfaces: I. XAFS and Bond-valence Determination of Mononuclear and Polynuclear Pb(II) Sorption Products on Aluminum Oxides", *Geochim. Cosmochim. Acta*, 61, 2617-2637 (1997).

- [52] I.D. Brown and R.D. Shannon, "Empirical Bond Strength-bond Length Curves for Oxides", *Acta Crystallogr.*, A29, 266-282 (1973).
- [53] I.D. Brown and D. Altermatt, "Bond-valence Parameters Obtained from a Systematic Analysis of the Inorganic Crystal Structure Database", *Acta Crystallogr.*, B41, 244-247 (1985).
- [54] G.E. Brown, Jr., G.V. Gibbs and P.H. Ribbe, "The Nature and Variation in Length of the Si-O and Al-O Bond in Framework Silicates", *Amer. Mineral.*, 54, 1044-1061 (1969).
- [55] D.A. McKeown, G.A. Waychunas and G.E. Brown, Jr., "EXAFS Study of the Co-ordination Environment of Aluminum in a Series of Silica-rich Glasses and Selected Minerals Within the Sodium Aluminosilicate System", *J. Non-Crystal. Solids*, 74, 349-371 (1985).
- [56] I.D. Brown, "Chemical and Steric Constraints in Inorganic Solids", *Acta Crystallogr.*, B 48, 553-572 (1992).
- [57] B.H.W.S. deJong and G.E. Brown, Jr., "Polymerization of Silicate and Aluminate Tetrahedra in Glasses, Melts and Aqueous Solutions: I. Electronic Structures of $\text{H}_6\text{Si}_2\text{O}_7$, $\text{H}_6\text{Al}_2\text{O}_7^{1-}$ and $\text{H}_6\text{Al}_2\text{O}_7^{2-}$ ", *Geochim. Cosmochim. Acta*, 44, 491-511 (1980).
- [58] H.A. Thompson, G.A. Parks and G.E. Brown, Jr., "Structure and Composition of Uranium(VI) Sorption Complexes at the Kaolinite-water Interface", in *Adsorption of Metals by Geomedia, Variables, Mechanisms and Model Applications*, E.A. Jenne, ed., pp. 349-370, Academic Press, New York (1998).
- [59] A.J. Dent, J.D.F. Ramsay and S.W. Swanton, "An EXAFS Study of Uranyl Ions in Solutions and Sorbed onto Silica and Montmorillonite Clay Colloids", *J. Colloid Interface Sci.*, 150, 45-60 (1992).
- [60] C.J. Chisholm-Brause, S.D. Conradson, C.T. Buscher, P.G. Eller and D.E. Morris, "Speciation of Uranyl Sorbed at Multiple Binding Sites on Montmorillonite", *Geochim. Cosmochim. Acta*, 58, 3625-3631 (1994).
- [61] E.R. Sylwester, E.A. Hudson and P.G. Allen, "Surface Interactions of Actinide Ions with Geologic Materials Studied by XAFS", *Mat. Res. Soc. Symp. Proc.*, 590, 9-16 (2000).
- [62] E.R. Sylwester, E.A. Hudson and P.G. Allen, "The Structure of Uranium (VI) Sorption Complexes on Silica, Alumina and Montmorillonite", *Geochim. Cosmochim. Acta*, 64, 2431-2438 (2000).
- [63] E.A. Hudson, L.J. Terminello, B.E. Vianni, M. Denecke, T. Reich, P.G. Allen, J.J. Bucher, D.K. Shuh and N.M. Edelstein, "The Structure of Uranium(VI) Sorption Complexes on Vermiculite and Hydrobiotite", *Clays and Clay Minerals*, 47, 439-457 (1999).
- [64] T. Reich, H. Moll, T. Arnold, M.A. Denecke, C. Hennig, G. Geipel, G. Bernhard, H. Nitsche, P.G. Allen, J.J. Bucher, N.M. Edelstein and D.K. Shuh, "An EXAFS Study of Uranium(VI) Sorption onto Silica Gel and Ferrihydrite", *J. Electron Spectrosc. Relat. Phenom.*, 96, 237-243 (1998).
- [65] J.R. Bargar, R. Reitmeyer and J.A. Davis, "Spectroscopic Confirmation of Uranium(VI)-carbonato Adsorption Complexes on Hematite", *Environ. Sci. Technol.*, 33, 2481-2484 (1999).

- [66] A. Manceau, L. Charlet, M.C. Boisset, B. Didier and L. Spadini, "Sorption and Speciation of Heavy Metals on Hydrrous Fe and Mn Oxides: From Microscopic to Macroscopic", *Appl. Clay Sci.*, 7, 201-223 (1992).
- [67] T.D. Waite, J.A. Davis, T.E. Payne, G.A. Waychunas and N. Xu, "Uranium(VI) Adsorption to Ferrihydrite: Application of a Surface Complexation Model", *Geochim. Cosmochim. Acta*, 58, 5465-5478 (1994).
- [68] P. Zhao, P.G. Allen, E.R. Sylwester and B.E. Viani, "The Sorption of Uranium(VI) and Neptunium(V) onto Hydrothermally Altered Concrete", *Radiochim. Acta.*, 88, 729-736 (2000).
- [69] E. Östhols, A. Manceau, F. Farges and L. Charlet, "Adsorption of Th on Amorphous Silica: An EXAFS Study", *J. Colloid Interface Sci.*, 194, 10-21 (1997).
- [70] J-M. Combes, C.J. Chisholm-Brause, G.E. Brown, Jr., G.A. Parks, S.D. Conradson, P.G. Eller, I. Triay and A. Meier, "EXAFS Spectroscopic Study of Neptunium(V) Sorbed at the α -FeOOH/Water Interface", *Environ. Sci. Technol.*, 26, 376-382 (1992).
- [71] J.R. Bargar, R. Reitmeyer, J.J. Lenhart and J.A. Davis, "Characterization of U(VI)-carbonato Ternary Complexes on Hematite: EXAFS and Electrophoretic Mobility Measurements", *Geochim. Cosmochim. Acta*, 64, 2737-2749 (2000).
- [72] C.C. Fuller, J.R. Bargar, J.A. Davis and M.J. Piana, "Mechanisms of Uranium Interactions with Apatite: Implications for Ground-water Remediation", *Environ. Sci. Technol.* (in review) (2001).

SOLVENT PHASE CHARACTERISATION OF LANTHANIDE(III) AND AMERICIUM(III) COMPLEXES WITH MALONAMIDE (TEMA) AND TERPYRIDINE LIGANDS BY EXAFS: COMPARISON WITH SINGLE CRYSTALS

C. Den Auwer,¹ M. Grigoriev,² C. Madic,³ M.T. Presson,¹ M. Nierlich,⁴ P. Thuery,⁴ F. David,⁵ S. Hubert,⁵ M.G.B. Drew,⁶ M.J. Hudson,⁶ P.B. Iveson,⁶ M.L. Russell⁶

¹CEA/Marcoule, DCC/DRRV/SEMP, BP 17171, F-30207 Bagnols-sur-Cèze, France

²Institute of Physical Chemistry, Moscow, Russia

³CEA/Saclay, DCC

⁴CEA/Saclay, DSM/DRECAM/SCM, Gif-sur-Yvette, France

⁵Institut de Physique Nucléaire, Orsay, France

⁶Reading University, Reading, UK

Abstract

In order to develop molecules that will be good candidates for the extractive separation of the various elements contained within nuclear fuels, 4f and 5f molecular chemistry has been the subject of numerous studies. Thus, to better understand the ligand to cation interaction and to fine tune the theoretical models, precise knowledge about the cation co-ordination sphere must be obtained. More precisely, both structural and electronic data must be acquired in order to define the role of the cation frontier orbitals within the complex. To do so, various structural probes must be used, from vibrational and nuclear techniques to X-ray spectroscopies. In the field of actinide solvent extraction, the species of interest are in the solvent phase and both solid state diffraction methods and solvent phase X-ray absorption spectroscopy have become of primary importance lately.

A number of Ln(III) and Am(III) complexes of the type $M(\text{NO}_3)_3\text{L}_{1,2}$ (where M is either Ln^{3+} or Am^{3+} and L is either the 2,2',6',2''-terpyridine (Tpy) or the N,N,N',N' tetraethylmalonamide (TEMA) ligand) have been crystallographically characterised in the solid state. In order to obtain structural information in the solvent phase, EXAFS L_{III} edge measurements have been performed on the cation (DCI ring at the LURE facility). The overall contraction (-0.05 Å) of the cation co-ordination sphere from Nd^{3+} to Lu^{3+} reflects the decrease in the lanthanide ionic radii. With the TEMA ligand, this steric constraint generates the elongation of one nitrate bond, leading to one formally monodendate nitrate for the late Ln ions. Comparison is made with the Tpy ligand.

In the case of Am^{3+} cation, comparison with isostructural Nd^{3+} shows that similar co-ordination spheres are obtained, either with the TEMA or the Tpy ligands.

Introduction

To better understand the role of the 4f and 5f orbitals in the bonding modes in lanthanide or actinide organocomplexes, it is essential to describe the electronic and geometric structures of the latter. We are working on the experimental and theoretical characterisation of actinide cations in order to fine tune the design of new ligands that would be good candidates for the minor actinide(III)/lanthanide(III) (An(III)/Ln(III)) separation. Fundamental data on lanthanide ions in the solvent phases have been the subject of wide interest in the literature. Ionic versus covalent relative character across the lanthanide series, inner or outer sphere complexation mechanisms in various solvent phases or structural characterisation of the Ln polyhedra are some of the problems to be addressed.

X-ray absorption spectroscopy (XAS) applied to actinide species has been greatly developed over the past decade and has been shown to be a very powerful technique to probe the lanthanide and actinide co-ordination sphere [1].

In this paper we present a summary of our current investigation of two series of lanthanide and americium complexes in solution with oxygen or nitrogen donor ligands: Ln(III) or Am(III)/3NO₃/2TEMA (in ethanol) and Ln(III)/3NO₃ (in pyridine) (Ln = lanthanide ions, Am(III) = trivalent americium and TEMA = N,N',N,N' tetraethylmalonamide). Details about these results can be found in the references [2].

Experimental

Absorption L_{III} edge spectra were recorded at both the LURE facility (Orsay, France) and the Daresbury facility (Daresbury, UK). A double crystal monochromator (Si 111 and Si 311) was used for data collection. Data extraction was carried out using a polynomial function and Fourier transformation was done in k³CHI(k) (2.5-10.7 Å⁻¹) using a Kaiser window. FEFF7 calculated phases and amplitudes were used.

Details concerning data collection, data extraction and data fitting are provided in the references [2].

Results and discussion

Malonamide (TEMA) complexes of Ln(III) and Am(III) in the presence of nitrate counter-ion

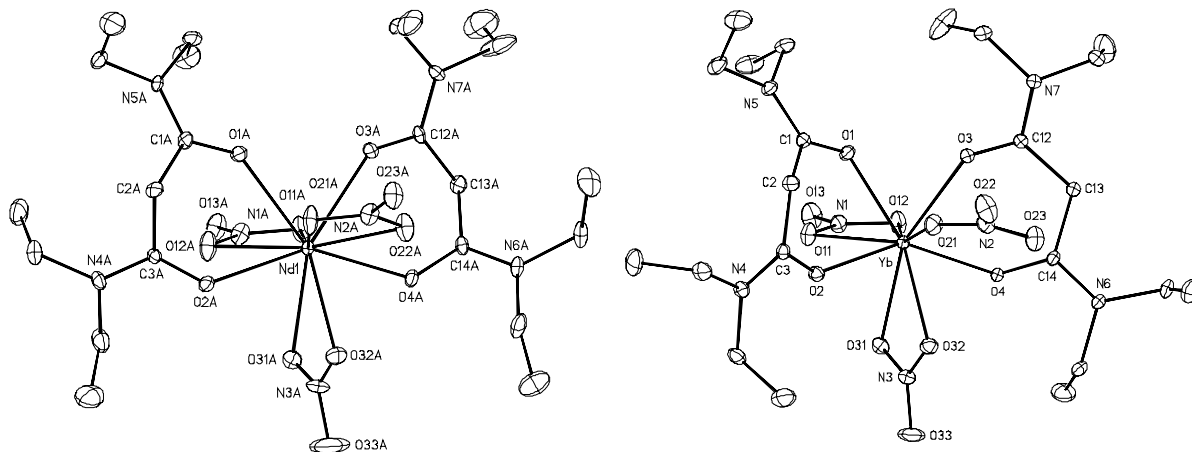
The solid-state structure of Nd(NO₃)₃TEMA₂ is consistent with the expected stoichiometry of complexes of TEMA with the Nd³⁺ ion and shows the bidentate behaviour of the malonamide ligands [Figure 1(a)] [2(a)]. The Nd-O distances for the O atoms of the nitrate ions located on each side of the plane defined by the TEMA molecules are systematically larger than those for the ions crossing the plane, indicating a stress between the TEMA molecules and two nitrate ions in the co-ordination sphere of the Nd³⁺ ion. The increase in such stress for the complex with the smaller ion (Yb³⁺) results in the change in co-ordination number and the occurrence of one monodentate nitrate ion [Figure 1(b)].

For the XAS spectra related to the solvent phase, all EXAFS adjustments have been carried out assuming as fitting initial conditions that six oxygen atoms are coming from the three nitrate groups and four oxygen atoms are coming from the two TEMA ligands, giving a non-fitted number of 10 oxygen neighbours. Even if this assumption does not account for likely co-ordinated water molecules coming from the hydration water molecules of the solid Ln(III) nitrates, it does satisfactorily account for the overall complex structure. The expected decrease of the averaged Ln-O bond length <Ln-O> for

Figure 1

(a) Molecular structure of $\text{Nd}(\text{NO}_3)_3(\text{TEMA})_2$; displacement ellipsoids are represented with 10% probability [2(a)].

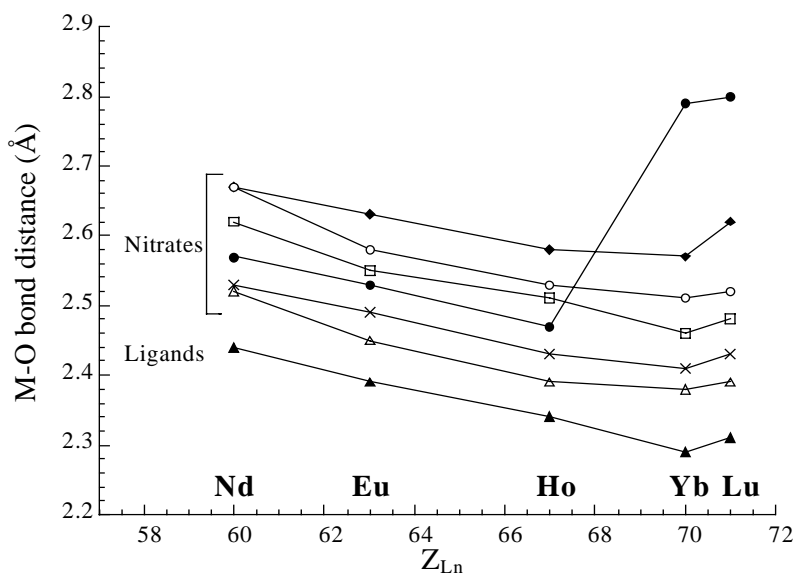
(b) Molecular structure of $\text{Yb}(\text{NO}_3)_3(\text{TEMA})_2$; displacement ellipsoids are represented with 10% probability [2(a)].



$\text{Ln} = \text{Nd, Eu, Ho, Yb, Lu}$ given by the EXAFS measurements is in agreement with the reduction of the Ln^{3+} ionic radius $r_{\text{Ln}^{3+}}$ when Z_{Ln} increases from Nd to Lu: $\langle \text{Ln-O} \rangle = 2.53 \text{ \AA}$ to 2.40 \AA and $r_{\text{Ln}^{3+}} = 1.107 \text{ \AA}$ (CN = 8) to 0.979 \AA (CN = 8) \AA , when $Z_{\text{Ln}} = 60$ to 71 , respectively [3] (Figure 2). Surprisingly, for the Yb and Lu cations, one of the oxygen atoms of one nitrate is moved away from the lanthanide first co-ordination sphere (to about 2.8 \AA). This result compares to the solid-state structure of $\text{Yb}(\text{NO}_3)_3(\text{TEMA})_2$, which is made up of one monodentate and two bidentate nitrates. However, in this solid-state structure, the two non-bonded oxygen atoms of the monodentate nitrate are located at 3.54 and 4.38 \AA from Yb.

Figure 2. M-O bond lengths in $\text{M}(\text{NO}_3)_3(\text{TEMA})_2$ solvent phase complexes ($\text{M} = \text{Nd, Eu, Ho, Yb}$ and Lu)

($\blacklozenge, \square, \bullet, \Delta, \times$) represent the six oxygen atoms of the three nitrates;
 \blacktriangle represents the averaged four oxygen atoms of the two TEMA ligands [2]



The value of 2.83 Å given by EXAFS is therefore low for a non-bonded oxygen of a monodentate nitrate and can only be explained by a strong tilt of the NO₃ entity away from the cation. In that sense, the lanthanide polyhedron may be viewed here as a 9+1 co-ordination mode instead of a 10 co-ordination mode for the Nd to Ho species.

A comparison was made in the solvent phase with the americium(III) complex. The americium(III) cation is often compared to that of Nd(III), as both ions are isostructural ($r_{Nd(III)} = 1.109$ Å, $r_{Am(III)} = 1.09$ Å, CN = 8) and have the same stable oxidation state (III). The EXAFS spectrum at the americium L_{III} edge has been fitted using the same structural assumptions as for Nd(NO₃)₃(TEMA)₂ and the averaged Am-O distances have been found to be 0.02 Å shorter than the average Nd-O distances. This confirms that the two cations form comparable complexes with O-bearing ligands with similar polyhedra in identical experimental conditions.

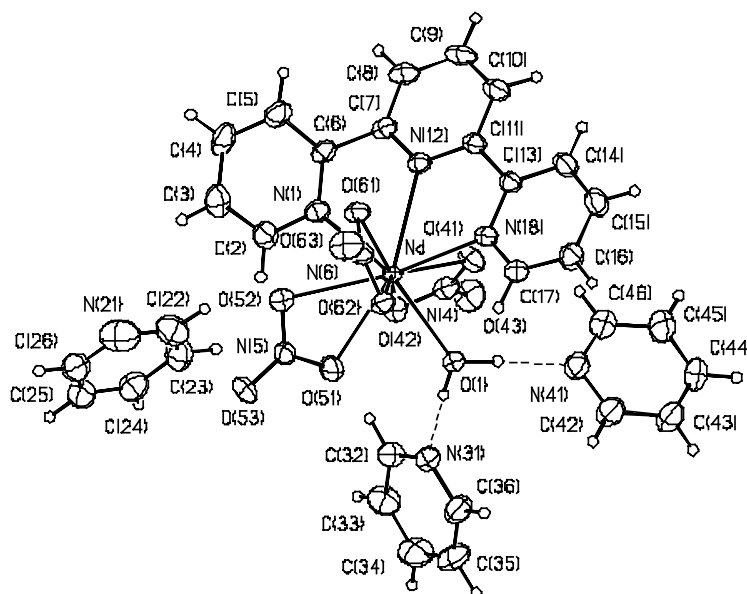
Terpyridine (Tpy) complexes of Ln(III)

The solid-state structure of [Nd(NO₃)₃TpyH₂O]·3Py [4] is a good structural model to study the lanthanide nitrate co-ordination sphere in pyridine (noted Py) since the Tpy ligand might be considered as an assembly of three pyridine molecules.

There is already in the literature a number of X-ray structural data for the lanthanide complexes with Tpy including those for nitrate-containing complexes with one to one Ln:Tpy molar ratio [5]. This complex is ten-co-ordinated (Figure 3) and contains a terdentate Tpy ligand, three bidentate nitrate anions and a co-ordination water molecule. The shortest distance in the Nd ion co-ordination polyhedron is that of Nd-O(H₂O), which is 2.396(2) Å. The Nd-N distances are from 2.553(2) to 2.5952(14) Å, the Nd-O distances for three bidentate nitrate groups are from 2.5045(14) to 2.5467(14) Å (five distances) and the sixth distance (for the O(52) atom) is 2.648(2) Å. The co-ordination polyhedron of the Nd(III) ion can be described as a distorted sphenocorona.

Figure 3. Molecular structure of [Nd(NO₃)₃TpyH₂O]·3Py

Displacement ellipsoids are represented with 10% probability [4]

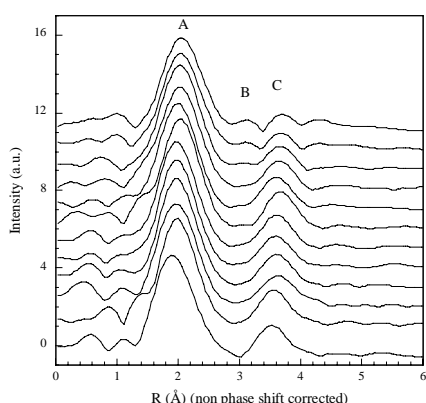


The Fourier transformed (FT) EXAFS data of the $\text{Ln}^{3+}/3\text{NO}_3^-$ complexes in pyridine are presented in Figure 4(a). As a starting assumption, the general formula of these complexes can be viewed as $\text{Ln}(\text{NO}_3)_n\text{Py}_m(\text{H}_2\text{O})_p$. Peak A accounts for the first lanthanide neighbours that are composed of n nitrate ligands ($0 < n \leq 3$), m pyridine molecules bound to the Ln(III) ion via their nitrogen atom ($m \geq 0$) and p water molecules ($p \geq 0$) that originate from the hydration water molecules of the solid Ln(III) nitrates used to prepare the solutions in Py. The decrease of Peak A distance to the absorbing atom agrees with the lanthanidic contraction as shown above for the $\text{Ln}/3\text{NO}_3^-/2\text{TEMA}$ complexes. In the second sphere, Peak B intensity decreases from Nd to Lu and Peak C intensity increases from Nd to Lu. To date, the origin of this behaviour is still not clear. However, the symmetry of the nitrate ligands may account for the second co-ordination sphere modification upon reduction of the cationic size since Peak C has been attributed to a multiple scattering resonance of the nitrate ions.

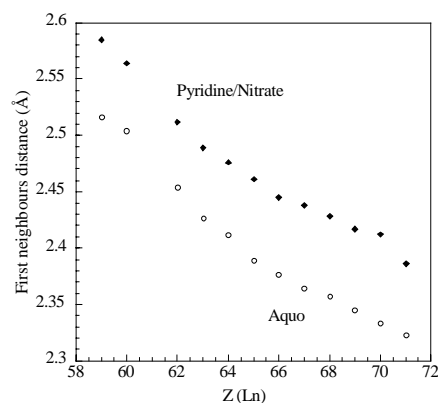
In Figure 4(b), a comparison is made between $\text{Ln}^{3+}/3\text{NO}_3^-$ systems in pyridine and $\text{Ln}^{3+}/3\text{Cl}^-$ systems in aqueous HCl solutions. In the latter, the chloride anions have been shown to be non-complexing [6] and the lanthanide cations are totally solvated by water molecules. Throughout the lanthanide series, the averaged Ln-O(N) distances are larger for $\text{Ln}^{3+}/3\text{NO}_3^-$ systems than for $\text{Ln}^{3+}/3\text{Cl}^-$ systems; this is attributed to the steric effect of the nitrate groups that form inner-sphere complexes in pyridine versus the water molecules in aqueous medium.

Figure 4

(a) FT of the lanthanide L_{III} edge in the $\text{Ln}(\text{NO}_3)_3\text{Py}_n(\text{H}_2\text{O})_p$ complexes in pyridine. From top to bottom: Pr, Nd, Sm, Eu, Gd, Tb, Dy, Ho, Er, Tm, Yb, Lu.



(b) Averaged Ln-O,N distances of the two series: $\text{Ln}(\text{NO}_3)_3\text{Py}_n(\text{H}_2\text{O})_p$ in pyridine and LnCl_3 in 1.0 M HCl aqueous solutions.



Conclusion

These preliminary results show the complexity of the structure of the lanthanide co-ordination sphere that depends on the counterion/solvent system. On the other hand, similar americium experiments are to be carried out for comparison with that of Nd.

In summary, EXAFS was found a very valuable tool for the understanding of the co-ordination modes of Ln(III) and Am(III) ions when involved in aqueous or non-aqueous solutions in interactions with O or N-bearing ligands. In such systems, solid-state model structures are indispensable to quantify the solvent phase structural evolutions.

This experimental technique will certainly have a bright future in studies in the field of nuclear hydrometallurgy.

REFERENCES

- [1] See for instance as an overview the Proceedings of the XAS-Actinide 1998 Conference, Grenoble, NEA/OECD publications (1999).
- [2] (a) C. Den Auwer, M.C. Charbonnel, M.G.B. Drew, M. Grigoriev, M.J. Hudson, P.B. Iveson, C. Madic, M. Nierlich, M.T. Presson, R. Revel, M.L. Russel and P. Thuéry, *Inorg. Chem.*, **39**, 1487 (2000).
- (b) C. Den Auwer, M.C. Charbonnel, M.T. Presson, C. Berthon, *Inorg. Chem.*, submitted.
- [3] (a) F. David, *J. Less Comm. Met.*, **121**, 27 (1986).
- (b) F. David and B. Fourest, *New. J. Chem.*, **21**, 167 (1997).
- [4] C. Den Auwer, M. Grigoriev, M.C. Charbonnel and M.T. Presson, to be published.
- [5] (a) M. Fréchette and C. Bensimon, *Inorg. Chem.*, **34**, 3520-3527 (1995).
- (b) M.G.B. Drew, M.J. Hudson, M.L. Russel, J-O. Liljenzin, M. Skålberg, L. Spjuth and C. Madic, *J. Chem. Soc., Dalton Trans.*, 2973-2980 (1998).
- (c) S.A. Cotton and P.R. Raithby, *Inorg. Chem. Commun.*, **2**, 86-88 (1999).
- (d) P.C. Leverd, M.C. Charbonnel, J-P. Dognon, M. Lange and M. Nierlich, *Acta Cryst.*, **C55**, 368-370 (1999).
- (e) M.G.B. Drew, M.J. Hudson, P.B. Iveson, C. Madic and M.L. Russel, *J. Chem. Soc., Dalton Trans.*, 2433-2440 (1999).
- [6] T. Yaita, H. Narita, S. Suzuki, S. Tachimori, H. Motohashi and H. Shiwaku, *J. Radioanal. Nucl. Chem.*, **239**, 371 (1999).

XAFS SPECTROSCOPY OF ACTINIDES IN THE SOLID STATE

Patrick G. Allen

Glenn T. Seaborg Institute for Transactinium Science, LLNL
Livermore, CA 94551

Abstract

Due to their complex electronic structure, actinides in solid-state systems display a number of unusual physical phenomena that are normally not observed in aqueous systems. Under appropriate conditions, X-ray absorption fine-structure spectroscopy (XAFS) is a sensitive probe, and can be used to study some of these effects. This paper will present recent results on: 1) anomalous background absorption effects in actinide oxides and metallic systems, 2) influence of electronic effects in XANES spectra and 3) lattice distortions observed in the temperature-dependent EXAFS spectra of alpha uranium.

Anomalous background absorption effects are observed at the L_{III} absorption edges of actinides in oxides (AnO_2 where $An=Th, U, Np$ and Pu) and metallic systems (U and Pu). These effects manifest themselves and appear as difficult to remove “low-R” features in the EXAFS Fourier transforms. Numerous theories have been proposed to explain similar features in other non-actinide systems, most of which are referred to as atomic XAFS (AXAFS) or multi-electron excitations (MEE). Independent of a fundamental assignment, techniques for their removal as well as trends in these oxide and metallic systems will be discussed.

Actinide L_{III} XANES spectra are, in principle, assigned to a $2p_{3/2} \rightarrow 6d$ transitions. In the electronic model, edge positions and white line intensities may be described in terms of effective charge densities and d -orbital occupancy at the valence level. However, features and trends in the XANES spectra of actinide metals and oxides indicate that the $5f$ electrons also have an important role. This is likely due to the proximity in energy of the $6d$ and $5f$ energy levels coupled with a breakdown in the dipole selection rules that results from relativistic effects dominating over spin-orbit coupling schemes. Effects are seen in U and Pu metal XANES spectra which may be attributed to $5f$ de-localisation relative to more localised behaviour observed in the oxide systems.

In the vicinity of 40 K, alpha uranium undergoes a subtle phase transformation which has been known and studied for many decades. The phase transformation, ascribed to a charge density wave phenomenon, is depicted by a lattice shift of specified U atoms within the orthorhombic lattice. U L_{III} -edge data were collected on this system as a function of temperature. The ability of EXAFS to discern lattice shifts of this nature in solid-state systems will be discussed.

**WHAT INFORMATION CAN BE OBTAINED FROM
XANES SPECTRA ABOUT THE LOCAL ATOMIC AND
ELECTRONIC STRUCTURES OF TRANSITION METAL OXIDES?**

**Rostislav Vedrinskii, Victor Kraizman, Alexander Novakovich,
Igor Maznichenko, Alexander Sakun, Alan Makoev**
Rostov State University, Rostov on Don, Russia

Abstract

Tc K-XANES calculated within one-electron full multiple scattering method for compounds with tetrahedral and octahedral co-ordinations of Tc atom are shown to be in good agreement with the experiment. Mechanisms which cause the pre-edge structure in transition metal K-absorption spectra in oxides are considered. It is shown that the pre-edge structure enables to obtain information about local atomic order and about occupation of d conduction bands in the crystal. The dependence of the energy of the main rise in Tc K-absorption spectra on interatomic distances, co-ordination numbers, and type of ligands are studied.

Introduction

X-ray absorption spectroscopy (XAS) is widely used for studies of local electronic and atomic structure of condensed matter. XAS can provide valuable information for crystalline solids as well as for amorphous materials and liquids, including dilute samples. Using hard X-rays one can perform *in situ* measurements at storage ring facilities. This possibility is extremely useful for studies of radioactive and hazardous materials.

X-ray absorption fine structure is separated naturally into two parts: EXAFS and XANES. The mechanisms responsible for the EXAFS formation are rather simple and as a result the direct methods were developed many years ago, enabling to obtain information on interatomic distances, co-ordination numbers, atomic numbers of the atoms near the absorbing one, and amplitudes of atomic vibrations. On the contrary, the mechanisms responsible for XANES formation are complicated and thus no direct method for XANES processing similar to that for EXAFS has yet been elaborated. Nevertheless there are some features in XANES which are used for the analysis of electronic structure and local atomic order around the absorbing atoms. We describe below the mechanisms of formation of such features in K-absorption spectra of transition metals (TM) in oxides and illustrate them using the Tc oxide spectra as examples.

The main rise of TM K-absorption cross-section in oxides occurs at about 10-20 eV above the conduction band (CB) bottom. The difficulty is that the local partial density of metal p states is small below the main rise since the low-energy CBs are constructed mainly by metal d -atomic orbitals (AO) with small admixture of oxygen O $2p$. Therefore the electron transitions from the TM K-level to the states originated from the d CBs cause low intensity features in spectra, which are usually called the pre-edge fine structure (PEFS). The $1s \rightarrow nd$ transitions are dipole forbidden for the free atoms but $1s$ electron excitations to d CBs can become dipole allowed in condensed matter due to an admixture of TM p states to the d ones. Since the degree of such an admixture and respectively the intensities of the PEFS peaks are very sensitive to the local atomic structure about the absorbing atom, PEFS can provide valuable information on this structure.

Three mechanisms are responsible for the PEFS formation [1]. The first is caused by excitations of the TM $1s$ electrons to the lowest unoccupied CBs of a crystal which are formed mainly by TM d AOs. The TM $1s$ electron transitions to these CBs are caused by the hybridisation of the diffuse p -symmetry orbitals of the absorbing TM atom with d AOs of the TM atoms close to the absorbing one and O $2p$ AOs. The energies of such MOs are weakly affected by the potential of X-ray core hole and the peaks in PEFS caused by this mechanism provide a sufficiently precise energy reference of the empty conduction bands arising from the corresponding MOs. This mechanism causes noticeable peaks in the PEFS only if neighbouring TMO_n polyhedrons share one or more oxygen atoms with the polyhedron containing the absorbing TM atom. The intensities of these peaks are determined by the type of octahedron conjunction in the crystal lattice. For example, in the perovskite structure crystals, such as PbTiO_3 , the PEFS peaks caused by transitions to the t_{2g} MOs of the near-by TiO_6 octahedrons are not observed at all or they are very weak, whereas transitions to the e_g MOs take place. On the other hand transitions to the both e_g and t_{2g} MOs of the near-by TiO_6 octahedrons take place in the case of rutile crystal.

The second mechanism is the well-known quadrupole transition mechanism, which allows direct transitions of the TM $1s$ electrons to the e_g and t_{2g} MOs of the TMO_n polyhedron containing the absorbing TM atom. Despite their weak intensities the peaks caused by this mechanism can be unambiguously identified in the experimental spectra of the single crystal sample due to the specific dependence of their intensities on the direction and polarisation of incident photons. Using this

dependence measured for single crystals it is possible to determine which d orbitals are empty and which are occupied. The studies carried out for the NiO single crystal [2] have shown that all the t_{2g} MOs are occupied whereas there are empty e_g MOs. The d MOs of the TMO_n polyhedron containing the absorbing TM atom are highly localised within its atomic sphere and, therefore, these MOs are strongly shifted down by the K-hole potential. The values of such shifts are about 3-4 eV.

The third mechanism causes the dipole transitions to the same MOs as the second. Such transitions are forbidden if absorbing atoms are disposed in the centrally symmetric positions but they can occur for the lack of inverse symmetry about the absorbing atoms, for example in the case of tetrahedral co-ordination of TM atoms. In the case of octahedral co-ordination of TM atoms, the inverse symmetry can be broken by static distortions or thermal vibrations. As a result e_g and t_{2g} MOs of the octahedron containing absorbing TM atom become weakly hybridised with p orbitals of this atom.

The difference of the energy position of the main edge in K spectra in different compounds, so-called chemical shift, is often associated with the variation of the K-level energy caused by changing the TM atom charge in a compound [3]. As a matter of fact this shift can also be caused by other reasons such as change of interatomic spacing, co-ordination number, atomic number of nearby atoms, and so on. The analysis of possible cases is carried out in the present paper.

For XANES calculations a traditional full multiple scattering method is used. It is described briefly in the next section. The multiple scattering method is the one-electron method, which seems to be unsuitable for calculating the spectra of TM atoms in paramagnetic state. Nevertheless it appears that using spin-dependent one-electron $X\alpha$ potential, one is able to calculate XANES in K-absorption spectra for magnetically ordered systems in good agreement with the experiment [4]. Spin-dependent potential calculated using the local spin-density prescription of von Barth and Hedin along with the Hedin-Lundqvist self-energy was employed for Fe K-edge XMCD [5].

Method for calculations

Using a one-electron approximation and including dipole and quadrupole terms of the photon-electron interaction operator one can express the X-ray absorption cross-section (XACS) for an atom in a polyatomic system through the photoelectron Green's function (GF) $G(\mathbf{r}, \mathbf{r}', \varepsilon)$ using the equation:

$$\sigma_i^0(\omega) = -8\pi \left(\frac{e^2}{\hbar c} \right) \hbar\omega \left[\text{Im} \int \varphi_i^*(\mathbf{r}) \mathbf{e} \mathbf{r} G(\mathbf{r}, \mathbf{r}', \varepsilon) \mathbf{e} \mathbf{r}' \varphi_i(\mathbf{r}') d^3r d^3r' \right. \\ \left. + \left(\frac{\omega}{2c} \right)^2 \text{Im} \int \varphi_i^*(\mathbf{r}) \mathbf{e} \mathbf{r} \cdot \mathbf{k} \mathbf{r} G(\mathbf{r}, \mathbf{r}', \varepsilon) \mathbf{e} \mathbf{r}' \cdot \mathbf{k} \mathbf{r}' \varphi_i(\mathbf{r}') d^3r d^3r' \right] \quad (1)$$

where $\sigma_i^0(\omega)$ is the cross-section of the photoionisation of the atomic core level i in the isolated atomic sphere number 0 by the linear polarised X-ray wave with the frequency ω , \mathbf{e} is the electric field vector (polarisation vector) of the X-ray wave, \mathbf{k} is its wave vector, $\varphi_i(\mathbf{r})$ is the wave function of the atomic level i , and ε is the photoelectron energy determined relatively to the *muffin-tin* (MT) zero (E_{MT}) of the crystal potential.

In order to calculate the GF in the continuum the full multiple scattering method [6-8] which employs MT approximation for the crystal potential is the most suitable. This method is based on the equation which connects the GF $G(\mathbf{r}, \mathbf{r}', \varepsilon)$ in the co-ordinate representation with the GF matrix $G_{LL'}^{mn}$ in

the so-called ‘‘orbital momentum-number of the atom’’ representation. We present this equation for the special case when both vectors \mathbf{r}, \mathbf{r}' are inside the same atomic sphere number 0:

$$G(\mathbf{r}, \mathbf{r}', \varepsilon) = G_0(\mathbf{r}, \mathbf{r}', \varepsilon) + f \sum_{L, L'} e^{i(\delta_l + \delta_{l'})} R_l(\varepsilon, r) Y_L(\hat{r}) G_{LL'}^{00} R_{l'}(\varepsilon, r') Y_{L'}(\hat{r}') \quad (2)$$

where $G_0(\mathbf{r}, \mathbf{r}', \varepsilon)$ is the GF for the isolated atomic sphere, $Y_L(\hat{r})$ is the real spherical harmonic $L = (l, m)$, \hat{r} is a unit vector directed along the vector \mathbf{r} , δ_l is the partial scattering phase shift for the electron wave with the orbital moment l scattered by the 0-th atomic sphere, f is a coefficient ($f = (2m/\hbar^2)^{3/2} \sqrt{\varepsilon}$), $R_l(\varepsilon, r)$ is a regular solution of the radial Schrödinger equation for the electron with the orbital moment l and the energy ε in the atomic sphere number 0. The solution $R_l(\varepsilon, r)$ is normalised on the surface of the atomic sphere by the following boundary condition:

$$R_l(\varepsilon, r_0) = j_l(kr_0) \cos \delta_l - n_l(kr_0) \sin \delta_l \quad (3)$$

where r_0 is the radius of the atomic sphere 0, k is the electron wave number, and j_l and n_l are the spherical Bessel and Neuman functions.

Substituting Eq. (2) into Eq. (1) the XACS can easily be expressed through the GF matrix $G_{LL'}^{00}$. For instance, the expression for the K-XACS obtained within the dipole approximation is the following:

$$\begin{aligned} \sigma_K^0(\omega) = & \left[8\pi\hbar\omega \left(\frac{e^2}{\hbar c} \right) \right] \left(\frac{2m}{\hbar^2} \right)^{3/2} \sqrt{\varepsilon} \left| \int \phi_{1s}(r) r^3 R_1(\varepsilon, r) dr \right|^2 \\ & \cdot \sum_{i,j=1}^3 e_i e_j \text{Im} \sum_{m,m'=-1}^1 (i\delta_{mm'} - G_{mm'}^{00} e^{2i\delta_1}) S_{mi} S_{m'j} \end{aligned} \quad (4)$$

where $S_{mi} = \int Y_{1m}(\hat{r}) \hat{r}_i Y_{00}(\hat{r}) d^2\hat{r}$.

For calculating the GF matrix $G_{LL'}^{n0}$ the following system of linear algebraic equations should be solved [6,7]:

$$G_{LL'}^{n0} = g_{LL'}^{n0} + \sum_{n', L'} g_{LL'}^{nn'} t_{r'}^{n'} G_{L'L'}^{n'0} \quad (5)$$

where t_l^n is the partial scattering t -matrix for the n -th atom in the crystal and the electron orbital moment l , $g_{LL'}^{nn'}$ is the coefficient in the bicentral expansion for the free electron GF.

The core hole influence on the absorbing atom potential breaks the translational symmetry of the crystal potential and the system of Eq. (5) can be solved in this case if one employs the cluster approximation for the crystal and, besides, restricts the number of the orbital moments included in the summation in Eq. (5). The correct choice of the representative cluster is the important point of the full multiple scattering method [1]. To include the finite lifetime of the electron-hole pair appearing at the final stage of the photoionisation process we have smeared the spectra taking into account that the photoelectron lifetime in the medium rapidly decreases with the increase of the photoelectron energy ε .

The cluster potential construction

In the present paper as in the previous one [1] we approve a semi-empirical non-self-consistent approach to the cluster potential construction assuming that the most important point for the XANES calculations is keeping the correct values of the relative energies of the atomic valence levels and/or atomic scattering resonances for different atoms in the crystal. The potential inside an atomic sphere is considered to be a sum of a free atom self-consistent potential and a constant value (potential shift) simulating both the Maudelung potential and the change of the potential caused by redistribution of the electron density inside the atomic sphere. To estimate the potential shifts one can compare the energies of the atomic levels with those determined by the self-consistent band calculations or with some experimental data. The potential outside the cluster is considered to be equal to the average interstitial potential (MT-zero). This means that we ignore the reflection of the electron waves from the atoms being outside the cluster chosen.

The electron density inside each atomic sphere is considered to be equal to that of the corresponding free atom obtained with the usual Herman-Skillman procedure [9] using the exchange parameter α taken according to the Schwarz prescription [10] ($\alpha \approx 0.75$). At the same time the potentials used for the t -matrix calculations for the vacant electron states in the continuum are determined using $\alpha \approx 0.5$ - 0.6 which is slightly decreased in comparison with that of Schwarz. Schwarz has chosen the α value in order to fit the occupied state energies to those of Hartree-Fock, consequently the X_α potential for the occupied electron states really includes two terms: the first one simulates the exchange potential and the second cancels the electron self-interaction. Of course, the second term should be excluded for calculating the vacant electron state wave functions in the continuum. To do this in a simple way we propose to decrease the α value.

The electron configurations for all the atoms in the cluster excluding the absorbing one are chosen to coincide with those for the neutral free atoms in the ground state. The configuration of the absorbing atom has been chosen to include extra atomic screening of the core hole. In the case of the metals or covalence crystals the complete extra atomic screening leads to the increase of the valence shell occupation by one electron ($Z+1$ model) [11]. In the case of ionic-covalent crystals the screening charge should be slightly less than the whole electron charge. It is worth noting that self-consistent cluster calculations systematically overestimate the screening charge in such crystals. It is clearly observed in calculations of Ti K XANES in PbTiO_3 [8], where the energy of the pre-edge structure and its shape are not in accordance with the experiment. Such calculations do not allow carrying out the analysis of the pre-edge structure. Thus, we consider the screening charge as an adjustment parameter [1,12,13]. It was shown that the best agreement with the experimental K-XANES in the case of the d metal oxides is reached if one increases the d -shell occupation of the ionised TM atom by 0.8 electron. Such a result seems to be quite reasonable. This model of the core-hole potential is called the model of incomplete extra atomic screening. Of course, it should be understood that this model can not be justified rigorously. We use it for the simple simulation of the complicated dynamic processes which occur during X-ray absorption. Nevertheless our studies have shown that the model proposed enables us to calculate the TM K-XANES for various TM oxides in good agreement with the experiment [1,12,13].

Some additional complications occur for the compounds containing TM atoms in a paramagnetic state. These complications are caused by interaction of photoelectron with the unfilled d shell of an absorbing atom and necessitate taking into account Pauli's principle with the one-electron calculation method. We assume in the present paper that electron-electron interaction leads only to some additional smearing of the pre-edge structure. We will explain how to include Pauli's principle using as an example the Tc K-spectrum of TcO_2 .

Comparison of calculations with experimental spectra for Tc K-edge

Tc K-edge XANES in compounds with tetrahedral co-ordination: p-d-f mixture

The accuracy of the multiple scattering method based on MT approximation for the cluster potential for calculating Tc absorption spectra is not evident beforehand, especially in the pre-edge region, due to the large radius of $4d$ -wave function of Tc atom. Therefore calculations of the spectra with unambiguous interpretation of pre-edge singularities are good tests for validity of the proposed approach. A common feature of all the K-edge XANES of $3d$ or $4d$ TM atoms in tetrahedral environment is a noticeable peak in the pre-edge region. The origin of this peak is absolutely clear. The lowest unoccupied molecular orbitals (LUMO) of TMO_4 tetrahedron constructed from metal $3d$ ($4d$) states and ligand p states have a great admixture of metal p states because x , y , z states and xy , yz , xz states are transformed within the same irreducible representation of T_d group. Therefore transitions of $1s$ electron to these LUMO are allowed by dipole selection rules and intensities of such transitions are great.

Spectra chosen for the analysis are Tc K-XANES of a liquid sample 1.3 mMol/L $\text{NaTcO}_4(\text{aq})$, and of a crystal KTcO_4 [14]. EXAFS analysis shows that the Tc atom in the solution is surrounded by four oxygen atoms at a distance of $1.72 \pm 0.01 \text{ \AA}$ [14]. The XANES for this compound is calculated employing the five-atomic cluster TcO_4 with oxygen atoms disposed in apexes of regular tetrahedron and Tc-O separation equals 1.72 \AA . The crystal lattice of KTcO_4 is constructed by tetrahedrons TcO_4 with Tc-O separation 1.71 \AA . Different tetrahedrons have no common oxygen atoms. Tc K-XANES for KTcO_4 is calculated employing the 55-atomic cluster $(\text{TcO}_4)\text{K}_{10}(\text{TcO}_4)_8$. Scattering phase shifts with $l \geq 3$ for Tc, with $l \geq 2$ for K, and with $l \geq 1$ for O atoms are included. The model of the cluster potential described above is employed. Comparison of the calculated and experimental spectra is presented in Figure 1. The intensities of experimental spectra are normalised in order to provide the same absorption step as calculated spectra. The energy of Peak A in the experimental spectra is adjusted to that of the calculated ones. Calculated spectra are convoluted with Lorentz function. Its full width equals 7 eV in the region of the pre-edge peak. One can see that the energy splitting between Peaks A and C and the intensity of Peak A relative to the atomic background absorption in both cases are excellently reproduced in calculations.

To understand the origin of Peaks B and C we calculated the spectrum of TcO_4 in the same cluster assuming that f -partial scattering phase shift at Tc atom equals zero and comparing the result with the previous calculations. This comparison is presented in Figure 2 along with the f -partial scattering phase shift (spectra in Figure 2 are not smeared for clarity.) The behaviour of the f -scattering phase shift testifies to the existence of f resonance at an energy of about 40 eV above MT-zero level. It is evident that inclusion of the f -scattering phase shift causes the appearance of additional features with the complicated shape in K-spectrum at an energy close to that of f -resonance. Thus one observes in Tc K-spectra in tetrahedral co-ordination the effect caused by mixture of Tc p states with the both Tc d and f states. We call this phenomenon p - d - f mixture. Peaks B and C are pronounced better in the spectra of a crystal than in those of a complex because the f resonance influences on these spectra not only via p - f mixture at the absorbing atom but also via sharp changing of scattering characteristics of neighbouring TcO_4 tetrahedrons.

Tc K-edge XANES in TcO_2

TcO_2 crystal has a rutile-like crystal structure. In this structure each Tc atom is surrounded by six oxygen atoms, which form slightly distorted octahedrons. Therefore the p - d mixture will weakly influences the Tc K-spectra. On the contrary, since in rutile structure nearby TMO_6 octahedrons share

Figure 1. Tc K-XANES in TcO₄ complex (1.3 mMol/L NaTcO₄(aq)) (left panel) and in KTcO₄ crystal (right panel)

Experiment [14]: open circles, calculations: solid line. Calculated absorption cross-sections are given in Mb, experimental spectra in arbitrary units. Energy reference of experimental spectra is chosen to fit the position of Peak A.

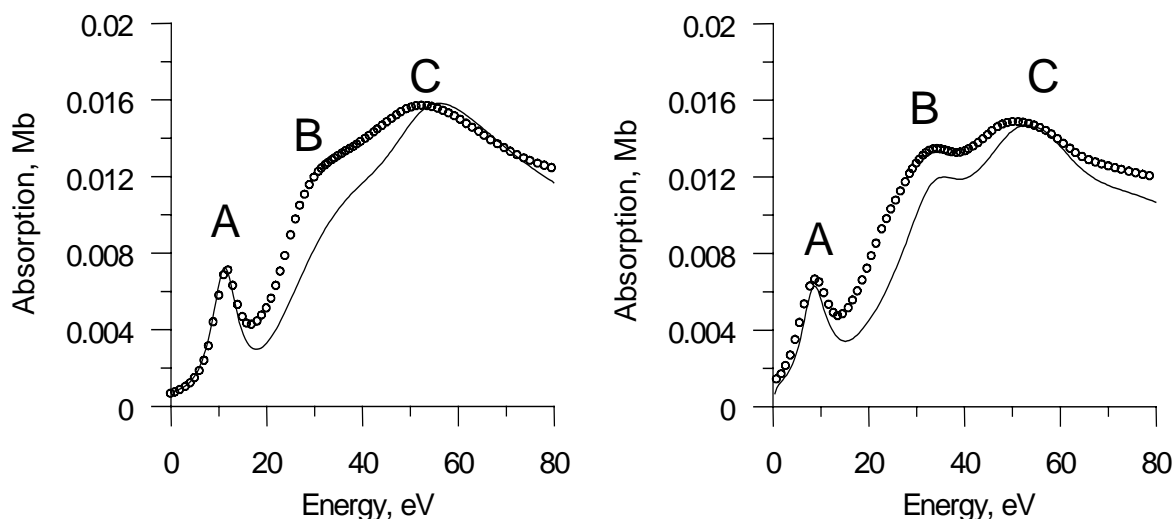
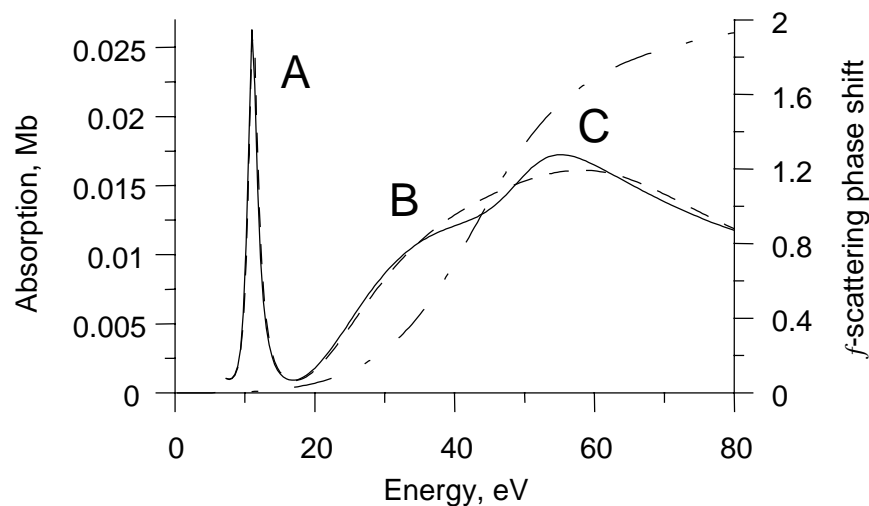


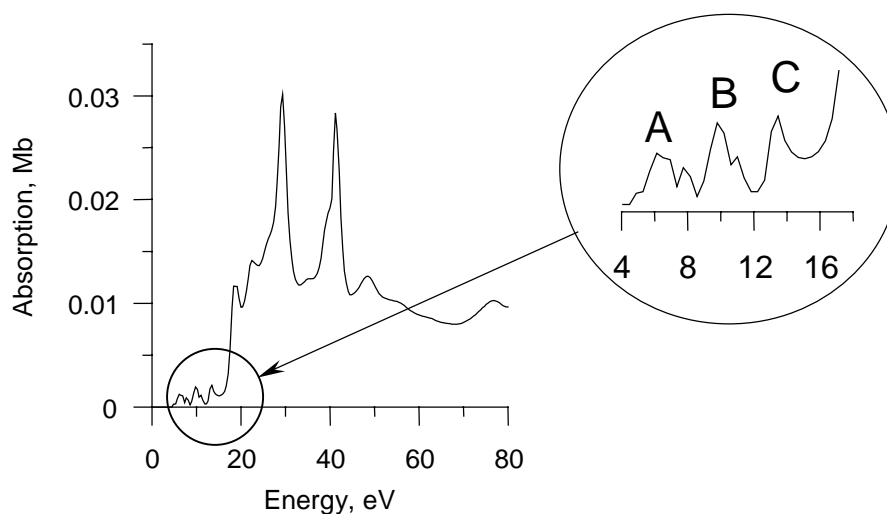
Figure 2. The influence of Tc f-scattering resonance on Tc K-spectrum in TcO₄ complex

δ_f -f partial scattering phase shift: dashed-dotted line; unsmearred Tc K-spectrum: solid line; the same spectrum calculated assuming $\delta_f = 0$: dashed line



common apexes and edges, the transitions to the neighbouring octahedrons have to take place. The Tc K-absorption spectrum is calculated for 55-atomic cluster which contains 11 complete TcO₆ octahedrons: the central one containing absorbing Tc atom, and all the octahedrons which share at least one oxygen atom with the former. The Tc atom in TcO₂ crystal has three 4d electrons which fill MOs with t_{2g} symmetry. We assume for simplicity that spin moments of all Tc atoms in the crystal have the same direction. The spectrum calculated for the case of unpolarised radiation and only dipole transitions being taken into account is presented in Figure 3. Unsmearred spectrum consists of a great

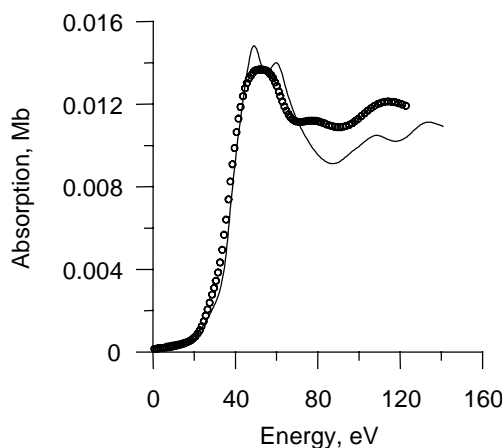
Figure 3. Unsmear Tc K-spectrum in TcO₂ crystal; enlarged pre-edge structure is shown in inset



number of narrow peaks. Such structure is typical for rutile-like crystals. The pre-edge is shown enlarged in the inset. Peak A is caused by the excitations of the Tc K-electron to the t_{2g} MOs of the neighbouring octahedrons, whereas Peak B is caused by the excitations to the e_g ones. To prove this statement we have changed slightly the potential shift for neighbouring Tc atoms. Energies of Peaks A and B change together with the potential shifts. At the same time, changing the potential shift for the absorbing Tc atom or for O atoms practically does not affect the energies of Peaks A and B. Unfortunately, we could not find a simple interpretation for Peak C. The GF multiple scattering one-electron method yields transitions to both empty and filled final state. Since only three of six t_{2g} MOs are empty one has to include Peak A into the resulting spectrum with a weight equalling 0.5. The comparison of the smeared calculated spectrum with the experimental one [14] is presented in Figure 4. The great width of K-level for Tc atom along with instrumental resolution leads to the transformation of the distinct Peaks A, B and C into weak though visible features at the beginning of the main rise of the spectra.

Figure 4. Tc K-XANES in TcO₂ crystal

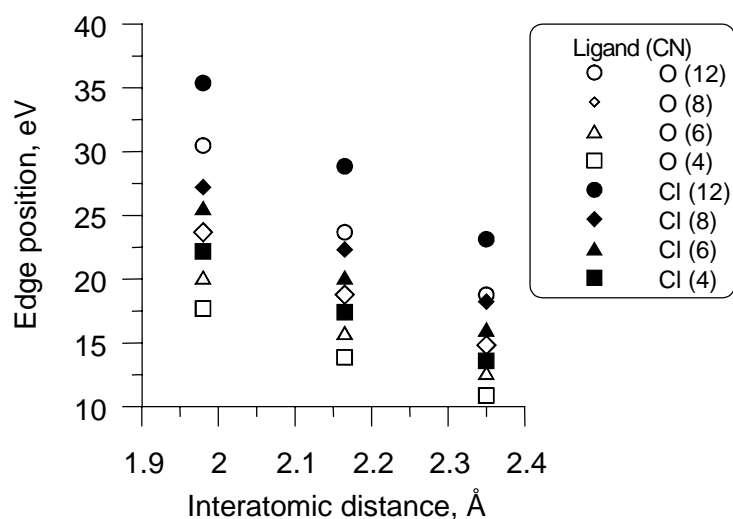
Experiment [14]: open circles, calculations: solid line. Calculated absorption cross-sections are given in Mb, experimental spectra in arbitrary units. Energy reference of experimental spectra is chosen to fit the main rise position.



Dependence of Tc K-edge main rise on the nearest environment

The energy of the main rise of the K-absorption spectra of the identical TM atoms in different compounds may significantly differ from each other. This shift, often called a chemical shift of the K-edge, is often employed for determination of the oxidation state of TM atoms in compounds [3]. Meanwhile the shift is determined not only by the change of the binding energy of K-level but also by the change of spacing, co-ordination numbers, atomic numbers of the atoms near the absorbing atom, etc. In order to study the influence of short-range atomic order on the energy of the main rise we have carried out model calculations of the K spectra for the clusters TcL_n where $L = O$ or Cl ; $n = 4, 6, 8, 12$. The clusters used are regular polyhedrons with n apexes and Tc-L distances equal to 1.98, 2.35 and 2.165 Å. The first distance is characteristic for Tc-O bond length in TcO_2 whereas the second for Tc-Cl in $(NH_4)_2TcCl_6$ [15]. We should like to emphasise that the potential inside Tc atomic spheres and in the interatomic region remains unchanged in all the clusters, thus only the influence of interatomic distances, co-ordination numbers and kinds of ligand atoms has been studied. As usual, the energy of the inflection point at the main rise was considered as the edge position. The results of the calculations are presented in Figure 5. One can conclude that all the factors mentioned above significantly change K-edge energy. The results obtained explain the K-edge shift for spectra of TcO_2 and $(NH_4)_2TcCl_6$ where Tc atoms have the same valence. As follows from Figure 5, this shift equals about 4 eV which is in reasonable agreement with the experiment [15]. It seems that the well-known correlation between TM atom oxidation state and chemical shift of the K-absorption edge is mainly caused not by the change of the TM atom electric charge but by the change of the distance between these atoms and nearby anions.

Figure 5. The dependence of the main rise position in the Tc K-spectrum of TcL_n cluster. $L = O, Cl$; $n = 4, 6, 8, 12$.



Conclusion

The analysis of the PEFS in TM K-spectra in oxides enables to obtain direct information about the symmetry of TM co-ordination polyhedron, small displacements of TM atom from the centre of the TMO_6 octahedron, type of linkage of TMO_n polyhedrons in the crystal lattice. The experimental studies of the chemical shift of TM K edge together with the theoretical calculations of the main rise shape enable to determine the oxidation state of TM atoms in different compounds.

Acknowledgement

These studies were supported by RFBR grant 00-02-17683.

REFERENCES

- [1] R.V. Vedrinskii, V.L. Kraizman, A.A. Novakovich, Ph.V. Demekhin, *et al.*, *J. Phys.: Condens. Matter*, 10, 9561 (1998).
- [2] D. Heumann, G. Dräger, S. Bocharov, *J. de Physique IV France*, 7, C2-481 (1997).
- [3] I. Almahamid, J. Bryan, J. Bucher, A. Burrell, *et al.*, *Inorganic Chem.*, 34, 193 (1995)
- [4] R.V. Vedrinskii, V.L. Kraizman, A.A. Novakovich, Sh.M. Elyafi, *et al.*, to be published.
- [5] A.L. Ankudinov, J.J. Rehr. *Phys. Rev.*, B 56, R1718 (1997).
- [6] R.V. Vedrinskii, A.A. Novakovich, *Fiz. Metall. Metallovedenie.*, 39, 7 (1975).
- [7] C.A. Ashley, S. Doniach, *Phys. Rev.*, B 11, 1279 (1975).
- [8] A.L. Ankudinov, B. Ravel, J.J. Rehr, S.D. Conradson, *Phys. Rev.*, B 58, 7565 (1998).
- [9] F. Herman, S. Skillman, "Atomic Structure Calculation", (Englewood Cliffs, NJ: Prentice-Hall, 1963).
- [10] K. Schwartz, *Phys. Rev.*, B 5, 2466 (1972).
- [11] A. Bianconi, M. Dell'Arriccia, A. Gargano, C.R. Natoli, in *EXAFS and Near Edge Structure*, A. Bianconi, L. Incoccia and S. Stipcich, eds. (Springer-Verlag, Berlin, 1983), p. 57.
- [12] B. Poumellec, V. Kraizman, Y. Aifa, R. Cortes, *et al.*, *Phys. Rev.*, B 58, 6133 (1998).
- [13] B. Ravel, E.A. Stern, R. Vedrinskii, V. Kraizman, *Ferroelectrics*, 206-207, 407 (1998).
- [14] T. Reich, H. Funke, C. Hennig, A. Roßberg, *et al.*, to be published.
- [15] P.G. Allen, G.S. Siemering, D.K. Shuh, J.J. Bucher, *et al.*, *Radiochim. Acta*, 76, 77 (1997).

THE REDOX SPECIATION OF NEPTUNIUM IN ACIDIC AND ALKALINE SOLUTIONS

L. Soderholm,¹ M.R. Antonio,¹ C.W. Williams,¹ J.C. Sullivan,¹ S.R. Wasserman,² J-P. Blaudeau³

¹Chemistry, ²XFD Divisions, Argonne National Laboratory, Argonne IL 60439 USA

³Ohio Supercomputer Centre, ASC-HP, 2435 West 5th St.B76, WPAFB,OH 45433 USA

Abstract

Newly developed *in situ* capabilities at the Advanced Photon Source have been used to obtain X-ray absorption spectroscopy (XAS) data from Np in aqueous solutions. L-edge XAS data have been obtained from acidic solutions in which Np was electrochemically stabilised in the (III) to (VI) states. A purpose-built electrochemical cell [1] housed in appropriate safety containment allows the acquisition of XAS data while the solution is maintained under controlled applied potentials. This electrochemical cell has been used in a proof-of-concept experiment designed to demonstrate the use of X-ray absorption near-edge structural (XANES) data for the determination of thermodynamic formal potentials. XANES data were obtained at a series of applied potentials from a 1 M perchloric acid solution containing 5 mM Np. The relative concentrations of Np redox species as a function of applied potential were extracted from the data using principal component (factor) analyses. The formal potentials determined for the Np(VI)/Np(V) and Np(IV)/Np(III) couples agree with those previously published. Extended X-ray absorption fine structure (EXAFS) data were obtained from the same solution, held at potentials chosen to optimise the concentration of a single Np redox species [2]. These data have been used to verify the co-ordination environment of Np ions as a function of oxidation state. Density functional theory (DFT), simple geometric modelling and results from the EXAFS data analysis are in agreement for the co-ordination environment of Np(III).

In a related set of experiments, L-edge XAS data of Np(V), Np(VI) and Np(VII) were obtained from a basic solution. The Np oxidation state was varied by sparging the solution with ozone. Data were collected as the sample was sparged and also after the sparging gas was turned off. Np optical data were obtained in the same XAS cell and confirm the oxidation of Np(VI) to heptavalent Np. The concentration of Np(VII) was determined using trivalent Cr as a quantitative reductant. The Np(VII) co-ordination environment determined from both the XANES and the EXAFS data analyses are consistent with a previously reported NMR data interpretation [3]. DFT calculations on the co-ordination environment of Np(VII) support the experimental results.

Acknowledgements

This work is supported by the US DOE, Basic Energy Sciences, Chemical Sciences, under contract No. W-31-109-ENG-38. JPB acknowledges support from the Ohio Supercomputer Centre.

REFERENCES

- [1] L. Soderholm, M.R. Antonio, C.W. Williams, S.R. Wasserman, *Anal. Chem.*, 71, 4622-4628 (1999).
- [2] M.R. Antonio, L. Soderholm, C.W. Williams, J-P. Blaudeau and B.E. Bursten (submitted).
- [3] E.H. Appelman, A.G. Kostka and J.C. Sullivan, *Inorg. Chem.*, 27, 2002-2005 (1988).

QUANTUM CHEMICAL CALCULATIONS ON STRUCTURES OF ACTINIDE COMPLEXES

Satoru Tsushima,* Tobias Reich
Institut für Radiochemie
Forschungszentrum Rossendorf
Germany

Abstract

The results of our recent theoretical calculations on the structures and the hydration numbers of actinide complexes are discussed together with EXAFS data. The hydration number determined from the calculated Gibbs free energy (inclusive of the solvation energy) was found to be different from the hydration number determined from the electronic energy at 0 K, 0 atm. The roles of entropy and solvation energy were found to be important with regard to the stability of the actinide complexes. The structures of the aqueous uranyl complexes obtained by EXAFS measurements were compared with the structures obtained by “gas phase” quantum chemical calculations. The importance of including the secondary co-ordination shell and counter-ions is discussed in this paper.

* On leave of absence from the Department of Quantum Engineering and Systems Science, The University of Tokyo, Japan.

Introduction

Quantum chemical *ab initio* calculations are capable of predicting various properties of molecules, including the structures, vibrational frequencies, formation energy and so on. Calculated properties are quite useful to gain further insight into actinide co-ordination chemistry. In order to do this, however, it is crucial to comprehend the correspondence between the calculated properties and those obtained by experiments. The purpose of the present work is to perform *ab initio* calculations of the actinide (uranium) complexes, determine their structures and co-ordination numbers, and to discuss the validity of the theoretical method for studying actinide complexation. This paper mainly consists of three parts. First, the co-ordination number of the uranyl ion, second the structure of the uranyl dimeric complex and third the structure of the uranyl carbonate complex.

Calculations

The GAUSSIAN 98 package of programs [1] was used for the calculations, which are based on density functional theory (DFT). The B3LYP hybrid density functional method (Becke's three-parameter hybrid functional using the LYP correlation functional [2,3]) was used since this method is known to reproduce accurate geometries and thermochemistries for uranium (VI) complexes [4,5]. Spin-orbit effects were not included since they are less important for the closed shell system that is considered here.

The calculations employed Hay's effective core potential (ECP) and corresponding basis set (without g function) for the uranium atom. The uranium core comprises the electrons in all shells up to and including the $4f^{14}$ and $5d^{10}$ shells leaving the outer $6s^2 6p^6$ and the outer six valence electrons ($5f, 6d, 7s, 7p$) treated explicitly using a $[3s 3p 2d 2f]$ contracted Gaussian basis. The 6-31G* basis set was used for oxygen, and the 6-31G basis was used for hydrogen [6] during the optimisation calculations. The 6-31++G* basis set was used for oxygen and the 6-31++G** basis was used for hydrogen [7] for the energy calculations. The geometries were not restricted to symmetry constraints and were fully optimised.

Zero point energy correction and thermal corrections (vibrational, rotational and translational) were made to the electronic energy:

$$E = E_{elec} + ZPE + E_{vib} + E_{rot} + E_{trans}$$

Gibbs free energy G was calculated from:

$$H = E + RT$$

$$G = H - TS$$

where R is the gas constant, T is the temperature, H is the enthalpy and S is the entropy. The entropy was calculated from the temperature-dependent partition function.

The solvation energy was calculated using the Polarised Continuum Model (PCM) method developed by Tomasi and co-workers [8]. Scaling factor 1.2 was used for the definition of the solvent accessible surface of all elements except hydrogen. Thus, the radius of each atomic sphere was determined by multiplying the van der Waals radius by the scaling factor. Since the pressure parameter $p = 1$ atm used by the GAUSSIAN 98 program corresponds to the hypothetical ideal gas

phase pressure, the pressure parameter $p = 1\ 354$ atm was used to reproduce the entropy effect of concentration on Gibbs energy in aqueous solution [9]. It is calculated from $p = \rho_w RT$ and $\rho_w = 997$ kg/m³, which corresponds to the experimental density of liquid water at room temperature.

Hydration number of uranyl ion

According to previous theoretical studies [10,11], the hydration number of the UO_2^{2+} ion is 5. Therefore in the present paper, the clusters of $\text{UO}_2(\text{H}_2\text{O})_5^{2+}$ and $\text{UO}_2(\text{H}_2\text{O})_6^{2+}$ were investigated. Three different structures were compared for each cluster.

For $\text{UO}_2(\text{H}_2\text{O})_5^{2+}$, the three different structures being examined are:

- 1) Five water molecules are in the first solvation shell around the UO_2^{2+} ion [$\text{UO}_2^{2+} \cdot 5\text{H}_2\text{O}$, Figure 1(a)].
- 2) Five water molecules bond to the UO_2^{2+} ion but there are four water molecules in the first solvation shell and one water molecule in the second solvation shell [$\text{UO}_2^{2+} \cdot 4\text{H}_2\text{O} \cdot \text{H}_2\text{O}^{**}$, Figure 1(b)].
- 3) Four water molecules are in the first solvation shell around the UO_2^{2+} ion and one water molecule bonds to the first shell water molecule through hydrogen bonding [$\text{UO}_2^{2+} \cdot 4\text{H}_2\text{O} \cdot \text{H}_2\text{O}^*$, Figure 1(c)].

For $\text{UO}_2(\text{H}_2\text{O})_6^{2+}$, the three different structures being examined are:

- 1) Six water molecules are in the first solvation shell around the UO_2^{2+} ion ($\text{UO}_2^{2+} \cdot 6\text{H}_2\text{O}$).
- 2) Six water molecules bond to UO_2^{2+} ion, but there are five water molecules in the first solvation shell and one water molecule in the second solvation shell ($\text{UO}_2^{2+} \cdot 5\text{H}_2\text{O} \cdot \text{H}_2\text{O}^{**}$).
- 3) Five water molecules are in the first solvation shell around the UO_2^{2+} ion and one water molecule bonds to the first shell water molecule by hydrogen bonding ($\text{UO}_2^{2+} \cdot 5\text{H}_2\text{O} \cdot \text{H}_2\text{O}^*$).

Table 1 shows the Gibbs free energies and the binding energies of the different clusters in the aqueous system. The binding energy of $\text{UO}_2(\text{H}_2\text{O})_n^{2+}$ clusters in aqueous solution was determined as:

$$\Delta E_{\text{UO}_2^{2+} \cdot n\text{H}_2\text{O}} = E_{\text{UO}_2^{2+} \cdot n\text{H}_2\text{O}} - (E_{\text{UO}_2^{2+}} + nE_{\text{H}_2\text{O}})$$

where $E_{\text{UO}_2^{2+}}$ is the energy of the UO_2^{2+} ion and $E_{\text{H}_2\text{O}}$ is the energy of the water molecule, which were calculated using the same basis sets. All energies are the Gibbs free energy after adjustment for the concentration in the liquid ($p = 1\ 354$ atm) and include the PCM solvation energy. It argues that among the structures of $\text{UO}_2^{2+} \cdot 5\text{H}_2\text{O}$, $\text{UO}_2^{2+} \cdot 4\text{H}_2\text{O} \cdot \text{H}_2\text{O}^{**}$ and $\text{UO}_2^{2+} \cdot 4\text{H}_2\text{O} \cdot \text{H}_2\text{O}^*$, the structure of $\text{UO}_2^{2+} \cdot 5\text{H}_2\text{O}$ has the lowest binding energy. Its binding energy in liquid phase is 11.7 kcal/mol lower than $\text{UO}_2^{2+} \cdot 4\text{H}_2\text{O} \cdot \text{H}_2\text{O}^{**}$ and 3.4 kcal/mol lower than $\text{UO}_2^{2+} \cdot 4\text{H}_2\text{O} \cdot \text{H}_2\text{O}^*$. It indicates that among these three structures, the structure with five water molecules in the first solvation shell is more stable than that with four water molecules in the first co-ordination shell. On the other hand, among the structures

of $\text{UO}_2^{2+} \cdot 6\text{H}_2\text{O}$, $\text{UO}_2^{2+} \cdot 5\text{H}_2\text{O} \cdot \text{H}_2\text{O}^{**}$ and $\text{UO}_2^{2+} \cdot 5\text{H}_2\text{O} \cdot \text{H}_2\text{O}^*$, the structure of $\text{UO}_2^{2+} \cdot 5\text{H}_2\text{O} \cdot \text{H}_2\text{O}^*$ has the lowest binding energy; in liquid phase the binding energy is 7.5 kcal/mol and 21.5 kcal/mol lower than $\text{UO}_2^{2+} \cdot 5\text{H}_2\text{O} \cdot \text{H}_2\text{O}^{**}$ and $\text{UO}_2^{2+} \cdot 6\text{H}_2\text{O}$ respectively. The structure of $\text{UO}_2^{2+} \cdot 5\text{H}_2\text{O} \cdot \text{H}_2\text{O}^{**}$ is the lowest in energy. It illustrates that the structure with five water molecules in the first solvation shell is more stable than that with six water molecules in the first solvation shell. In addition, the structure where the second shell water molecule connects to the first shell water molecule by hydrogen bonding is more stable than that of the second shell water molecule which directly bonds to the UO_2^{2+} ion. This demonstrates that five water molecules in the first shell can form the most stable complex with UO_2^{2+} , the co-ordination number of water molecules around the UO_2^{2+} ion in the first solvation shell being 5.

There is one point that must be emphasised here. All the above-mentioned binding energies are those in liquid phase. From Table 1 it is clear that the binding energies of $\text{UO}_2(\text{H}_2\text{O})_n^{2+}$ based on “gas phase calculation” are overestimated, and that the hydration number 4 is designated the most stable. That means that the solvation energy and the entropic contribution to the free energy account for a large portion. Since pentavalent uranyl ion has large solvation energy, a small change in the ion cavity might result in significant change in solvation energy. If the hydration energy and entropy effect are not included into the energy, results for the binding energy will be wrong, and thus the co-ordination number will also be wrong.

Dimeric uranyl hydroxide complex $(\text{UO}_2)_2(\text{OH})_2^{2+}$

Solid-state structures of the uranyl hydroxide dimer indicate that two uranyl groups are connected via a double OH bridge for the uranyl dinuclear complex, $(\text{UO}_2)_2(\text{OH})_2^{2+}$. The initial structure of our calculation is thus based on this principle (Figure 2). At several levels of theory, we have optimised the structure of $(\text{UO}_2)_2(\text{OH})_2(\text{H}_2\text{O})_6^{2+}$. Generally, the choice of the basis set is very important for reliable calculations. Computation time, however, is proportional to some power of the number of the basis functions. Therefore, it is always very important to find a compromise between the accuracy and the computation time. Schreckenbach, *et al.* [4] argues that the use of the 6-31+G* basis set is a reasonable choice for the calculation of the uranyl hydroxide monomer. We had obtained a different finding during the calculations of the uranyl hydroxide dimer. By adding a set of diffuse functions to the oxygen basis (6-31G* \rightarrow 6-31+G* \rightarrow 6-31++G*), we observed a small change in the uranyl axial bond, but considerable lengthening of the U-O_{OH} bond by up to 0.04 Å. The effect on the U-U bond length is also significant. The U-U bond length increased from 4.06 Å to 4.09 Å (6-31G* \rightarrow 6-31+G*), and then decreased to 4.04 Å (6-31++G*). The addition of a polarisation function to the hydrogen (using 6-31++G**) had only a small influence on the result, leading to a contraction of U-O_{ax} bond lengths by 0.006 Å, and a lengthening of the U-O_{OH} bonds by 0.02 Å. Thus, we consider that the calculation of uranyl hydroxide complex should be carried out at least at the 6-31++G* level of theory.

Our calculation suggested a “bent” O=U=O structure for the uranyl dimer, having an O=U=O angle of 169-171 degrees. The *ab initio* ECP calculation at the Hartree Fock level by Wadt [12] gave the correct *cis* bent and *trans* linear structures for ThO_2 and UO_2^{2+} , respectively. ThO_2 ($6d^05f^0$) is *cis*, bent (122 degrees) because it allows π -donation from the two oxygens to two independent 6d orbitals, with a single 6d orbital shared. UO_2^{2+} ($6d^05f^0$) is *trans*, linear because of the participation of its 5f orbitals. This calculation, however, does not exclude the possibility that the UO_2^{2+} ion may show deviations from the 180° angle. Theoretical calculations of the bare UO_2^{2+} ion at the BP86 and the MP4(SDQ) levels by Ismail, *et al.* [13] gave bent uranyl ion, the bending of 2° and 98°, respectively.

A significant bending of the uranyl at MP4(SDQ) level of theory indicates failure of the perturbation theory. It was concluded that the multi-configurational aspect of the wave function invalidates the MP2 and MP4 approaches. On the other hand, the B3LYP method gave reliable results.

There is a general agreement that the uranium 6d orbitals are involved in π bonding in the O=U=O moiety. Clark, *et al.* [14] argue that the OH⁻ ligand is a strong π donor in uranyl hydroxide, which results in the competition of the 6d e_g orbitals between oxo and hydroxo ligands. In fact, Dai, *et al.* [15] reported a red shift of the U(VI) charge transfer (CT) band (~410 nm) upon dimeric complexation. It indicates an electron transfer to the uranyl moiety from the equatorial plane. Having two π -donating oxygens in the equatorial “*ortho*” positions, (UO₂)₂(OH)₂(H₂O)₆²⁺ would have a significant asymmetry in the π orbital structure around the uranyl moiety, which probably favours the bending of the O=U=O against the OH⁻ ligand. A Raman spectroscopic study by Fujii, *et al.* [16] indicated that the polarisability of the U-Oax bond in (UO₂)₂(OH)₂²⁺ is 10-50% higher than that of UO₂²⁺, suggesting a “bent” (UO₂)₂(OH)₂²⁺.

The present study has shown that the uranyl hydroxide dimeric complex has a “bent” O=U=O angle. It is thus not appropriate to constrict to linear O=An=O angle during the quantum chemical calculations of actinyl complexes. It is not surprising that other ligands might contribute to the formation of more bent O=U=O. Studying the O=An=O angle may provide further insight into the axial and equatorial bondings of the actinyl complexes.

Uranyl carbonate complex

The structure optimisation of UO₂(H₂O)₅²⁺ and UO₂(CO₃)₃⁴⁻ complexes were carried out using 6-31G*, 6-31++G, and 6-31++G* basis sets for H,C and O. The calculated U-Oax and U-Oeq bond lengths are given in Table 2 along with EXAFS measurement data. The EXAFS data show that U-Oax bond length of uranyl hydrate and uranyl tricarbonate does not greatly deviate. The calculated U-Oax for UO₂(H₂O)₅²⁺ and UO₂(CO₃)₃⁴⁻ is, however, as different as ~0.08 Å. Obviously, the theoretical calculation seriously overestimates the U-Oax bond length of the UO₂(CO₃)₃⁴⁻ complex.

The carbonate ion, CO₃²⁻, has a resonance structure, and the carbon atom in the centre is connected with three equivalent oxygen atoms. Each oxygen atom has an effective charge of -2/3. We have carried out the optimisation calculation of the carbonate ion CO₃²⁻ at 6-31G, 6-31G*, 6-31G**, 6-31++G and 6-31++G* level of theories. At all levels of theory, we obtained only positive vibrational frequency. If the diffuse function is not added in the basis function, the effective charge of oxygen is too negative (-0.80 at the 6-31G level, -0.81 at the 6-31G* and 6-31G** levels). But the addition of diffuse function gave the oxygen effective charge close to -2/3 (-0.68 at the 6-31++G level, -0.63 at the 6-31++G* level). Thus, the diffuse function is mandatory in the calculation of the carbonate ion and carbonate complexes.

In the calculation of uranyl tricarbonate, however, we did not observe a significant impact of the addition of the diffuse function into the basis functions. It slightly changed the U-Oax bond length (~0.01 Å) but had more impact on U-Oeq bond length (~0.04 Å). This is probably because the interaction between the uranyl and the ligand is mainly electrostatic, and changes of equatorial ligand have no apparent influence on the axial bonding. It thus seems curious that the carbonate complexation significantly lengthened the U-Oax bond distance compared to the hydrate.

We have further studied this point by looking into HOMO and LUMO energies and their major orbital characters of the uranyl tricarbonate complex. According to Schreckenbach [4] and Hirata [17], the equatorial oxygen p orbitals are the main contributors of the HOMO and the nearly lying occupied MOs in uranyl hydrate, hydroxide and uranyl nitrate complexes. The LUMO and the near lying unoccupied MOs mainly consist of U 5f AOs. These facts suggest that uranyl hydrate and its complex have similar orbital character for the HOMO and LUMO and the near lying MOs. However, at the 6-31++G* level, orbitals near HOMO and LUMO of uranyl tricarbonate consist of an admixture of various AOs, suggesting the failure of the calculation. It is often pointed out that the calculation of highly negatively charged ion tends to fail.

We have carried out the structure optimisation of Liebigite, $\text{Ca}_2\text{UO}_2(\text{CO}_3)_3^0$. Because two calcium atoms cancel the negative charge of the carbonate ligand, the calculation for Liebigite does not have the problem with the charge. The calculated structure at the 6-31++G level of theory is given in Table 3. By adding two calcium atoms, the two U-Oax bond distances shortened by 0.05 Å compared to $\text{UO}_2(\text{CO}_3)_3^{4-}$. But the EXAFS measurements give 1.80 Å for the $\text{UO}_2(\text{CO}_3)_3^{4-}$ and 1.81 Å for $\text{Ca}_2\text{UO}_2(\text{CO}_3)_3^0$, suggesting that the U-Oax bond length is almost equal in these two species. Thus, we consider that the presence of the positively charged atom has solved the problem with the negative charge of the carbonate complex. In fact, the calculated structure of Liebigite does not deviate too much from the structure obtained by experiments. The addition of 10 hydration waters ($\text{Ca}_2\text{UO}_2(\text{CO}_3)_3 \cdot 10\text{H}_2\text{O}$, Figure 3) engendered a more reasonable accord with the experiment (Table 3).

In conclusion, we can say that the calculation of the uranyl tricarbonate tends to fail because it is a highly negatively charged ion, and the electrons do not fill the right orbitals. The addition of a cation to the system will solve the problem with the charge, and the calculated structure agrees reasonably with the experiments. Because the distal oxygen in uranyl tricarbonate has a high negative effective charge, it is probably mandatory to include polarisation, charge transfer and hydrogen bonding between the distal oxygen and the waters in the second co-ordination shell. Further studies including the second co-ordination shell seem worthwhile.

Acknowledgement

S. Tsushima was supported by a contract with Forschungszentrum Rossendorf (FZR) as a Guest Scientist at the Rossendorf Beamline at the European Synchrotron Radiation Facility (ESRF). The authors greatly appreciated the use of the SGI supercomputer ORIGIN 2000 at Technische Universität Dresden. We are grateful to Dr. Manfred Kunicke, FZR, for his technical support during the calculations and graduate student Tianxiao Yang, The University of Tokyo, for her assistance during the work.

REFERENCES

- [1] M.J. Frisch, *et al.*, Gaussian 98 User's Reference (2nd ed.), Gaussian, Inc., Pittsburgh, PA, (1998).
- [2] A.D. Becke, *J. Chem. Phys.* 98, 5648 (1993).
- [3] C. Lee, W. Yang, R.G. Parr, *Phys. Rev. B*, 37, 785 (1988).
- [4] G. Schreckenbach, P.J. Hay, R.L. Martin, *Inorg. Chem.*, 37, 4442 (1998).
- [5] G. Schreckenbach, P.J. Hay, R.L. Martin, *J. Comput. Chem.*, 20, 70 (1999).
- [6] P.C. Hariharan and J.A. Pople, *Theor. Chim. Acta*, 28, 213 (1973).
- [7] W.J. Hehre, R. Ditchfield and J.A. Pople, *J. Chem. Phys.*, 56, 2257 (1972).
- [8] S. Miertus, E. Scrocco and J. Tomasi, *Chem. Phys.*, 55, 117 (1981).
- [9] R. Martin, P. Jeffrey Hay and L.R. Part, *J. Phys. Chem. A*, 102, 3565 (1998).
- [10] S. Tsushima, A. Suzuki, *J. Mol. Struct. (THEOCHEM)*, 529, 21 (2000).
- [11] S. Spencer, L. Gagliardi, N.C. Handy, A.G. Ioannou, C.K. Skylaris, A. Willetts, A.M. Simper, *J. Phys. Chem. A*, 103, 1831 (1999).
- [12] W.R. Wadt, *J. Am. Chem. Soc.*, 103, 6053 (1981).
- [13] N. Ismail, J-L. Heully, T. Saue, J-P. Daudey, C.J. Marsden, *Chem. Phys. Lett.*, 300, 296 (1999).
- [14] D.L. Clark, S.D. Conradson, R.J. Donohoe, D.W. Keogh, D.E. Morris, P.D. Palmer, R.D. Rogers, C.D. Tait, *Inorg. Chem.*, 38, 1456 (1999).
- [15] S. Dai, M.C. Burleigh, J.M. Simonson, R.E. Mesmer, Z.L. Xue, *Radiochim. Acta*, 81, 195 (1998).
- [16] T. Fujii, K. Fujiwara, H. Yamana, H. Moriyama, *J. Alloys Compds.*, in press.
- [17] M. Hirata, R. Sekine, J. Onoe, H. Nakamatsu, T. Mukoyama, K. Takeuchi, S. Tachimori, *J. Alloys Compds.*, 128, 271-273, (1998).

Table 1. The binding energy of $\text{UO}_2^{2+}(\text{H}_2\text{O})_n$ clusters (kcal/mol)

Complex	Gas phase 0 K, 0 atm	Aqueous phase 298 K, 1 atm
$\text{UO}_2^{2+}\cdot 5\text{H}_2\text{O}$	-353.1	-58.3
$\text{UO}_2^{2+}\cdot 4\text{H}_2\text{O}\cdot \text{H}_2\text{O}^*$	-341.5	-46.6
$\text{UO}_2^{2+}\cdot 4\text{H}_2\text{O}\cdot \text{H}_2\text{O}^{**}$	-353.5	-54.9
$\text{UO}_2^{2+}\cdot 6\text{H}_2\text{O}$	-349.9	-34.8
$\text{UO}_2^{2+}\cdot 5\text{H}_2\text{O}\cdot \text{H}_2\text{O}^*$	-364.5	-48.9
$\text{UO}_2^{2+}\cdot 5\text{H}_2\text{O}\cdot \text{H}_2\text{O}^{**}$	-374.1	-56.3

* Second shell water bounds to uranium.

** Second shell water is hydrogen bonded to first shell.

Table 2. The structures of $\text{UO}_2(\text{H}_2\text{O})_5^{2+}$ and $\text{UO}_2(\text{CO}_3)_3^{4-}$ obtained by theoretical calculations and EXAFS measurements (length in Å)

Complex	Method	U-Oax	U-Oeq
$\text{UO}_2(\text{H}_2\text{O})_5^{2+}$	B3LYP/6-31G*	1.757	2.512
	B3LYP/6-31++G	1.776	2.502
	B3LYP/6-31++G*	1.751	2.532
	EXAFS	1.77	2.42
$\text{UO}_2(\text{CO}_3)_3^{4-}$	B3LYP/6-31G*	1.838	2.564
	B3LYP/6-31++G	1.844	2.604
	B3LYP/6-31++G*	1.824	2.592
	EXAFS	1.80	2.43

Table 3. The structures of Liebigite obtained by EXAFS and by theoretical calculations (length in Å)

Method	Complex	U-Oax	U-Oeq	U-C	U-Ca	U-Dis
EXAFS	Liebigite	1.81	2.44	2.90	3.94	4.22
Calculation	$\text{Ca}_2\text{UO}_2(\text{CO}_3)_3^0$		2.36	2.97	3.83	
			2.55	2.97		
			2.84	3.37		
Calculation	$\text{Ca}_2\text{UO}_2(\text{CO}_3)_3^0\cdot 10\text{H}_2\text{O}$		2.40	2.96	3.99	4.13
			2.60	2.96		
			2.72	3.25		

Figure 1. Optimised structures of $\text{UO}_2^{2+}(\text{H}_2\text{O})_3^{2+}$

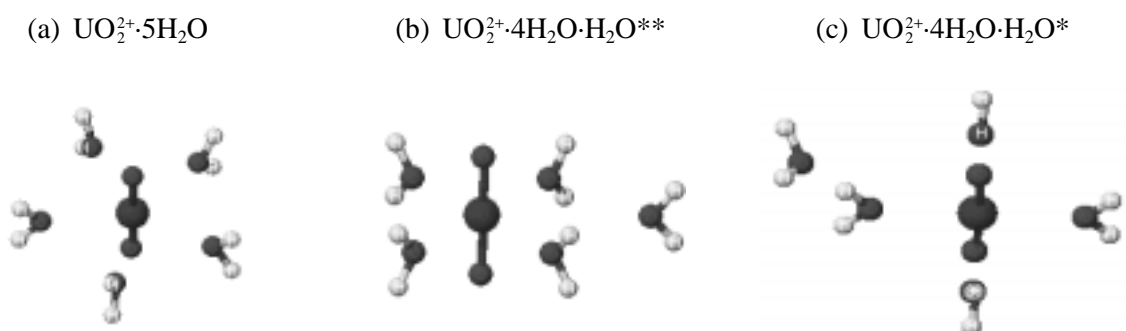


Figure 2. The structure of the dimeric uranyl hydroxide complex $(\text{UO}_2)_2(\text{OH})_2^{2+}$

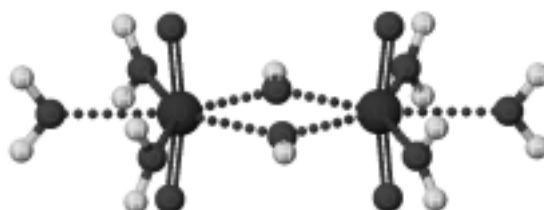


Figure 3. The structure of $\text{Ca}_2\text{UO}_2(\text{CO}_3)_3 \cdot 10\text{H}_2\text{O}$



ACTINIDES IN EARTH MATERIALS: THE IMPORTANCE OF NATURAL ANALOGUES

François Farges,^{1,2} Messaoud Harfouche,¹ Pierre-Emmanuel Petit³ and Gordon E. Brown, Jr.^{2,4}

¹Laboratoire des Géomatériaux, Université de Marne-la-Vallée

F-77454 Marne-la-Vallée Cedex 2 (France)

²Surface & Aqueous Geochemistry Group

Department of Geological & Environmental Sciences

Stanford University, Stanford, CA 94305-2115, USA

³European Synchrotron Radiation Facility

F-38041 Grenoble Cedex

⁴Stanford Synchrotron Radiation Laboratory

2575 Sand Hill Road, MS 99

Menlo Park, CA 94025, USA

Abstract

Predictions of the stability of waste forms designed for long-term storage of actinides require an accurate knowledge of the long-term properties of these actinides in their host matrix. One useful approach to address this issue involves comparison of structural and thermodynamic information derived from short time-scale experiments on synthetic samples with similar information from natural samples, including natural glasses and metamict minerals. These natural analogues of synthetic waste forms, although significantly different in structure, properties and composition from the synthetic samples, offer a number of examples of earth materials that have received large doses of radioactivity (mainly α events) over very long time periods (10^6 - 10^9 years). In this paper, we present a review of the co-ordination chemistry of actinides in natural deep-seated earth systems and their analogues (mostly glasses, melts and radiation-damaged minerals). Special emphasis is given to data analysis methods that are important in determining accurate XAFS-derived interatomic distances and co-ordination numbers for actinides in these complex materials, including anharmonicity, multi-electronic transitions, deconvolution procedures, and *ab initio* calculations of near-edge structure. The effects of anharmonicity and multi-electronic transitions are best studied using high-energy resolution spectrometers on third-generation synchrotron sources. Application of these methods to selected natural minerals (crystalline and radiation-damaged) is presented, together with a comprehensive list of unusual mineral structures that are known to incorporate relatively large amounts of actinides over long periods of geologic time in a stable manner.

Introduction

In earth materials such as primary minerals, melts, hydrothermal assemblages, surficial fluids and minerals as well as soils, natural actinides (Th and U) are relatively scarce. Their normalised natural abundances in the earth's crust are relatively low (6 and 1.8 ppm for Th and U, respectively, in crustal rocks) but are higher than those of silver or mercury [1,2]. However, natural actinides are thought to be more concentrated within the deep earth, and are believed to be a significant source of the earth's internal heat because of their nuclear reactions [3].

Despite this low abundance, natural actinides are among the most important ions in geochemistry. This is because of their radioactive decay (^{232}Th , ^{235}U and ^{238}U decay into ^{208}Pb , ^{207}Pb and ^{206}Pb , respectively [4]) which provides a means of dating geological processes [5]. It is also because of their unusual geochemical properties. For instance, Th and U are "incompatible" in melts, which means that they prefer to concentrate in the melt phase during the crystallisation of magmas [6]. Also, the presence of several oxidation states of uranium [U(IV), U(V) and U(VI)] makes this element behave quite differently as a function of oxygen fugacity. For example, uranium is relatively less soluble in melts and aqueous fluids when tetravalent, but it is generally highly soluble when hexavalent.

Because of the importance of U for understanding the earth's internal processes, as well as the packaging, reprocessing and environmental remediation of high-level nuclear waste, a knowledge of its oxidation states and co-ordination environments in earth materials is needed. Although it occurs only in the 4+ oxidation state in earth materials, a similar statement can be made about a knowledge of the co-ordination environment of Th in earth materials. For instance, this type of structural information can be used as an experimental validation of molecular dynamics modelling of actinide-bearing melts and solutions, as well as the extent of radiation damage in ceramics [7]. However, because of their relatively low concentrations in most earth materials, little structural information for actinides in such materials is available. In addition, few methods are sensitive to thorium, which is essentially spectroscopically inactive. X-ray absorption fine structure (XAFS) methods (at the M- and L-edges) are by far the most powerful tools available for obtaining speciation information for thorium at low concentrations. In contrast, uranium can be studied using a variety of spectroscopic methods such as UV-vis-NIR and laser-induced fluorescence spectroscopies and imaging. However, these methods are indirect and highly sensitive to the presence of other cations (especially 3d transition elements such as Fe, which are often present in earth materials).

The use of synchrotron sources can overcome these limitations by providing quantitative, element-specific information on oxidation states and co-ordination environments for elements like Th and U (even in chemically and structurally complex materials such as crystals, finely divided minerals, molten silicates, soils or aqueous solutions [8]). Also, third-generation synchrotron sources provide higher resolution spectra with higher signal-to-noise ratios. As a result, the understanding of structural sites occupied by actinides and their oxidation states in natural systems has benefited from significant recent developments in XAFS spectroscopy methods, which we describe in this paper.

Oxidation states of uranium in geological systems

Three oxidation states are known for uranium in earth materials: U(IV), U(V) and U(VI). No metallic uranium or U(III) has been found in geological systems or in moon rocks [1], because these redox states require extremely low oxygen fugacities. The relative amounts of these oxidation states depend on oxygen fugacity ($f\text{O}_2$), mineral or melt composition, and, in part, on other redox couples such as Fe(II)/Fe(III) or possibly Cr(III)/Cr(VI).

In deep-seated geologic (“igneous”) systems, U occurs as both U(IV) and U(V), although it is most often concentrated in U(IV)-bearing minerals such as uraninite/pitchblende UO_{2+x} (with $0 < x < 0.6$), coffinite $USiO_4$ or as inclusions of these phases in rock-forming minerals such as biotite. Tetravalent U also occurs as a minor component of accessory minerals including zircon, titanite, various (Ca, Th) oxides such as zirkelite/zirconolite, and other complex oxides of the euxenite-pyrochlore families for the most common ones (see Table 1). Tetravalent uranium is also probably the dominant oxidation state of U in the earth’s mantle minerals, although some direct characterisation of these phases would be required to verify this suggestion [9]. Under more oxidising conditions, Calas [10] found that U(V) is an important oxidation state of uranium in silicate melts. Farges, *et al.* [6] determined the dominant environment of U in synthetic glasses of geological interest – a distorted six-co-ordinated environment, having a XANES L_{III} -edge position similar to that for U(VI) compounds. U(V) is rarely found in minerals, occurring in minor amounts with the more common U(IV) in some radiation-damaged (“metamict”) zircons.

Under oxidising conditions, U(VI) is the stable oxidation state in which this element is most likely transported in hydrothermal (supercritical) and aqueous systems. Complexes with chlorine or carbonates [11] are suspected to transport uranium and thorium in such systems, but no direct evidence for such complexation has yet been reported. In silicate glasses and melts, U(VI) is usually found as uranyl-bearing moieties (with $U-O_{axial}$ near 1.77 Å and $U-O_{equatorial}$ near 2.25 and 2.5 Å [6]). Finally, highly damaged and weathered minerals such as zircon (“cyrtolite” variety: hydrated $ZrSiO_4$), thorite and pyrochlore show considerable amounts of U(VI). Preliminary work suggests that weathering, not radiation damage, is the cause of the tetravalent oxidation of uranium in these minerals [12].

Actinides and anharmonicity

XAFS studies of melts *in situ* (at high temperature) require an accurate understanding of the way Th-O and U-O bonds behave with increasing temperature. Such a study was conducted using the heating loop technique on a dispersive EXAFS spectrometer at LURE [13]. Several oxide and silicate compounds of Th and U were investigated between room temperature and 2 000 K [14]. Fourier transforms of the EXAFS spectra of Th in a sodium disilicate glass/melt as a function of temperature (20 to 1 474°C) are shown in Figure 1(a). The use of anharmonic theories are required to achieve accurate bond distances and co-ordination numbers from EXAFS data taken at high temperature [15]. Results of the modelling show that the anharmonic variations in the EXAFS spectra due to temperature cannot be properly modelled using cumulant expansions. In contrast, the use of an analytical function [16] resulted in excellent EXAFS-derived distances and co-ordination numbers [14]. Figure 1(b) shows the results of harmonic versus anharmonic modelling (using the analytical function of Winterer [16] for Th-O pair correlations in a Th-containing sodium disilicate melt/glass as a function of temperature. In the case of crystalline ThO_2 , the EXAFS-derived linear thermal expansion coefficient ($10(2) \times 10^{-6} K^{-1}$) is in excellent agreement with the experimental one ($9 \times 10^{-6} K^{-1}$) derived by X-ray diffraction studies. In the case of uranium, similar studies are in progress and already show that, in the case of uranyl-bearing compounds, the axial U-O bond vibrates much less with temperature than the longer equatorial U-O bonds. Therefore, at high temperature, it is often difficult to extract robust structural information from U-EXAFS spectra. However, theoretical studies of U L_{III} -XANES spectra provide a more robust way of obtaining accurate information on the co-ordination environment of U at high temperature.

XANES studies of actinides: theoretical calculations and deconvolution procedures

The newest versions of the FEFF code 8.2 [17,18] make possible relatively accurate calculations of the XANES spectral region for most elements. As outlined by Ankudinov, *et al.* [18], the use of a partially non-local potential, i.e. Dirac-Fock for core, Hedin-Lundqvist for valence electrons and a constant imaginary part (the “EXCHANGE 5” option) provides fairly good results, although some improvements are still required [19]. In the case of α -uranotile, in which uranium is present as the uranyl moiety [20], it is possible to reproduce relatively accurately the experimental XANES spectra [Figure 2(a)]. This theoretical simulation includes the contributions arising from axial and equatorial oxygens, in excellent agreement with polarised XANES experiments on other uranyl-bearing structures [21].

The introduction of core-hole deconvolution procedures (either instrumental, multi-excitation and/or core-hole lifetime-related [22-26] provides new insights about XANES theoretical calculations and EXAFS data reduction. For instance, L-edges of actinides have a relatively large core-hole lifetime (~ 10 eV) [27], making it necessary to perform such procedures cautiously (i.e. with a noise level below 10^{-4}). The results (see Figure 2(a) for an example of instrumental deconvolution) are promising, however, because of the availability of high-flux spectrometers, such as beam line ID26 (ESRF, Grenoble, France), together with low-noise Si photodiode detectors [28], which makes the study of dilute natural samples feasible. These new convolution procedures will be important for materials having several redox states of uranium or for tracing selected spectral features, such as those due to multiple-scattering and partially hidden pre-edges. In addition, the excellent signal-to-noise ratio achieved on third-generation synchrotron sources as compared to older sources reveals the presence of multi-excitation transitions that were not detectable on first-generation sources (compare Figure 2(b) with [29]). In Th-bearing radiation-damaged natural zircons, for example, a probable multi-electronic feature is likely to occur in any L_{III} EXAFS spectrum of Th, near $k = 10 \text{ \AA}^{-1}$. In this case core-hole lifetime deconvolution procedures are required to detect these features. In these samples, another suspicious feature was found near $k = 5.5 \text{ \AA}^{-1}$, but its multi-electronic excitation origin is not clear as the feature is part of a wide EXAFS oscillation arising from Th-O pairs. If these contributions were ignored, it is likely that the medium-range structure ($\leq 6 \text{ \AA}$) around Th in any sample would be misinterpreted, as these features interfere with the high-frequency EXAFS signals arising from next-nearest neighbours. A similar type of analysis must be performed for the L_{III} -edge XANES and EXAFS spectra of U as well as for artificial actinides.

Actinides in silicate glasses and melts

XAFS studies of thorium and uranium in glass/melt systems of geochemical interest [6,29,30] suggest that only uranyl-bearing moieties form “complexes” in glasses and melts. Tetravalent actinides were found to adopt a different co-ordination environment in simple silicate glasses, including both six-co-ordinated environments and mixtures of six- and eight-co-ordinated environments [29]. More recent studies suggested that similar environments also exist in the melt to 1 450°C [31]. Therefore, the location of uranium and thorium in glasses gives a good approximation of the sites of these actinides in high temperature melts. No clear evidence for halogen complexation of U(IV), U(V) and U(VI) [6] or of Th [29] has been found, although such complexes are often invoked to help explain the transport properties of actinides in melts. In all U(VI)-containing glasses, there is a great deal of evidence from XANES and EXAFS spectroscopy as well as from optical absorption spectroscopy that U is present as uranyl groups with two short axial bonds [$d(\text{U-O}_{\text{axial}}) \approx 1.77\text{-}1.85 \text{ \AA}$] and four or five longer equatorial bonds to oxygen [$d(\text{U-O}_{\text{equatorial}}) \approx 2.18\text{-}2.25 \text{ \AA}$]. These results are consistent with the local structures of U(VI) in borosilicate glasses used in radioactive waste storage. All of these studies

demonstrate the stability of the uranyl group geometry in silicate, aluminosilicate and borosilicate glasses and melts of various compositions and different average structure. They also indicate that melt structure exerts little influence on the local environment around U(VI).

Bond valence models for actinides in oxide glasses and melts

Bond valence theory has been used to model the local structure around Th and U in silicate glasses [6,29] and melts [31]. These empirical models are based on the application of Pauling's second rule [32,33], see also Ref. [8] for a more detailed discussion of Pauling bond valence constraints on medium-range structure in silicate glasses and melts. The application of these empirical models is particularly useful for constraining the medium-range structure (out to 3-4 Å radial distance) around actinides in glasses and melts because of the lack of robust pair potentials for actinides required for accurate molecular dynamics modelling or for reverse Monte Carlo studies of neutron/X-ray scattering experiments.

The calculated models suggest that, because of their high charge and low co-ordination, tetravalent actinides are not likely to bond directly to a bridging oxygen (BO) in the glass network at the observed Th/U-O distances (2.3-2.4 Å range) without significantly lengthening of some individual Si-O bonds beyond their maximum observed value, and disrupting the tetrahedral network. A more plausible structural configuration corresponds to the linkage of Th/U(IV) to several non-bridging oxygens (NBOs). These oxygens are most likely around Th/U(IV) because they require one Si(IV) and one alkali to charge balance Th/U(IV). The presence of some NBOs around Th corresponds to an environment characteristic of a weak network modifier following the definition of Nelson, *et al.* [34].

The structural and chemical roles of the two types of oxygen ligands of uranyl groups can also be understood by considering the variation of U-O bond strength with bond length [35]. If we consider the EXAFS-derived U(VI)-O_{axial} distances, this relationship shows that the bond strengths of U(VI)-O_{axial} bonds range from 2.2 to 1.96 vu for the observed U(VI)-O_{axial} distances (1.77 to 1.85 Å). These bond strength values are very close to those required for "charge balance" at the axial oxygens in the Pauling sense (i.e. the sum of bond strengths to each oxygen is close to 2.0 vu [32]), suggesting that these oxygens are not bonded to other cations in the glasses studied. This idea provides a rationale for the common observation that uranyl axial oxygen ligands do not participate in other chemical bonds in crystalline uranyl-compounds. Thus these axial oxygens are not expected to interact with the glassy network. As a consequence, the U(VI)-O_{axial} distance is longer than 1.7 Å in all uranyl-containing compounds. The non-bonded character of the axial oxygens helps explain the stability of uranyl groups with low distortion in silicate melts. In contrast, the U(VI)-O_{equatorial} bonds have lower bond strengths (\approx 0.60-0.65 vu). Recent molecular dynamics calculations for glasses and melts [36] have suggested that most ions follows Pauling's second rule to an accuracy level of ± 2 -13%.

Actinides in minerals

Accessory minerals like zircon, titanite, apatite, pyrochlore and many others (Table 1) can be studied using XAFS methods to provide useful information about the location of trace/minor amounts of actinides. Recent results suggest that substitution of actinides for smaller ions in minerals often requires substantial expansion of the original local structure of their host mineral to accommodate their larger size [12]. This local expansion effect may extend as far as 4 Å and is close to that measured in the isostructural actinide-rich equivalent (e.g. ThSiO₄ for Th in ZrSiO₄). Therefore, such replacements are the cause of a number of Å-scale defects in the structure. Molecular dynamics calculations of U in crystalline zircon confirm these preliminary results [7].

Actinides in radiation-damaged crystals

In nature, one can find minerals that were exposed to intense radiation damage (over 10^{16} α /mg of sample). These samples, which may have only moderate actinide contents, suffered only low levels of α -decay damage but were exposed to this decay for millions of years and sometimes billions of years [4]. These minerals usually retain their crystallographic faces but their internal structure is destroyed by alpha recoil, produced by the decay of actinides (“metamict”). Table 1 lists the principal metamict minerals, which are mostly oxides and include some silicates. Among these metamict minerals, zircon is the most common. The periodic to aperiodic displacive phase transition of minerals due to α -particle recoil is of special interest in both mineralogy and in materials science. Radiation-induced defects in complex ceramics are an important consideration in evaluating the long-term behaviour of individual phases that may occur in proposed crystalline, high-level nuclear waste forms [37,38,39].

Using XAFS spectroscopy, it is possible to measure the oxidation state of uranium in natural metamict minerals that have suffered major radiation damage and to evaluate the effects of the relatively highly ionising decay of natural radioactivity. In the case of natural pyrochlores [40] and the thorite/thorogummite series [41], U was found to be oxidised, in contrast to zirconolite or zircon, which show no U oxidation [41,42]. This important conclusion, as well as other findings, enhances the choice of zirconolite and zircon as potential hosts for high-activity nuclear wastes (Pu and Am among others). However, the effect of long-term radiation damage in minerals is extremely variable. In zircon, bond valence models suggest the formation of Zr-rich domains (and concomitant Si-rich domains) in highly metamict zircons [43], which was confirmed recently using ^{29}Si NMR spectroscopy [44] and molecular dynamics calculations [7]. Such major structural reorganisation of the tetrahedral framework cannot occur in oxides, such as zirconolite.

Similar studies must be extended to Cr or Ce, which are structural analogues of Pu and Am, and can be oxidised. Additional studies are required to better understand the location of these actinides in such structures after they have received high radiation doses. These phases are known to auto-heal their defects and to be more resistant to weathering and structural reorganisation than minerals/structure types like zircon or pyrochlore.

Conclusions

Despite the limited number of studies involving actinides in deep-seated geological systems by XAFS methods, third-generation synchrotron sources and optimised computer tools (software and hardware) should dramatically improve the contributions of earth and environmental scientists to the already large database on actinides in natural materials and ceramic waste forms. More importantly, earth materials offer a diversity of structures and concepts that are interesting to investigate in order to determine if these natural analogues are suited for high-level waste containment and also to test computer methods with a combination of appropriate experimental methods such as X-ray absorption fine structure spectroscopy.

Acknowledgements

We thank the organising committee for the invitation to present this paper at the Actinide-XAS-2000 Workshop in Grenoble, France. We also wish to thank Dr. David K. Shuh (Chemical Sciences Division, Lawrence Berkeley National Laboratory) and an anonymous reviewer for a careful review of the manuscript. Our work discussed in this review was supported by the French GDR *Nomade*, the Institut Universitaire de France, the US Department of Energy (DOE) and the National Science Foundation (NSF). Our synchrotron radiation studies were carried out at the Stanford Synchrotron Radiation Laboratory (SSRL) and the European Synchrotron Radiation Facility (Grenoble, France). SSRL is supported by the US DOE and the National Institutes of Health. The technical staffs of these synchrotron laboratories are thanked for their help during our XAFS studies, particularly due to A. Solè and J. Goulon (ESRF), as well as J.R. Bargar (SSRL). Fruitful discussions with R.C. Ewing (University of Michigan, Ann Arbor) and sample donations from three national mineral collections in Paris (Muséum National d'Histoire Naturelle, École Nationale Supérieure des Mines and the Sorbonne collection at Université de Paris 6^{ème}) are also gratefully acknowledged.

REFERENCES

- [1] F. Bea, in *Encyclopedia of Geochemistry*, C.P. Marshall and R.W. Fairbridge, eds., pp. 645-648, Kluwer Academic Publishers (Dordrecht, The Netherlands, 1999).
- [2] S. Krishnaswami, in *Encyclopedia of Geochemistry*, C.P. Marshall and R.W. Fairbridge, eds., pp. 630-635, Kluwer Academic Publishers (Dordrecht, The Netherlands, 1999).
- [3] J.L. Vigneresse and M. Cuney, in *Terrestrial Heat Flow and the Lithosphere Structure*, V. Cermak and L. Rybach, eds., pp. 86-110 (Springer-Verlag, New York, 1991).
- [4] R.C. Ewing, in *Uranium: Mineralogy, Geochemistry and the Environment*, P.C. Burns and R. Finch, eds., *Reviews in Mineralogy and Geochemistry*, Vol. 38, Mineralogical Society of America, Washington, D.C. (1999).
- [5] G. Faure, *Principles of Isotope Geology*, 2nd edition, New York, John Wiley & Sons. 589 pp. (1986).
- [6] F. Farges, C.W. Ponader, G. Calas and G.E. Brown, Jr., *Geochim. Cosmochim. Acta*, 56, 4205-4220 (1992).
- [7] J-P. Crocombette and D. Ghaleb, *J. Nuclear Mat.*, 257, 282-286 (1998).
- [8] G.E. Brown, Jr., J.R. Bargar, F. Farges and H.T. Berbeco, these proceedings (2001).
- [9] E. Knittle, *Geodynamics Series*, 28, 119-130, American Geophysical Union, Washington, D.C. (1998).
- [10] G. Calas, *Geochim. Cosmochim. Acta*, 43, 1521-1531 (1979) (in French).

- [11] H. Keppler and P.J. Wyllie, *Nature*, 348, 531-533 (1990).
- [12] M. Harfouche, F. Farges and P-E. Petit, "Structural Characterization of Natural Actinides (Th and U) in Ceramics and Analogues: XANES and EXAFS Studies on Natural Zircons", European Union of Geosciences (EUG XI), J1-2671 (in press).
- [13] F. Farges, J-P. Itié, G. Fiquet and D. Andrault, *Nucl. Instrum. Meth. in Phys. Res. B*, 101, 493-498 (1995).
- [14] Z. Wu and F. Farges, *Physica B*, 266, 282-289 (1999).
- [15] G.E. Brown, Jr., F. Farges and G. Calas, in *Structure, Dynamics, and Properties of Silicate Melts*, J.F. Stebbins, D.B. Dingwell and P.F. McMillan, eds., pp. 317-410, *Reviews in Mineralogy*, Vol. 32, The Mineralogical Society of America, Washington, DC (1995).
- [16] M. Winterer, Proceedings of the 9th International Conference on X-ray Absorption Fine Structure (XAFS IX, Grenoble), *J. Phys IV France*, 7, 243 (1997).
- [17] J.J. Rehr, Z.I. Zabinsky and R.C. Albers, *Phys. Rev. Lett.*, 69, 3397-4000 (1992).
- [18] A.L. Ankudinov, B. Ravel, J.J. Rehr and S.D. Conradson, *Phys. Rev. B* 58, 7565-7576 (1998).
- [19] H.A. Thompson, G.E. Brown, Jr. and G.A. Parks, *Am. Mineral.*, 82, 483-496 (1997).
- [20] F.V. Stohl and D.K. Smith, *Am. Mineral.*, 66, 610-625 (1981).
- [21] D.H. Templeton and L.K. Templeton, *Acta Crystallogr.*, A38, 62-67 (1982).
- [22] P.W. Loeffen and R.F. Pettifer, *Phys. Rev. B (Condensed Matter)*, 54, 14877-80 (1996).
- [23] A. Filipponi, *J. Phys. B*, 33, 2835-2841 (2000).
- [24] K.V. Klementev, "Deconvolution Problems in X-ray Absorption Fine Structure", *submitted* (see <http://www.crosswinds.net/~klmn/viper.html>) (2001).
- [25] V. Gotte, J. Goulon, Ch. Goulon-Ginet, A. Rogalev, C.R. Natoli, K. Perié, J-M. Barbe and R. Guillard, *J. Phys. Chem. B*, 104, 1927-1938 (2000).
- [26] F. Farges, G.E. Brown, Jr., P-E. Petit and M. Munoz, *Geochim. Cosmochim. Acta* (in press).
- [27] F.C. Brown, in *Synchrotron Radiation Research*, H. Winick and S. Doniach, eds., pp. 61-100, (Plenum Press, New York, 1980).
- [28] C. Gauthier, V.A. Solé, R. Signorato, J. Goulon and E. Moguiline, *J. Synchrotron Rad.*, 6, 164-166 (1999).
- [29] F. Farges, *Geochim. Cosmochim. Acta*, 55, 3303-3319 (1991).
- [30] L.L. Davis, H. Li, D. Caulder and J. Crum, *Geol. Soc. Am., 1999 Annual Meeting, Abstracts with Programs*, 31, p. 134 (1999).
- [31] F. Farges and G.E. Brown, Jr., *J. Physique IV*, 7 (C2), 1009-1010 (1997).

- [32] L. Pauling, *J. Am. Chem. Soc.*, 51, 1010-1026 (1929).
- [33] I.D. Brown and D. Altermatt, *Acta Crystallogr., B* 41, 244-247 (1985).
- [34] C. Nelson, T. Furukawa and W.B. White, *Mat. Res. Soc. Bull.* 18, 959-966 (1983).
- [35] N.E. Brese and M. O'Keefe, *Acta Crystallogr. B*, 47, 192-197 (1991).
- [36] F. Farges, S. Rossano and J-M. Delaye, "EXAFS, Bond-valence and Molecular Dynamics: The Case of KTS2 Glass/Melt, 4th European Conference in Mineralogy and Spectroscopy (in press).
- [37] W. Lutze and R.C. Ewing, in *Radioactive Waste Forms for the Future*, W. Lutze and R.C. Ewing, eds., pp. 700-740 (Elsevier, Amsterdam, 1988).
- [38] W.J. Weber, *J. Mat. Res.*, 5, 2687 (1991).
- [39] R.C. Ewing, W.J. Weber and F.W. Clinard, Jr., *Prog. in Nuclear Energy*, 29, 63-127 (1995).
- [40] G.R. Lumpkin and R.C. Ewing, *Phys. Chem. Minerals*, 16, 2-20 (1988).
- [41] F. Farges and G. Calas, *Am. Mineral.*, 76, 60-73 (1991).
- [42] F. Farges, R.C. Ewing and G.E. Brown, Jr., *J. Mat. Res.*, 8, 1983-1995 (1993).
- [43] F. Farges, *Phys. Chem. Minerals*, 20, 504-514 (1994).
- [44] I. Farnan, *Phase Transitions*, 69, 47-60 (1999).

Table 1. Main metamict minerals in nature

(a) Oxides		(b) Oxides (cont'd)	
• Group of pyrochlore, zirkelite/zirconolite series		• Serie fergusonite-(Y)-formanite-(Y)	
Zirconolite	(Ca,Fe,REE,Zr,Th)(Zr,Nb,Ti,Ta,Fe)Ti ₂ O ₇	Fergusonite β-(Y)	YNbO ₄
Polymignite	(Ca,Fe,REE,Zr,Th)(Zr,Nb,Ti,Ta,Fe)Ti ₂ O ₇	Fergusonite β-(Ce)	(Ce,La,Nd)NbO ₄
Zirkelite	(Ca,Th,Ce)Zr(Ti,Nb) ₂ O ₇	Fergusonite β-(Nd)	(Nd,Ce)NbO ₄
• Group of crichtonite		Fergusonite-(Y)	YNbO ₄
Davidite-(Ce)	(Ce,La)(Y,U)(Ti,Fe) ₂₀ O ₃₈	Fergusonite-(Ce)	(Ce,Nd,La)NbO ₄ ·0.3(H ₂ O)
Davidite-(La)	(La,Ce,Ca)(Y,U)(Ti,Fe) ₂₀ O ₃₈	Fergusonite-(Nd)	(Nd,Ce)(Nb,Ti)O ₄
• Group of pyrochlore, betafite series, with Ti > (Nb,Ta)		Formanite-(Y)	YTaO ₄
Betafite	(Ca,Na,U) ₂ (Ti,Nb,Ta) ₂ O ₆ (OH)	• Series baddeleyite-uraninite	
Stibiobetafite	(Sb,Ca) ₂ (Ti,Nb,Ta) ₂ (O,OH) ₇	Tazheranite	CaTiZr ₂ O ₈
Yttrobetafite-(Y)	(Y,U,Ce) ₂ (Ti,Nb,Ta) ₂ O ₆ (OH)	Calzirtite	CaZr ₂ TiO ₉
Plumbobetafite	(Pb,U,Ca)(Ti,Nb) ₂ O ₆ (OH,F)	Cerianite-(Ce)	(Ce,Th)O ₂
• Group of pyrochlore, pyrochlore series, with Nb > Ti		• Non-classified oxides	
Pyrochlore	(Na,Ca) ₂ Nb ₂ O ₆ (OH,F)	Zirconolite-2M	CaZrTi ₂ O ₇
Calciobetafite	Ca ₂ (Ti,Nb) ₂ (O,OH) ₇	Zirconolite-3T	CaZrTi ₂ O ₇
Kalipyrochlore	(K,Sr) ₂ Nb ₂ O ₆ (O,OH)·n(H ₂ O)	IMA98.059	(Bi,U,Ca,Pb) _{1+x} (Nb,Ta) ₂ O ₆ (OH)·n(H ₂ O)
Strontipyrochlore	Sr ₂ Nb ₂ (O,OH) ₇	(c) Phosphates (weakly metamict)	
Bariopyrochlore	Ba ₂ Sr ₂ (Nb,Ti) ₂ (O,OH) ₇	• Xenotime-(Y)-Wakefieldite-(Ce) series	
Yttropyrochlore-(Y)	(Y,Na,Ca,U) ₂ (Nb,Ta,Ti) ₂ (O,OH) ₇	Xenotime-(Y)	YPO ₄
Ceripyrochlore-(Ce)	(Ce,Ca,Y) ₂ (Nb,Ta) ₂ O ₆ (OH,F)	• Group of monazite	
Plumbopyrochlore	(Pb,Y,U,Ca) ₂ Nb ₂ O ₆ (OH)	Monazite-(La)	(La,Ce,Nd)PO ₄
Uranopyrochlore	(U,Ca,Ca) ₂ (Nb,Ta) ₂ O ₆ (OH,F)	Monazite-(Ce)	(Ce,La,Nd,Th)PO ₄
• Group of pyrochlore, microcline series, with Ta > Nb		Monazite-(Nd)	(Nd,Ce,La,Pr,Sm,Gd)(P,Si)O ₄
Microcline	(Na,Ca) ₂ Ta ₂ O ₆ (O,OH,F)	Cheralite-(Ce)	(Ce,Ca,Th)(P,Si)O ₄
Stannomicrocline	(Sn,Fe)(Ta,Nb,Sn) ₂ (O,OH) ₇	Brabantite	CaTh(PO ₄) ₂
Stibiomicrocline	(Sb,Ca,Na) ₂ (Ta,Nb) ₂ (O,OH) ₇	• Group of rhabdophane	
Bariomicrocline	Ba ₂ (Ta,Nb) ₂ (O,OH) ₇	Rhabdophane-(Ce)	(Ce,La)PO ₄ ·(H ₂ O)
Plumbomicrocline	(Pb,Ca,U) ₂ Ta ₂ O ₆ (OH)	Rhabdophane-(La)	(La,Ce)PO ₄ ·(H ₂ O)
Natrobstantite	(Na,Cs)Bi(Ta,Nb,Sb) ₂ O ₁₂	Rhabdophane-(Nd)	(Nd,Ce,La)PO ₄ ·(H ₂ O)
Bismutomicrocline	(Bi,Ca)(Ta,Nb) ₂ O ₆ (OH)	Brockite	(Ca,Th,Ce)(PO ₄) ₂ ·(H ₂ O)
Uranmicrocline	(U,Ca) ₂ (Ta,Nb) ₂ O ₆ (OH)	Tristramite	(Ca,U,Fe)(PO ₄ ,SO ₄) ₂ ·2(H ₂ O)
• Columbite series		Grayite	(Th,Pb,Ca)PO ₄ ·(H ₂ O)
Magnocolumbite	(Mg,Fe,Mn)(Nb,Ta) ₂ O ₆	Ningyoite	(U,Ca,Ce) ₂ (PO ₄) ₂ ·1-2(H ₂ O)
Manganocolumbite	(Mn,Fe)(Nb,Ta) ₂ O ₆	(d) Silicates	
Ferrocolumbite	FeNb ₂ O ₆	• Nesosilicates	
Manganotantalite	MnTa ₂ O ₆	zircon	ZrSiO ₄
Ferrotantalite	FeTa ₂ O ₆	coffinite	USiO ₄ ·U(SiO ₄) _{1-x} (OH) _{4x}
• Polycrase-(Y)-loranskite series		thorite	ThSiO ₄
Polycrase-(Y)	(Y,Ca,Ce,U,Th)(Ti,Nb,Ta) ₂ O ₆	huttonite	ThSiO ₄
Uranopolycrase	(U,Y)(Ti,Nb,Ta) ₂ O ₆	thorogummite	Th(SiO ₄) _{1-x} (OH) _{4x}
Yttrocrasite-(Y)	(Y,Th,Ca,U)(Ti,Fe) ₂ (O,OH) ₆	hafnon	HfSiO ₄
Fersmite	(Ca,Ce,Na)(Nb,Ta,Ti) ₂ (O,OH,F) ₆	Umbozerite	Na ₃ Sr ₄ ThSi ₈ (O,OH) ₂₄
Euxenite-(Y)	(Y,Ca,Ce)(Nb,Ta,Ti) ₂ O ₆	• Nesosubsilicates	
Samarskite-(Y)	(Y,Fe,U)(Nb,Ta) ₂ O ₄	Titanite	CaTiSiO ₅
Ishikawaite	(U,Fe,Y,Ca)(Nb,Ta) ₂ O ₄ (?)	Gadolinite-(Y)	Y ₂ FeBe ₂ Si ₂ O ₁₀
Yttrocolumbite-(Y)	(Y,U,Fe)(Nb,Ta) ₂ O ₄	Gadolinite-(Ce)	(Ce,La,Nd,Y) ₂ FeBe ₂ Si ₂ O ₁₀
Yttrotantalite-(Y)	(Y,U,Fe)(Ta,Nb) ₂ O ₄	Melanocerite-(Ce)	(Ce,Th,Ca) ₃ (Si,B) ₃ O ₁₂ (OH,F)·n(H ₂ O)
Loranskite-(Y)	(Y,Ce,Ca)ZrTaO ₆ (?)	• Sorosilicates	
• Aeschnite series		Yttrialite-(Y)	(Y,Th) ₂ Si ₂ O ₇
Aeschnite-(Y)	(Y,Ca,Fe)(Ti,Nb) ₂ (O,OH) ₆	Ekanite	ThCa ₂ Si ₈ O ₂₀
Aeschnite-(Ce)	(Ce,Ca,Fe)(Ti,Nb) ₂ (O,OH) ₆	Iraqite-(La)	K(La,Ce,Th) ₃ (Ca,Na) ₄ (Si,Al) ₁₆ O ₄₀
Aeschnite-(Nd)	(Nd,Ce)(Ti,Nb) ₂ (O,OH) ₆	Tritomite-(Y)	(Y,Ca,La,Fe) ₃ (Si,B,Al) ₃ (O,OH,F) ₁₃
Vigezzite	(Ca,Ce)(Nb,Ta,Ti) ₂ O ₆	Tritomite-(Ce)	(Ce,La,Ca,Y,Th) ₃ (Si,B) ₃ (O,OH,F) ₁₃
Niobo-aeschnite-(Ce)	(Ce,Ca)(Nb,Ti) ₂ (O,OH) ₆	Karnasurtite-(Ce)	(Ce,La,Th)(Ti,Nb)(Al,Fe)(Si,P) ₂ O ₇ (OH) ₄ ·3(H ₂ O)
Niobo-aeschnite-(Nd)	(Nd,Ce)(Nb,Ti) ₂ (O,OH) ₆	Tranquillityite	Fe ₈ (Zr,Y) ₂ Ti ₂ Si ₂₄
Rynersonite	Ca(Ta,Nb) ₂ O ₆	Chevkinite-(Ce)	(Ce,La,Ca,Na,Th) ₄ (Fe,Mg) ₂ (Ti,Fe) ₃ Si ₄ O ₂₂
Tantaloeschnite-(Y)	(Y,Ce,Ca)(Ta,Ti,Nb) ₂ O ₆	Karnasurtite-(Ce)	(Ce,La,Th)(Ti,Nb)(Al,Fe)(Si,P) ₂ O ₇ (OH) ₄ ·3(H ₂ O)
• Thorutite-orthobrannerite series		Allanite-(Y)	(Y,Ce,Ca) ₂ (Al,Fe) ₂ (SiO ₄) ₃ (OH)
Thorutite	(Th,U,Ca)Ti ₂ (O,OH) ₆	Allanite-(La)	Ca(La,Ce)(Fe,Mn)(Al,Fe) ₂ (SiO ₄) ₃ (OH)
Brannerite	(U,Ca,Ce)(Ti,Fe) ₂ O ₆	Allanite-(Ce)	(Ce,Ca,Y) ₂ (Al,Fe) ₂ (SiO ₄) ₃ (OH)
Orthobrannerite	U ₂ Ti ₄ O ₁₂ (OH) ₂	Vesuvianite	Ca ₃ Mg ₂ Al ₂ (SiO ₄) ₂ (Si ₂ O ₇) ₂ (OH) ₂
• Petscheckite-liandratite series		Steenstrupine-(Ce)	Na ₁₄ Ce ₂ Mn ₂ Fe ₂ (Zr,Th)(Si ₆ O ₁₈) ₂ (PO ₄) ₇ ·3(H ₂ O)
Petscheckite	UFe(Nb,Ta)2O8	Thorosteenstrupine	(Ca,Th,Mn) ₂ Si ₄ O ₁₁ F ₆ (H ₂ O)
Liandratite	U(Nb,Ta)2O8		

Figure 1. Comparison of (a) Fourier transforms for Th in a sodium disilicate glass/melt as a function of temperature and (b) average Th-O distances calculated using both harmonic and anharmonic EXAFS models (modified after [14])

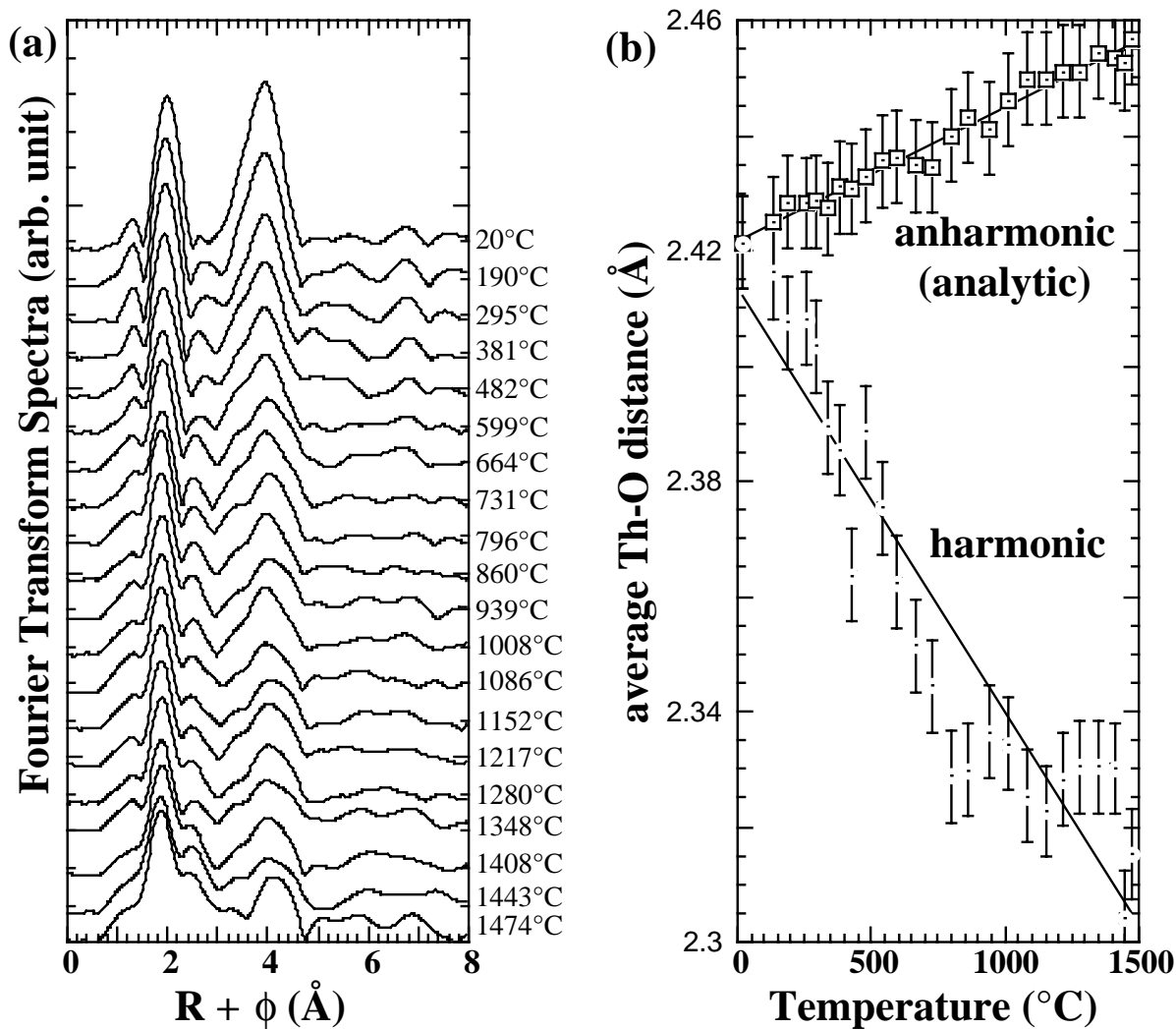
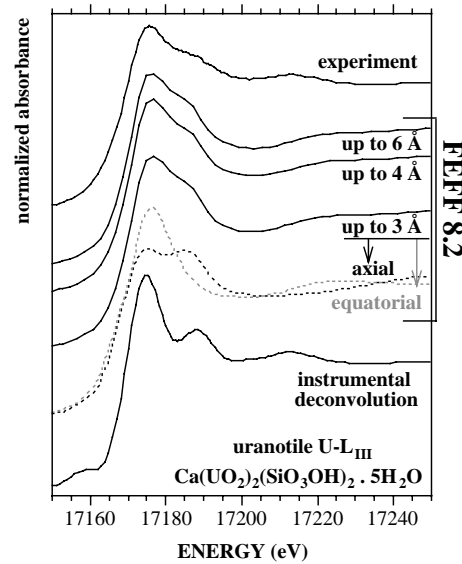
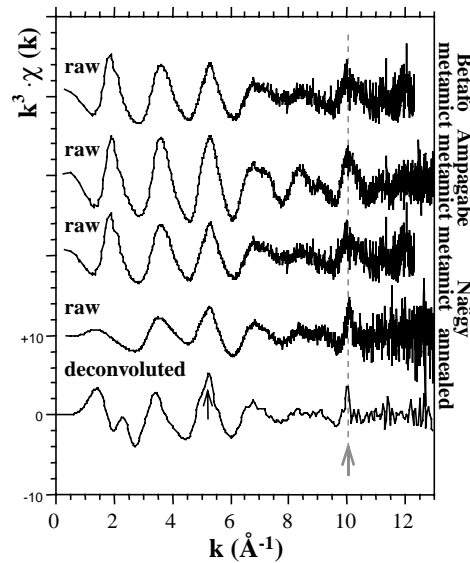


Figure 2

(a) Experimental (top curve) and calculated U- L_{III} XANES spectra (2nd, 3rd and 4th from top) using FEFF 8.2 for α -uranotile, considering different cluster sizes: uranyl moiety (up to 3 Å from the central U, also showing the individual axial and equatorial contributions) and its medium-range environment including next-nearest neighbours (up to 4, and 6 Å, respectively). The more distant atoms (Si, U, Ca, O and H) do not contribute significantly to the measured spectrum. The normalised experimental spectrum was collected on undulator beam line ID26 at ESRF, and its instrumental deconvolution (i.e. related to monochromator broadening: bottom curve) was calculated using the VIPER code [24]. The instrumentally deconvoluted spectrum is consistent with *ab initio* XANES calculations.



(b) normalised k^3 -weighted EXAFS spectra at the L_{III} -edge of Th (100-2 000 ppm Th) in various Th-bearing zircons from different localities in Madagascar (Betafo, Ampagabe) and Japan (Naëgy): radiation damaged (“metamict”: top four spectra) or annealed (at 1 200°C for four hours: bottom two spectra). Spectra were collected on undulator beam line ID26 at ESRF. The thick grey arrows indicate a probable multi-electronic excitation transition near $k = 10 \text{ \AA}^{-1}$, which is best detected using a multi-electronic excitation deconvolution procedure in the VIPER code [24]. Another possible multi-electronic excitation feature may occur near $k = 5.5 \text{ \AA}^{-1}$ (light black arrow). Neglecting these multi-electronic excitation features can lead to incorrect structural information in EXAFS data analysis, particularly for next-nearest neighbour contributions.



**LOCAL STRUCTURE OF Th COMPLEXES ON MONTMORILLONITE
CLAY MINERAL DETERMINED BY EXTENDED X-RAY
ABSORPTION FINE STRUCTURE (EXAFS) SPECTROSCOPY**

R. Dähn,¹ A.M. Scheidegger,¹ A. Manceau,² B. Baeyens¹ and M.H. Bradbury¹

¹Waste Management Laboratory, Paul Scherrer Institute
CH-5232 Villigen, Switzerland

²Environmental Geochemistry Group, LGIT-IRIGM, University of Grenoble
BP53, F-38041 Grenoble Cedex 9, France

Abstract

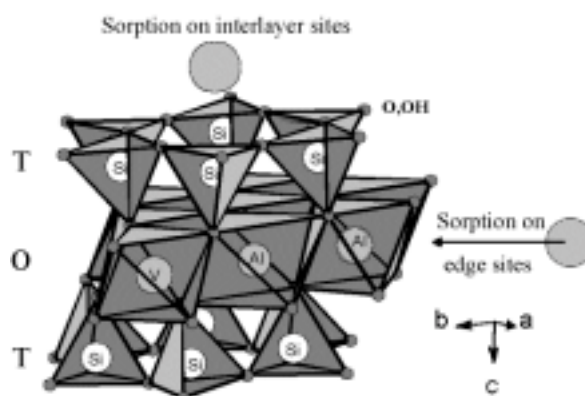
The research at the Waste Management Laboratory, PSI, concentrates on the understanding of safety relevant mechanisms and processes that govern the release of radionuclides from waste matrices, and their transport through engineered barrier systems and the surrounding geosphere. For this reason, detailed sorption studies of radionuclides in clay and cement systems are conducted. The studies are combined with extended X-ray absorption fine structure (EXAFS) spectroscopy measurements in order to understand the sorption mechanisms at an atomic level.

In this manuscript, a case study of Th(IV) uptake on montmorillonite is presented. EXAFS samples were prepared by incubating a montmorillonite suspension with Th for seven days at pH = 5 (Th_{initial}: 4.3×10^{-5} to 4×10^{-4} M). The resulting Th loadings on the clay varied between 14 and 166 $\mu\text{mol/g}$. L_{III}-Th EXAFS spectra of Th-treated montmorillonite were measured at the Rossendorf Beamline at the European Synchrotron Radiation Facility. Data analysis revealed the presence of two O shells at 2.27 Å and 2.45 Å in all samples. The spectra at low Th uptake suggest the presence of Si/Al and Th backscattering atoms at distances of 3.85 Å and 3.77 Å respectively. The presence of a Th-Si/Al backscattering pair suggests that Th is bound to Si tetrahedra by a double corner-sharing manner. At higher Th uptake, however, the spectrum shows a strong similarity with the spectrum of amorphous Th(OH)₄ and suggests that Th is predominately present as a newly formed Th(OH)₄-like phase.

Introduction

Sorption on mineral surfaces strongly affects the fate and mobility of contaminants in the geosphere. Therefore, an atomic-level understanding of sorption mechanisms of contaminants on mineral surface is of fundamental importance for maintaining environmental quality and assessing the long-term stability of waste repositories. On clay minerals several uptake mechanisms of divalent metal ions such as Ni(II), Co(II) and Zn(II) have been proposed: sorption on edge sites, sorption on interlayer sites (Figure 1) and the formation of lamellar nucleation phases such as neoformed layer silicates and mixed-layered double hydroxides [1-4].

Figure 1. Sorption modes on dioctahedral aluminous clays (V = vacancy) [5]



In this study EXAFS was used to investigate the uptake process of Th(IV) on montmorillonite. Th has long been recognised as an important tracer element in natural waters, soils and sediments because of its accurately known source terms, long half-life and single redox state [6]. Thorium is, therefore, a suitable analogue for other tetravalent actinides. Furthermore, Th is of major concern in nuclear waste management and an important contaminant in fly ashes from lignite power plants [7]. Th has been added to synthetic silicate glasses in order to study the structural environment of Th as a function of melt composition and polymerisation [8]. Long-term spontaneous radiation will make crystalline compounds (e.g. $ZrSiO_4$) become aperiodic and also oxide glasses to nucleate [9,10]. Dioctahedral aluminous clays are used as a backfill material in the Swiss concept for a high-level radioactive waste repository and, therefore, metal sorption on montmorillonite has been investigated in our laboratory in great detail [11].

Materials and methods

The montmorillonite STx-1 used in this study ($Si_4Al_{1.67}(Fe^{2+},Mg)_{0.33}O_{10}(OH)_2(Me_{0.33},H_2O)$, where Me refers to a metal cation in the interlayer space between sheets) was purchased from the Source Clay Minerals Repository Project of the Clay Minerals Society.

The EXAFS samples were prepared by adding 11-100 ml of a Th stock solution ($1 \cdot 10^{-3}$ M $(Th(NO_3)_4 \cdot 5H_2O)$, pH 3.0, 0.001 M HNO_3) to 50 ml of a conditioned and purified montmorillonite suspension (ionic strength of 0.1 M $(NaClO_4)$ to block cation exchange processes). The suspension was then filled with a 0.1 M $NaClO_4$ solution to 250 ml resulting in a solid to liquid ratio of 2.4 g/L and an initial Th concentration of $4.3 \cdot 10^{-5} - 4.0 \cdot 10^{-4}$ M. The pH was adjusted and kept constant (pH = 5) and the samples were shaken end-over-end. The preparations were performed in a glove box under N_2 atmosphere (CO_2 and $O_2 < 5$ ppm). The reaction conditions were within the solubility limit

of $\text{Th}(\text{OH})_4$ [12,13,14]. After seven days of reaction time the suspensions were centrifuged and the wet pastes were filled into Plexiglas holders. The supernatant solutions were analysed by ICP-MS in order to determine the Th uptake on the Th/montmorillonite sorption system. Th L_{III} -edge EXAFS spectra were recorded at the Rossendorf Beamline (ROBL) at the ESRF [15] using a Si(111) crystal monochromator and Pt-coated mirrors. All sorption samples were measured at RT in fluorescence mode using a four-element Ge solid-state detector.

Data reduction was carried out by using the WinXAS 97 1.3 software package [16]. Radial structure functions (RSFs) were obtained by Fourier transforming k^3 -weighted $\chi(k)$ functions between 2.9 to 10 \AA^{-1} using a Bessel window function with a smoothing parameter of 4. Amplitude and phase shift functions were calculated with FEFF 8.0 [17] using the structure of thorite (α - ThSiO_4) [18] as reference. Since the inner potential corrections (ΔE_0) in the Th sorption samples varied between 5.5-6.5 eV, the parameter was fixed to 6 eV in order to reduce the number of free-fit parameters. Furthermore, the amplitude reduction factor (S_0^2) was set to 1.0.

The theoretical Th-O, Th-Si and Th-Th phase and amplitude functions calculated with FEFF 8.0 were tested by fitting the EXAFS spectrum of a synthetic thorite compound provided by Farges [8]. The results gave an average co-ordination number and bond distance of 8.5 ± 1.7 O atoms at 2.39 \AA ($\sigma^2 = 0.005 \text{\AA}^2$), of 5.3 ± 1.1 Th atoms at 3.9 \AA ($\sigma^2 = 0.005 \text{\AA}^2$) and of 3.9 ± 0.8 Si atoms at 3.92 \AA ($\sigma^2 = 0.005 \text{\AA}^2$). The structural parameters for thorite as determined by X-ray diffraction (XRD) are four equatorial O at 2.36 \AA , four axial O at 2.47 \AA , four Si at 3.9 \AA and four Th at 3.9 \AA [18]. The differences between EXAFS and XRD structural data are within the uncertainty of EXAFS parameters, that is $\sim 20\%$ for co-ordination numbers and $\sim 0.02 \text{\AA}$ for interatomic distances.

Results

Figure 2 shows the background subtracted, normalised and k^3 -weighted EXAFS spectra of montmorillonite treated with Th (sorbed Th concentrations of 14, 40 and 166 $\mu\text{mol/g}$). The corresponding RSFs are shown in Figure 3. For the lowest Th concentration the first peak is split into two and the amplitude is reduced, and the second peak is shifted to higher distance with higher Th concentration.

Figure 2. k^3 -weighted Th L_{III} -edge EXAFS spectra for Th sorbed on montmorillonite (pH = 5)

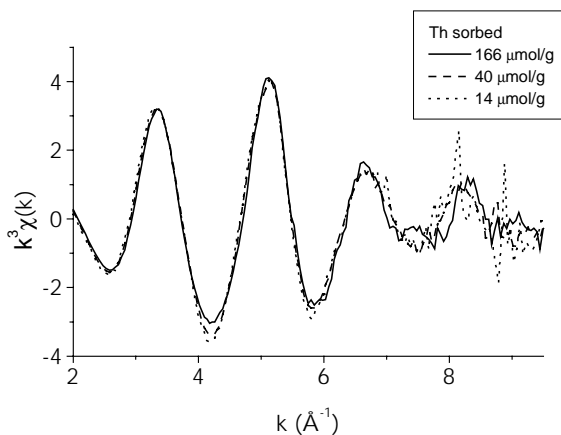
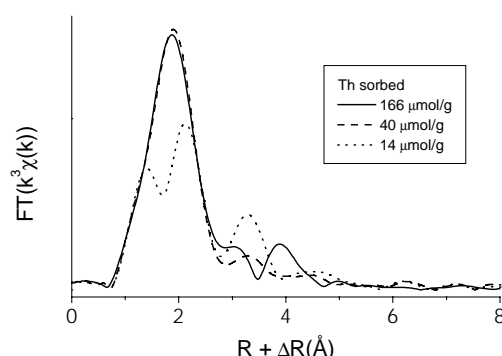


Figure 3. RSFs of k^3 -weighted Th L_{III} -edge EXAFS spectra for Th sorbed on montmorillonite (pH = 5)



The simulation of the Fourier filtered χ_0 functions obtained by back transforming first RSF peaks ($\Delta R = 1-2.5 \text{ \AA}$) indicated that two nearest O distances are present in all Th sorption samples. To constrain fit parameters, the Debye-Waller (DW) factor of the second oxygen shell was fixed to $\sigma^2 = 0.005 \text{ \AA}^2$, as in the thorite reference. Furthermore, the DW of the first oxygen shell was set to $\sigma^2 = 0.002 \text{ \AA}^2$ in order to obtain a total co-ordination number of 10 for the two O shells. For steric and crystallographic reasons the total number of oxygen atoms in the first and second shell should not exceed 10. EXAFS structural parameters for the two nearest O shells are listed in Table 1. The shorter shell consists of 2.6-3.0 O atoms at 2.27-2.28 \AA and the longer of 6.6-7.1 O atoms at 2.45-2.46 \AA .

Table 1. EXAFS structural parameters for two nearest O shells of Th sorbed on montmorillonite (pH = 5)

Sample	Th-O ¹			Th-O ²			ΔE_0^f [eV]	%Res
	N	R [\AA]	σ^{2f} [\AA^2]	N	R [\AA]	σ^{2f} [\AA^2]		
166 $\mu\text{mol/g}$	2.6	2.27	0.002	6.6	2.45	0.005	6	15.7
40 $\mu\text{mol/g}$	2.6	2.27	0.002	6.9	2.45	0.005	6	16.5
14 $\mu\text{mol/g}$	3.0	2.28	0.002	7.1	2.46	0.005	6	6.6

N, R, σ^2 , ΔE_0 are the co-ordination numbers, interatomic distances, Debye-Waller factors and inner potential corrections.

f: Fixed during the fit procedure.

The deviation between the fitted and the experimental spectra is given by the relative residual in per cent, %Res.

The k^3 -weighted Fourier back-transformed spectra of second RSF peaks ($\Delta R = 2.9-4.2 \text{ \AA}$ for the highest concentrated sample and $\Delta R = 2.9-3.7 \text{ \AA}$ for the two others) are shown in Figure 4. The structural results obtained by data analysis using Th and Si as backscatter atoms are shown in Table 2. Accordingly, the second peak consists of 1.5-1.7 Si at $\sim 3.85 \text{ \AA}$ and ~ 0.7 Th at 3.77 \AA (14 and 40 $\mu\text{mol/g}$). The σ^2 terms were set to 0.005 \AA^2 as in the thorite reference. The spectrum of the most concentrated Th sample (166 $\mu\text{mol/g}$) clearly differs from the spectra of the two less concentrated samples (14 and 40 $\mu\text{mol/g}$), indicating differences in the Th co-ordination environment. For example, there is a beat pattern near 6.5 \AA^{-1} in the most concentrated Th sample which indicates the presence of at least two cationic subshells containing heavy atoms such as Th.

At high Th concentration (166 $\mu\text{mol/g}$) neither a Th-Th and Th-Si, nor a Th-Th₁ and Th-Th₂ two-shell model provided a good fit to the experimental spectrum. Nevertheless, it is possible to propose an uptake mechanism for Th in this sample. In Figure 5 the EXAFS spectra of thorite [8] and amorphous Th(OH)₄ are compared to the 166 $\mu\text{mol/g}$ Th sample. The likeness of the sorption sample

Figure 4. k^3 -weighted EXAFS functions obtained by Fourier back-transforming second RSF peaks in Figure 3 ($\Delta R = 2.9$ - 4.2 \AA for $166 \mu\text{mol/g}$, $\Delta R = 2.9$ - 3.7 \AA for 14 and $40 \mu\text{mol/g}$)

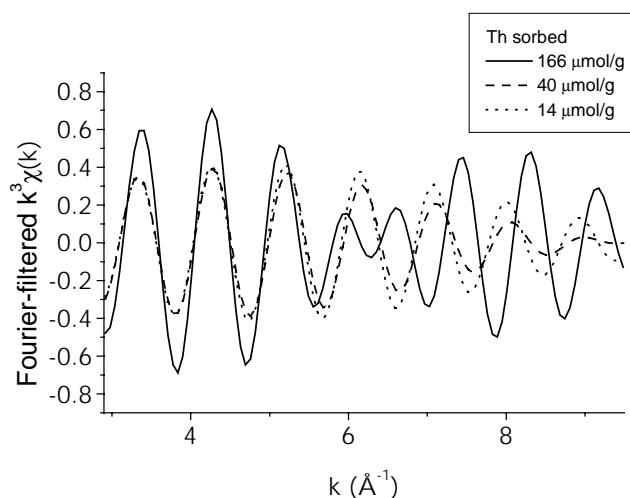
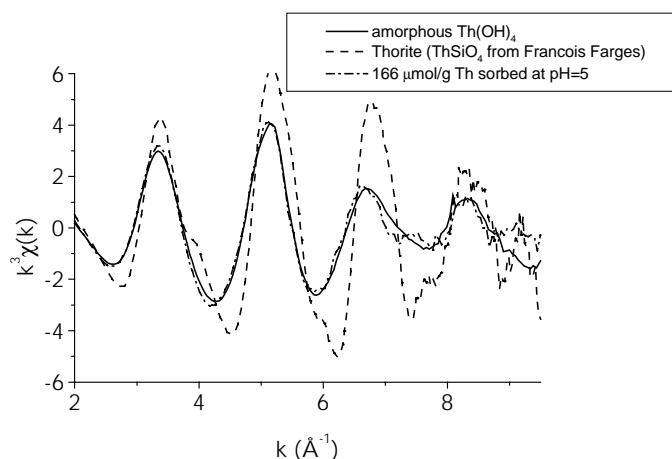


Table 2. EXAFS structural parameters for the nearest Th and Si shells and Th sorbed on montmorillonite (ph = 5)

Sample	Th-Si			Th-Th			ΔE_0^f [eV]	%Res
	N	R [Å]	σ^{2f} [Å ²]	N	R [Å]	σ^{2f} [Å ²]		
166 $\mu\text{mol/g}$	A reasonable fit could not be achieved							
40 $\mu\text{mol/g}$	1.5	3.84	0.005	0.7	3.76	0.005	6	29.7
14 $\mu\text{mol/g}$	1.7	3.85	0.005	0.7	3.77	0.005	6	25.0

f: Fixed during the fit procedure.

Figure 5. Comparison of k^3 -weighted XAFS functions of reference compounds and the highest concentrated Th sample



and the Th amorphous precipitate is striking, and suggests the formation of a similar precipitate at high Th concentration. Again it was not possible to fit $\text{Th}(\text{OH})_4$ data with just one or two Th-Th backscattering pairs. The reason lies probably in the fact that the second peak of the $\text{Th}(\text{OH})_4$ compound is too disordered to be fitted with a two-Th shell harmonic model [19].

Discussion

The results obtained in this study for the two most diluted samples compare well with those reported by Östhols, *et al.* [19] for the sorption of Th on amorphous silica: 1.7-2.7 O at 2.27-2.34 Å vs. 2.6-3.0 O at 2.27-2.28 Å (this study), 4.4-5.4 O at 2.53-2.56 Å vs. 6.9-7.1 O at 2.45-2.46 Å (this study) and 1.3-2.7 Si at 3.79-3.89 Å vs. 1.5-1.7 Si at 3.84-3.85 Å (this study). While the co-ordination numbers and interatomic distances for the first O and the Si shell match well, the second Th-O distance in the Th/montmorillonite system is significantly shorter. The distance of the second shell is characteristic for Th-H₂O bonds (2.44-2.45 Å) [20] and therefore does not modify the structural interpretation. EXAFS structural parameters for Th-sorbed silica were interpreted by Östhols, *et al.* [19] as the formation of a double corner-sharing Th surface complex. Based on the similarity of structural parameters in the two systems, it can be hypothesised that Th is bound to Si tetrahedra in a similar manner.

In conclusion, this study reveals the presence of two Th-O co-ordination spheres for the uptake of Th on montmorillonite at pH = 5. At low Th concentration (14 and 40 µmol/g), Th is bound to about two Si tetrahedra by a double-corner sharing mechanism as in Th sorbed silica. At high Th concentrations (166 µmol/g), Th precipitated as a Th(OH)₄-like amorphous thorium hydroxide.

Based on the data obtained in this study two structural mechanisms can be inferred for the samples with low Th concentration: The formation of a Th surface complex at the montmorillonite surface or the precipitation/neof ormation of a Th-silicate. The neof ormation of mixed (i.e. sorbate + sorbent metals) precipitates has recently been demonstrated in the case of Ni uptake on clay minerals [1,4,21] and Co on quartz [22].

Acknowledgements

The authors thank the staff of the Rossendorf Beamline at the ESRF for their support during the XAFS measurements, and the European Synchrotron Radiation Facility (ESRF) at Grenoble, France, for the provision of beam time. François Farges is thanked for providing the thorite spectrum. Partial financial support was provided by the National Co-operative for the Disposal of Radioactive Waste (Nagra), Wettingen (Switzerland).

REFERENCES

- [1] A.M. Scheidegger, G.M. Lamble and D.L. Sparks, *J. Colloid Interface Sci.*, 186, 118-128 (1997).
- [2] M. Schlegel, A. Manceau, D. Chateigner and L. Charlet, *J. Colloid Interface Sci.*, 215, 140-158 (1999).
- [3] M.L. Schlegel, A. Manceau and L. Charlet, *J. Colloid Interface Sci.*, 220, 392-405 (1999).

- [4] A.C. Scheinost and D.L. Sparks, *J. Colloid Interface Sci.*, 223, 1-12 (2000).
- [5] S.I. Tsipursky and V.A. Drits, *Clay Minerals*, 19 (2), 177-193 (1984).
- [6] P.H. Santschi and B.D. Honeymann, *Radiat. Phys. Chem.*, 34 (2), 213-240 (1989).
- [7] N. Savanonda, E. Prongpunyasakul and S. Ratanakorn, New York, Gordon and Breach (1985).
- [8] F. Farges, *Geochim. Cosmochim. Acta*, 55, 3303-3319 (1991).
- [9] G.R. Lumpkin, R.C. Ewing, B.C. Chakoumakos, R.B. Gregor, F.W. Lytle, E.M. Foltyn, F.W.J. Clinard, L.A. Boatner, M.M. Abraham, *Journal of Materials Research*, 1 (4), 564-576 (1986).
- [10] R.C. Ewing, B.C. Chakoumakos, G.R. Lumpkin and T. Murakami, *Nuclear Instruments and Methods in Physics Research*, 32 (1-4), 487-497 (1987).
- [11] B. Baeyens and M.H. Bradbury, *J. Contam. Hydrol.*, 27, 199-222 (1997).
- [12] J.L. Ryan and D. Rai, *Inorg. Chem.*, 26, 4140-4142 (1987).
- [13] E. Östhols, J. Bruno, I. Grenthe, *Geochim. Cosmochim. Acta*, 58 (2), 613-623 (1994).
- [14] V. Neck and J.I. Kim, *Radiochim. Acta*, in review (2000).
- [15] W. Matz, N. Schell, G. Bernhard, F. Prokert, T. Reich, J. Claussner, W. Oehme, R. Schlenk, S. Dienel, H. Funke, F. Eichhorn, M. Betzl, D. Prohl, U. Strauch, G. Huttig, H. Krug, W. Neumann, V. Brendler, P. Reichel, M. Denecke and H. Nitsche, *Journal of Synchrotron Radiation*, 6, 1076-1085 (1999).
- [16] T. Ressler, *Journal of Synchrotron Radiation*, 5 (2), 118-122 (1998).
- [17] J.J. Rehr, J. Mustre de Leon, S. Zabinsky and R.C. Albers, *Journal of the American Chemical Society*, 113 (14), 5135-5140 (1991).
- [18] M. Taylor and R.C. Ewing, *Acta Cryst.*, B 34, 1074-1079 (1978).
- [19] E. Östhols, A. Manceau, F. Farges and L. Charlet, *J. Colloid Interface Sci.*, 194, 10-21 (1997).
- [20] H. Moll, M.A. Denecke, J. Jalilehvand, M. Sandström and I. Grenthe, *Inorganic Chemistry*, 38 (8), 1795-1799 (1999).
- [21] R. Dähn, A. Scheidegger, A. Manceau, M. Schlegel, B. Baeyens, M.H. Bradbury, *Journal of Synchrotron Radiation*, in review (2000).
- [22] A. Manceau, M. Schlegel, K.L. Nagy and L. Charlet, *J. Colloid Interface Sci.*, 220, 181-197 (1999).

SORPTION OF URANYL SPECIES ON ZIRCON AND ZIRCONIA

C. Lomenech,¹ R. Drot,¹ J.-J. Ehrhardt,² J. Mielczarski³ and E. Simoni¹

¹Institut de Physique Nucléaire, Orsay, France

²Laboratoire de Chimie Physique pour l'Environnement, Villers-lès-Nancy, France

³Laboratoire Environnement et Minéralurgie, Vandœuvre-lès-Nancy, France

Abstract

The safety of a long-term storage of radioactive waste in deep geological repositories would be strongly affected by the migration properties of radionuclides through the different barriers to the surface of the earth. Since the main process involved in the retention of radioactive ions is their sorption at the water/mineral interface, a quantitative description of the sorption reactions is needed.

Macroscopic data have for a long time been the only source of information used to propose a modelling of sorption equilibria, although they bring no direct information on the nature of the sorbed species; a microscopic structural investigation of the surface complexes is difficult indeed, because of the small amount of matter sorbed. Thus, in this study, parallel to the macroscopic measurements, different complementary spectroscopic techniques have been used in order to determine the nature of the surface species. As the final purpose of such a study is the simulation of the experimental retention data, the precise structural identification of the sorption equilibria will then be very useful to constrain the data simulation code.

In this work, we present the results of both macroscopic and microscopic studies of the sorption of uranyl species on zircon and zirconia. The first part of our macroscopic approach was the surface characterisation of the non-sorbed materials by the determination of the specific areas, of the pH of the isoelectric points, and of the sorption site numbers, while the second part aimed at obtaining the sorption isotherms (percentage of sorption versus pH), which was performed using alpha spectrometry, for different uranyl concentrations, media (NaClO₄ or KNO₃) and ionic strengths.

The spectroscopic identification of the different surface complexes and sorption sites has been carried out using four different spectroscopies. Whereas time-resolved laser spectrofluorimetry gave a direct answer concerning the number of surface species (only for a few samples, because of the weak signals obtained), X-ray electron spectroscopy enabled us to show differences in the bonding energies between uranyl species sorbed either on zircon or on zirconia, or for the same sorbent for different pH or in different media (nitrate or perchlorate), this last point being confirmed by diffuse reflectance infrared spectroscopy. EXAFS measurements were then performed on well-characterised samples, on zircon and zirconia at different pH and in different media, for either dry or *in situ* samples. The results clearly show that the sorbed species are inner sphere complexes, and they seem to indicate strong similarities between our dry samples and the *in situ* experiments, which confirms the validity of other spectroscopic measurements. Moreover, differences between samples prepared at different pH were observed, which could possibly be explained by the formation of a surface precipitate.

